5-2021

A Novel Technique for Distributed Measuring of Strain in the Vadose Zone

Grant A. Plunkett
Clemson University, gaplunk@g.clemson.edu

A NOVEL TECHNIQUE FOR DISTRIBUTED MEASURING OF STRAIN IN THE VADOSE ZONE

A Thesis
Presented to
the Graduate School of
Clemson University

In Partial Fulfillment
of the Requirements for the Degree
Master of Science
Hydrogeology

---

by
Grant Plunkett
January 2021

Accepted by:
Dr. Lawrence Murdoch, Committee Chair
Dr. Liwei Hua
Dr. Scott DeWolf
Dr. Ronald Falta

ABSTRACT

Characterizing water content and pressure changes in the vadose zone is important to understanding a variety of geologic processes, ranging from storage and drainage, to evapotranspiration, and recharge. Changes in water content, or pressure, cause strain in the solid porous medium of the vadose zone, and it is possible that measuring those strains could be used as a characterization tool. The Coherence-length-gated Microwave Photonics Interferometry (CMPI) technique measures strain at high resolution along many intervals defined by pairs of reflectors distributed along an optical fiber. This technique has recently been developed at Clemson University, and it appears to have the spatial and temporal resolution to characterize strains that are expected to occur with hydrologic changes in the vadose zone. However, the technique has never been used to measure strain in porous media, so its capabilities remain uncertain. The objective of this thesis is to evaluate the ability of using CMPI to measure strain changes in the vadose zone.

The research approach consists of conducting laboratory tests using a column filled with sand that is subjected to changes in water content and pressure. An optical fiber with CMPI reflectors was laminated in a high-surface-area ribbon and deployed along the axis of the column. The column was made from 8-inch, Schedule 40 PVC pipe (75 cm tall, 20 cm inner diameter) and filled with medium-grained sand (K = 2.5x10^{-6} m/s, porosity = 0.28, Coefficient of Uniformity = 2, van Genuchten (n = 4.34, α = 0.00039 m^{-1}, θ_s = 0.28, and θ_r = 0.08), Young's Modulus = 18 –30MPa). Five pressure and four temperature sensors were inserted through the wall of the column. The optical

fiber strain measurements include five reflectors spaced 10 cm apart in a ribbon on the inside, and 5 addition reflectors on the outside along the axis of the column. Strain measurements are made between pairs of reflectors. The reflectors are created in 250-micron-diameter acrylate-coated single mode Corning SMF28e+ optical fiber using a femtosecond laser. The optical fiber was laminated between two pieces of polyester film creating a large surface area to transfer strain from the porous media to the optical fiber. The experiments were conducted by filling the column from the bottom or infiltrating water from the top. The water was allowed to equilibrate to room temperature prior to each test in order to limit thermoelastic strain.

Five injection tests with a rate of 250 ml/min and three infiltration tests at varying rates were conducted, and the results show patterns of strain and pressure are generally similar. Hydrologic conditions define three zones based on the pressure magnitude and distribution.

1.) *Ambient Zone* where the pressure heads are quasi-static, and the pressure gradient is roughly unity (head gradient of zero). This is the uppermost zone and is characterized by negative pressures. The pressure head gradient is approximately 1.

2.) *Transition Zone* where the pressures increase from ambient to zero, are changing relatively rapidly and the pressure gradient is relatively steep (pressure head gradients of 2). The Transition zone is 10 to 15 cm thick.

3.) *Positive Pressure Zone* where the pressure is positive, the rate of change is slower than in the transition zone and the gradient is flatter (pressure head gradient 1.1 to 1.2). This is the lowest zone in the column.

Injection of water causes the pressure to increase and the three pressure zones to move upward. The Transition zone moves at a rate of approximately $2x10^{-4}$ +/- $0.5x10^{-4}$ m/s, according to analyses of pressure profiles. This is the same as the ratio of the volumetric flux ($5.4x10^{-5}$ m/s) and the porosity (0.28).

Strain signals in the range of 10s of με were observed with a noise level of generally less than 0.1 με (signal to noise ratio of greater than 100) during injection and drainage. The strain generally increases during injection and decreases during drainage. The strain rate, and how the strain relates to changes in pore pressure varies considerably, however. These changes are repeatable and were used to define four stages in the strain time series during filling and four stages during draining. An additional three stages were identified in the time series of tests that involved filling the column until water ponded on the surface of the sand.

The spatial and temporal distributions of strain caused by injection depend on the location of the moving pressure zones. The locations of the different pressure zones were determined from pressure profiles at different times and these data were transferred to strain time series. This shows that the pressure zones occur in consistent locations relative to the strain sensor during the different stages, which indicates that the changing pore pressure is controlling the strain. This was expected, but how the pressure controls

the strain was unexpected. In some locations, the strain increases with increasing pressure, which is consistent with Hooke's Law. In other locations, however, the strain is unchanged or decreases when the pore pressure increases. It is inferred that this is a result of stress transfer, where an increase in stress in one location causes a decrease in stress in another location to maintain equilibrium.

An interesting effect occurs when the upper surface of the sand becomes saturated. Significant compression (several 10s of με) occurs as the pressure and saturation increase at the upper surface. Compression occurs throughout the column, but the effect is greatest at the top of the column. The rate of compression is fastest slightly before ponding occurs, but it slows markedly and nearly stops when water starts to accumulate at the surface (ponding). This effect reverses when the surface of the sand is drained, resulting in tension throughout the column. The compression caused by this effect can be as large or larger than the tensile strain that accumulated during filling. This effect was unexpected because increasing pressure is normally associated with tensile strain. Nevertheless, this effect was observed consistently in all tests where the pressure changes at the upper surface, including tests where water was injected from below or infiltrated from above. This effect behaves as if the pore pressure at the upper surface of the sand exerts a normal force on the boundary (increasing pore pressure exerts a downward compression on the boundary).

Results of the laboratory experiments indicate that CMPI can measure strain caused by fluid pressure changes in the vadose zone with a signal to noise ratio of 100 or more. Injection and drainage cause a strain signal that is complex, but repeatable. The

magnitudes of the strain signal are consistent with magnitudes that are expected based on poroelastic calculations using independently measured properties of the sand. The strain signal can be explained with a conceptual model that recognizes three basic effects: 1.) strain in proportion to pressure change (Hooke's Law); 2.) strain independent of local pressure change due to stress transfer; 3.) strain caused by a load applied at the ground surface that is proportional to the pressure change. These results indicate that the CMPI technique with an optical fiber laminated in a polyester ribbon generates data that represent the strain distribution during hydrologic processes of imbibition and drainage in variably saturated sand. This suggests that distributed strain measurements using CMPI could be a viable approach for evaluating processes in the vadose zone, laying the groundwork for future field implementation.

ACKNOWLEDGEMENTS

Many people have provided input crucial to this thesis. In particular, I would like to acknowledge and thank Drs. Lawrence Murdoch, Scott DeWolf, and Liwei Hua for their considerable contributions that made this work possible. Dr. Murdoch provided direction in the experimental design and writing. Dr. DeWolf assisted with electronic data collection for auxiliary components. Dr. Hua's technique and assistance in the measurement of strain have been instrumental for this research.

This work was funded by the Department of Energy, Project FE0028292.

CONTENTS

LIST OF TABLES

LIST OF FIGURES

CHAPTER ONE: INTRODUCTION

Understanding water content and movement in the vadose zone has applications from agriculture (Engman, 1991), to environmental monitoring (Baram et al., 2012), to resource management (Dobriyal et al., 2012). Soil moisture measurement techniques range in their scales. The largest scale remote sensing techniques use satellites to record electromagnetic radiation coming from the ground which can be interpreted to give soil moisture values for scales ranging from 10^3 to 10^4 m (Ochsner et al., 2013). Ground-based sensing has a greater resolution than remote sensing. Techniques such as capacitance probes and time domain reflectometry can measure soil moisture at the 10^{-1} m scale (Blonquist et al., 2005).

Changes in pressure or water content in the subsurface cause strain (Hisz et al., 2013). It is possible to use strain as a in situ measurement of water content in the vadose zone because a change in water content will alter the total stress. Point measurements of strain have been made using an instrument developed at Clemson University, called the DEL-x (Thrash, 2016), however a new method can measure the strain in regions distributed over a length of optical fiber (Hua et al., 2017). This distributed strain measurement method needs to be tested for use in the vadose zone. Laboratory tests will evaluate this technique and report findings on strain and how it varies during changes in pressure.

VADOSE ZONE MOISTURE MEASUREMENTS

The vadose zone by definition is the region between the water table and the ground surface (Martin & Koerner, 1984). This region is where many interesting dynamics occur between the groundwater and porous media. Fluctuations in the water table induce changes in the vadose zone. These fluctuations can come from raising and lowering the pressure in the saturated zone from below, or infiltration from above.

Methods have been developed for characterizing hydrogeologically relevant properties and processes in the vadose zone over scales ranging from kilometers to millimeters. These include characterizing the amount of cosmic ray absorption to infer water contents (Zreda et al., 2012), to neutron probes in boreholes (Dobriyal et al., 2012), to classical well testing characterizing aquifer properties.

Water content can vary over the cm scale in the vadose zone. Sensors can measure these fluctuations. However, in situ moisture sensors can be bulky and disturb the material they are situated in and have the potential to alter the material and measurements. Tensiometers are often used to measure suction pressure in unsaturated soils. This works as long as the tubing and porous cup of the tensiometer remains saturated. Time domain reflectometry (TDR) can measure water content in a subsurface sensor at a scale of around 10 cm (depending on the probe) (Blonquist et al., 2005). However, installing the instrument can disturb the sample and affect reported water content (Topp et al., 2001). Distributed measurements are possible with a cascaded TDR sensor (Aharoni et al., 2017)

STRAIN MEASUREMENTS

Measuring strain in the subsurface has applications that include geotechnical measurements of slope stability (Nitzsche & Herle, 2020), structural health of dams (Prakash et al., 2018), and modeling of subsidence (Hall & Fox, 2018). Strain measurements can monitor seismic events (Hagiwara, 1974), enhance the study of plate tectonics (Weiss et al., 2020), and monitor volcanism (Luttrell et al., 2013). Measuring the stress-strain relationship in reservoirs is important for the oil and gas industry (Gambolati et al., 1999). Soil compaction is a problem in agriculture negatively affecting crop growth (Keller et al., 2012).

InSAR

Satellites using Interferometric Synthetic Aperture Radar (InSAR) can measure strain rates and plate velocities (Weiss et al., 2020). These can be used to monitor tectonically active regions to better understand orogeny and crustal deformation. Naturally, this has potential use in hazard mapping for earthquakes and related disasters (e.g. Fattahi & Amelung, 2016). InSAR has also been used in measuring subsidence (Hongdong et al., 2011).

Tiltmeters

Tiltmeters have been used in diverse applications such as monitoring volcanos and monitoring hydraulic fracturing (Warpinski et al., 1997). Rainfall and changes in barometric pressure can induce measurable deformations in the subsurface, with up to 0.5

με measured in solid rock at a depth of 60 m during a rainfall event. (Dal Moro & Zadro, 1998).

DEL-x

An instrument has been recently developed at Clemson to measure small scale deformation in the subsurface. This instrument, the DELTA-extensometer, known as the DEL-x can measure vertical changes in the subsurface down to a resolution of 0.01 μm (Murdoch et al., 2016: Freeman, 2012; Thrash, 2016).

One finding that emerged from the DEL-X is that strain is affected by changes in water content, weight in overlying soil, changes in pore pressure (water or air), changes in surface load by barometric pressure, and temperature. However, signals need to be separated. Signals migrate with time, so one way to help separate signals and improve interpretation is to measure strain at multiple locations with depth. This is possible with DEL-X but limited by scale and logistics to 1-2 m spacing. Higher resolution is needed to resolve wetting and barometric fronts (Thrash, 2016).

Optical Fiber Strain sensors

Optical fibers have been used as strain sensors for some time to measure strain. Mainly in civil engineering applications such as structural health monitoring (Inaudi & Glisic, 2006), but increasingly including geomechanical relevance.

Distributed Brillouin Sensing systems

Distributed Brillouin Sensing systems (DBSs) have been used in subsurface strain measurements. Madjdabadi et al., 2016 explores using DBSs in mining applications measuring strain in a rock mass. The strains measured are in the 1000s of με with a noise level of approximately 80 με.

Fiber Bragg Grating

Recently, Fiber Brag Grating (FBG), an optical fiber sensor, has been explored for real time measurement of strain in unsaturated aeolian sands (You et al., 2019). Temperature and strain results show that the strain is greatly affected by temperature, however, most of the temperature change occurs near the surface of the sand.

Challenges to Measuring Strain in the Vadose Zone

A technique for measuring meaningful strain needs to be able to clearly resolve strain magnitudes expected in the vadose zone without affecting the material in a way that overly complicates the reading. Many vadose zones are soft, unconsolidated porous media. Sensors need to couple to the subsurface formation using a material with compliance high enough to not affect the measurement. The DEL-X measured displacements of a couple microns during rainfall events (Thrash, 2016). An instrument would need to have a sub-micron resolution to resolve these fronts. Problems and additional challenges arise when electrical components are placed in the ground, an ideal instrument would have its electrical components on the surface.

Coherence-length-gated Microwave Photonics Interferometry

Coherence-length-gated Microwave Photonics Interferometry (CMPI) is a technology that measures strain between reflectors etched into optical fiber (Hua et al., 2017). These measurements are distributed and can be spaced at a desired location. Earlier experiments of CMPI being used to measure strain have yielded encouraging results, however, there is currently no application involving loading or flow in porous media.

Description of technique

CMPI technology works by using a laser and an electro-optic modulator (EOM) to create light modulated in the microwave band. The light is injected into an optical fiber, and back scattered light from reflectors in the fiber is detected by a photodetector. The amplitude and phase of the reflected light at the modulated frequency is resolved through synchronized detection. After scanning the designated modulation band, the complex reflection spectrum is obtained. The time domain signal is obtained by Fourier transform of the complex reflection spectrum. Reflected waves that separate within the coherence length of the laser produce optical interference, which is sensitive to the localized strain (Hua et al., 2017) . The chirp effect of the EOM is used to create two quadrature signals for the interference phase demodulation in the CMPI system, which allows the strain to be measured between the reflector locations without complicated coherent detection schemes (Hua et al., 2020). An external interferometer (EI) can be added into the system to enable fully distributed sensing capability. CMPI has several unique advantages including high strain sensitivity, high signal quality, relieved

requirement on fabrication, low dependence on the types of optical waveguides, insensitivity to variations of polarization, and high spatial resolution.

CMPI Applications in Hydrogeology

Microwave photonics used with optical fiber has a diverse set of applications including structural monitoring (Leung et al., 2015). Potential applications in the subsurface include monitoring CO_2 injections for leaks, determining aquifer characteristics from pumping tests, and monitoring infiltration in the vadose zone. Advancing strain measurement capabilities from point measurements to distributed measurements over a length is important to understanding the movement of pressure fronts. For field applications to advance, CMPI strain sensing capabilities in porous media need to be evaluated first in the laboratory.

OBJECTIVE

This thesis has two distinct, but related objectives. One is to evaluate the feasibility of measuring strain caused by hydrologic processes in unconsolidated, variably saturated porous media. Another objective to evaluate the performance of the new sensing method Coherence-length-gated Microwave Photonics Interferometry as a technique for measuring strain in variably saturated porous media.

HYPOTHESIS

Strain in hydrogeologically relevant settings can be measured using optical fiber interrogated using the CMPI method.

APPROACH

The general approach to achieving the objective of the research is to use laboratory experiments to mimic hydrologic processes under ideal conditions and then measure the resulting distributions of pressure, temperature, and strain. The experiments will be configured by stretching a distributed optical fiber sensor through a sand-filled column and vary water pressure and saturation under controlled conditions in the laboratory to broadly resemble imbibition and draining processes in the vadose zone. The optical fiber is packaged in compliant strip that extends along the axis of the column.

The column contains features to allow instruments inside and outside as well as filling and draining from the bottom and infiltration from the top. It contains ports on the side where temperature and pressure sensors are inserted, and a port in the bottom where water can be injected and removed. Supports on the top of the column allow for a sprinkler head to infiltrate water from above.

This configuration allows water to be injected and either pumped out or drained by gravity out the bottom. It also allows water to be infiltrated in the top. The sand is filled to within a few cm of the top of the column, so water can pond on the sand.

Laboratory experiments conducted in the Advanced Materials Research Laboratory were used to evaluate the distributed strain under room temperature. A pair of optical fibers were used to measure the distributed strain using the CMPI method. An optical fiber with reflectors was packaged in a compliant strip with high surface area designed to couple the fiber to strain in the sand inside the column. The high compliance

allows for the strip and optical fiber to stretch as the material in the column deforms. High surface area helps to couple the strip to the porous media using friction. Another set of optical fiber reflectors are taped to the outside of the column. This is used to measure strain changes that may occur in the column itself.

The column was loaded with static weight to test the system and the resulting strain was used to estimate the elastic properties of the sand. Water was then injected in the bottom of the column to increase the water content and pressure in the column. Pressure and temperature were monitored with sensors along the column, and the distributed strain was measured with the optical fiber. These data were also measured upon drainage of the column. These are called "Fill and Drain" tests. Most Fill and Drain tests involve completely filling the column until water ponded on top of the sand. One test involved partially filling the column with water and then draining it.

Another set of tests were conducted by adding water to the top of the column to simulate infiltration. These tests involved sprinkling water over the top of the column using a shower head. Infiltration was tested at different rates. One test occurred where the drain at the bottom of the column was closed, allowing the column to fill up completely. Another set of tests created a continuous drainage scenario by opening the bottom drain throughout the test.

Experiments were conducted as a team effort. The work of this thesis focuses on designing and deploying experimental apparatus, controlling hydrologic processes (e.g. pumping or infiltration), making supporting hydrologic measurements characterizing hydrogeologic properties of soils, and interpreting data. A collaborator, Liwei Hua, was

responsible for obtaining data using microwave photonics and processing the data to determine strain.

ORGANIZATION OF THE THESIS

The following thesis is organized into seven chapters, including this introductory chapter. Chapter Two describes the setup for the experiments. Chapter Three describes physical characteristics and properties of the porous media used in the experiments. Chapter Four describes a loading experiment used to test the strain ribbon. Chapter Five describes tests involving varying the saturation in the column. Chapter Six introduces a conceptual model to help explain what the data from the experiments reveal. The thesis concludes with Chapter Seven.

CHAPTER TWO: APPARATUS AND EXPERIMENTAL METHODS

Experiments were conducted to test the equipment and reproduce hydrogeologically relevant situations during loading/unloading, injection/drainage, and infiltration/drainage. Loading/unloading tests were conducted by applying and removing different weights on the top of the column. The strain caused by these loads was measured to evaluate repeatability and to estimate material parameters. Injection/drainage tests were conducted by filling the column with water injected from the base, whereas infiltration/drainage tests were conducted by applying water to the top of the column. Water added during these tests was drained by either pumping or gravity. These tests were intended to simulate imbibition and infiltration.

Data Processing

The raw data was processed using a combination of programs, mainly MATLAB and Microsoft Excel. The data acquisition from the CMPI and LabJack data acquisition system used for the pressure and temperature sensors needed to be synchronized. The CMPI measured data at frequencies of 2 to 10 Hz depending on the experiment. The LabJack measured at 2 to 4 Hz. Timetables were made in MATLAB to synchronize the time to the start of the experiment and interpolate data points for the relevant data at intervals of every 0.25 seconds. These new data points are the linear interpolations of the raw data found between these points and accurately represent the data that would have been acquired at these time intervals.

APPARATUS

The experimental apparatus consists of a column filled with sand and fitted with sensors for pressure, temperature, and strain, and it also includes equipment for pumping and weighing water. The column used for the experiments is a 75 cm-long, 20 cm-diameter (8-inch nominal) PVC pipe (Figure 1). The column was sealed into a small basin using epoxy to provide structural stability and a watertight seal.

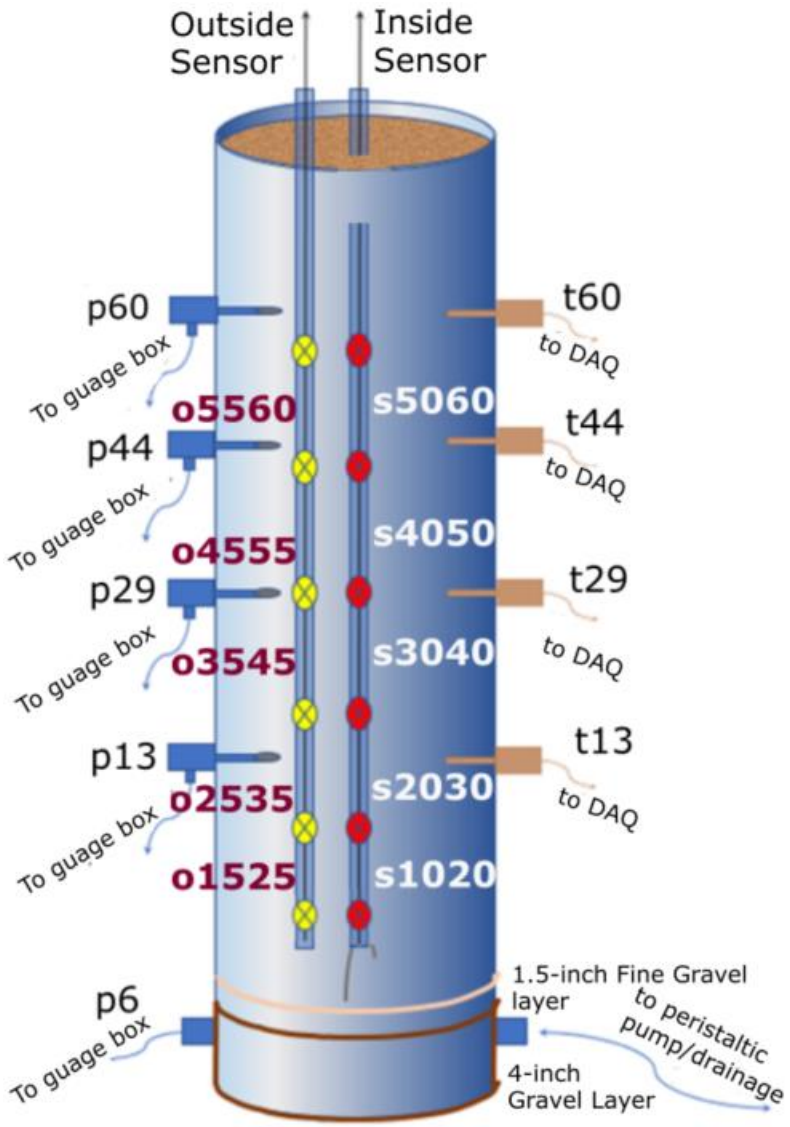

Figure 1: Column apparatus used for experiments, p6-p60 are pressure sensors. t13-t60 are temperature sensors. The five red points indicate the reflectors on a strain ribbon in sand inside of the column; yellow points indicate reflectors attached to the outside of the column.

Column Configuration

The holes are drilled and tapped ¼ NPT in the side of the column to accommodate tubing and sensors. Two holes are on opposite sides of the column and approximately 2 cm from the bottom. One is used to attach tubing from a pump and is used for filling and

draining water. The other is used for pressure measurement and a sighting manometer. A needle valve at the base of the sighting manometer can be used to isolate the manometer, which is necessary to prevent air from entering the column through the manometer during drainage. Two rows of holes extend along the axis on opposite sides of the column. The holes are 13, 29, 44, and 60 cm from the base. These holes were used for pressure and temperature sensors, and the name of the sensor includes the height of the access hole above the base.

A MasterFlow peristaltic pump equipped with 0.25-inch diameter tubing was used to inject, drain, and infiltrate the column. The peristaltic pump provided a nearly constant flow rate of 100 ml/min. The pump was attached to a tank that is weighed. Weighing the tank using the load cell array and assuming a constant density provided data on the water volume during injection or drainage.

To stabilize apparatus components and to lessen temperature fluctuations caused by air current convection, a frame was constructed around the column. This frame is made of T-Slotted aluminum bars. Panels made from polystyrene foam and transparent polycarbonate plastic are on the side of the frame to reduce air movement, and resulting temperature changes, at the column.

Infiltration is conducted using a 15 cm diameter shower head that is placed on a piece of polycarbonate supported by the frame 8 cm over the top of the column. The system evenly distributes water over the surface of the column except for the area below the fiber optic strain ribbon. This area is blocked out of the shower head to lessen the number of drops of water disturbing the optical fiber.

The column was filled to a depth of 5 cm with gravel. The gravel has a higher hydraulic conductivity than the sand. Water is injected into the side of the gravel layer and the high hydraulic conductivity causes the head to be essentially uniform over the gravel layer. This causes the upward flow rate to be essentially uniform over the column. On top of the gravel layer is a fine mesh overlain by, a centimeter-deep layer of coarse-grained, well sorted sand. The rest of the column is filled with fine to medium-grained sand. Soil Properties of these materials are presented in Chapter Three.

The column was leveled by placing spacers under the base and measuring with a bubble level.

Pressure, Temperature, Water Volume Measurement

Strain, pore pressure, temperature, and volume of water injected/drained were measured and recorded during the experiments. These quantities were measured with sensors and the data were recorded using a data acquisition system.

Pressure Sensors

Pore pressure is measured in the column using Honeywell (model ABPDANT005PGAA5) pressure transducers. These are board-mount transducers with a 0-35 kPa (0-5 psi) span, an accuracy of 0.25% of the span and a total error band of 1.5% of the span. They are designed to work with wet media, are temperature compensated and have an amplified analog output. These transducers are inexpensive and well suited to measuring pore pressure in the range of the experiments. They can accommodate an overpressure of ~1 MPa (150 psi), which makes them robust in an experimental setting.

Even though the Honeywell transducers were well suited to measuring pressures over the expected range during the experiments, they only measure positive pressure, and the pressure in the column was expected to range from +/- 6 kPa. The transducers were mounted on a horizontal frame below the column to accommodate this discrepancy, which ensured that the pressure signal would remain within their measurement range

The transducers are attached to plastic tubing that extends to a porous ceramic cup, which contacts the soil in the column. The porous ceramic cup is 0.635 cm (0.25 inch) in diameter by 2.858 cm long, 1 bar standard flow (Soilmoisture 0652X03-B01M1). The cup is sealed onto an aluminum (the aluminum corroded during use, so in retrospect these tubes should have been made from brass or stainless steel) tube, which is connected to a four-way brass fitting (Clippard 15002-3-BLK). The assembly functions like a miniature tensiometer, with the high air-entry pressure of the porous ceramic cup ensuring the tubing remains filled with water when the pressure drops below zero. The fitting is sealed with 10-32 bolts on the top and back, and a barb fitting on the bottom is attached vinyl tubing (3 mm (1/8 inch) outer, by 1.5 mm (1/16 inch) inner diameter) that extends to a transducer (Figure 2). The aluminum tube is inserted into a compression fitting that allows it to be sealed in the side of the column.

The system must be filled with water from the transducer to the porous cup in order to make an accurate measurement. To accomplish this, the transducers are filled with water using a syringe attached to a small capillary tube, then the 3 mm tubing is filled with water an attached to the transducer. The bolt on the end of the aluminum tube is removed and the capillary tube is inserted the full length of the porous cup and water is

injected to displace air. The bolt on the end is attached and then the bolt on the top of the four-way fitting is removed. The capillary tubing is inserted down into the 3 mm tubing and water is injected to displace remaining air. The bolt is then replaced, and the system is ready to use.

The lowest gauge (p6) is connected adjacent to the gravel layer in the column opposite of the injection site. The other four sensors are connected to tensiometers like the one shown in Figure 2.

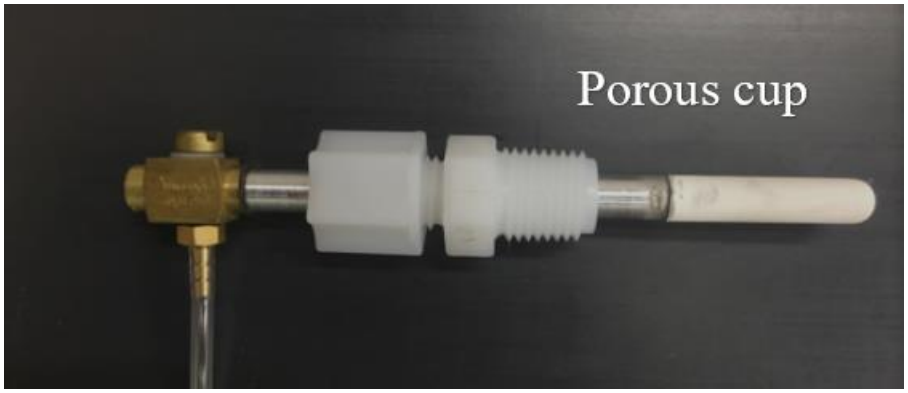

Figure 2: Tensiometer used to measure pressure in the sand on P2-P5. The porous ceramic cup shown on the end of the tensiometer allows suction to be measured.

The voltages recorded from the Data Acquisition system or DAQ are converted into pressures in Pascals by the using the relationship

$$Pressure(Pa) = \frac{voltage - 0.5}{4} * 34474 \qquad (1$$

Initial calibration of the sensors found that eq. (1) was accurate to within 10 Pa, which is sufficient for application in the experiments.

The pressure transducers were located at a common datum elevation below the bottom of the column, and as a result, the data from the transducers was proportional to the total hydraulic head. The pressure determined from eq. (1) was converted to total head by dividing by the unit weight of water. The pressure head at each tensiometer was determined by subtracting the height of the tensiometer above the datum from the total head. This resulted in measurements of both pressure and total heads as functions of time at each tensiometer.

Temperature Sensors

The column contains four temperature sensors. These sensors are made by embedding thermistors (EPCOS B57861S0303F040) into brass tubes filled with epoxy. An epoxy with a high metal content forms the contact between the sand and the thermistor. This is done to give the area around the thermistor a high thermal mass and thermal conductivity.

The electrical resistance in a thermistor changes with temperature, which needs to be converted to a voltage to be measured by the data acquisition system (LabJack U6-Pro). This is done by including the thermistor as one resistor in a basic voltage divider circuit where the output voltage varies as a function of the input voltage V_{in} as

$$V_{out} = \frac{R_0}{R_0 + R(T)} V_{in} \qquad (2$$

where $R(T)$ is the thermistor resistance and R_0 is a fixed "reference" resistance. These EPCOS thermistors are designed to have a reference value of 30 kOhms and a decreasing

resistance with increasing temperature. In this configuration, for example, when $R(T) = R_0$ the output voltage is one-half the input and increases with decreasing resistance.

The Steinhart–Hart equation combined with the voltage divider equation gives a way to convert from the voltages measured by the DAQ to the temperature. The electrical resistance as a function of temperature for these thermistors can be modeled as

$$\frac{1}{T} = \left(\frac{1}{B}\right) \ln\left(\frac{R}{R_0}\right) \qquad (3$$

where T is the temperature, R is the measured resistance, R_0 is the reference resistance (30 kOhms) and B is the thermistor specific calibration factor. For the thermistors used in the experiments, ($B = 3964^{o}$ Kelvin).

The thermistors are calibrated by filling the column up with water and placing a calibrated temperature and pressure transducer (HOBO U20) into the water. The thermistors temperature was calibrated to the temperature recorded by the HOBO U20 (Figure 3).

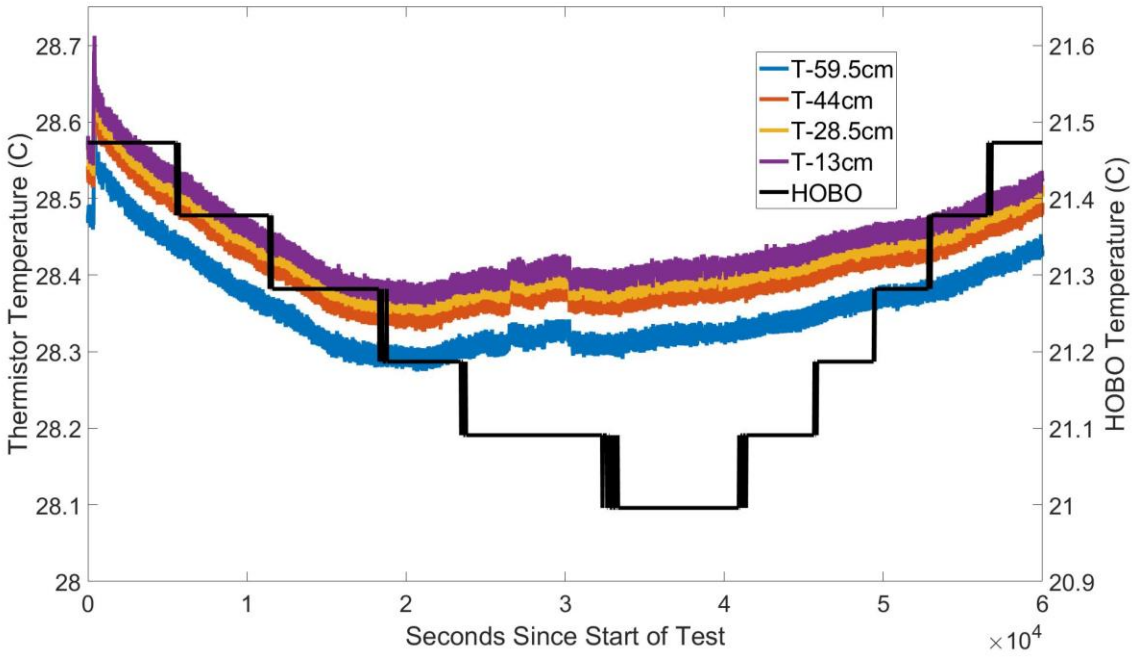

Figure 3: Temperature time series for the temperature measured with thermistors and the HOBO U20. The data respond together and have similar amounts of changes in temperature. The difference between the temperature found using the thermistors and HOBO gives constants subtracted from the Steinhart–Hart equation.

The temperature measured by the thermistors are slightly different, but they follow the same trend of decreasing by 0.3 ^{o}C over 2 x 10^4 s and then increasing slowly. The temperature measured by the HOBO follows those measured by the thermistors over the first 2x10^4 s, but there is a consistent difference of 7.1 ^{o}C between the data. This is accounted for by subtraction from the thermistor data. Then the temperature measured by the HOBO continued to decrease while the temperature measured by the transducers started to increase slightly. The temperature measured by the HOBO started to increase at t =3.5 x 10^4 s, and it is similar to temperatures measured by the thermistors at the end of the test. The step-like pattern of the time series indicates that the temperature change during the test is small compared to the analog to digital resolution of the HOBO U20.

The calibration test showed that the temperatures measured by the thermistors differ by approximately 0.1 ^{o}C, even though the temperature in the column was assumed to be uniform. This difference was accounted for by including an offset for each temperature measurement.

A temperature change can manifest as thermoelastic strain signal. To estimate the thermal expansion coefficients, a test recorded both the temperature and strain in the column filled with partially saturated sand over the course of a day (Figure 4). The temperature and strain fluctuate periodically during the test, with a period that ranges from 6 to 9 hrs. The total variation in strain is approximately 15 $\mu\varepsilon$, and the variation in temperature is 0.1 to 0.3 ^{o}C. This indicates a coefficient of thermal expansion of approximately 50 to 100 $\mu\varepsilon/^{o}$C. Thermal expansion coefficients were determined by correlating the temperature and strain at each position along the column. This tacitly assumes the temperature is uniform at each elevation.

The thermal expansion coefficients at each elevation (Table 1) were used with temperature measurements to estimate the strain due to thermoelastic effects. These strains were subtracted from the measured strains during the tests to correct for effects due to temperature change.

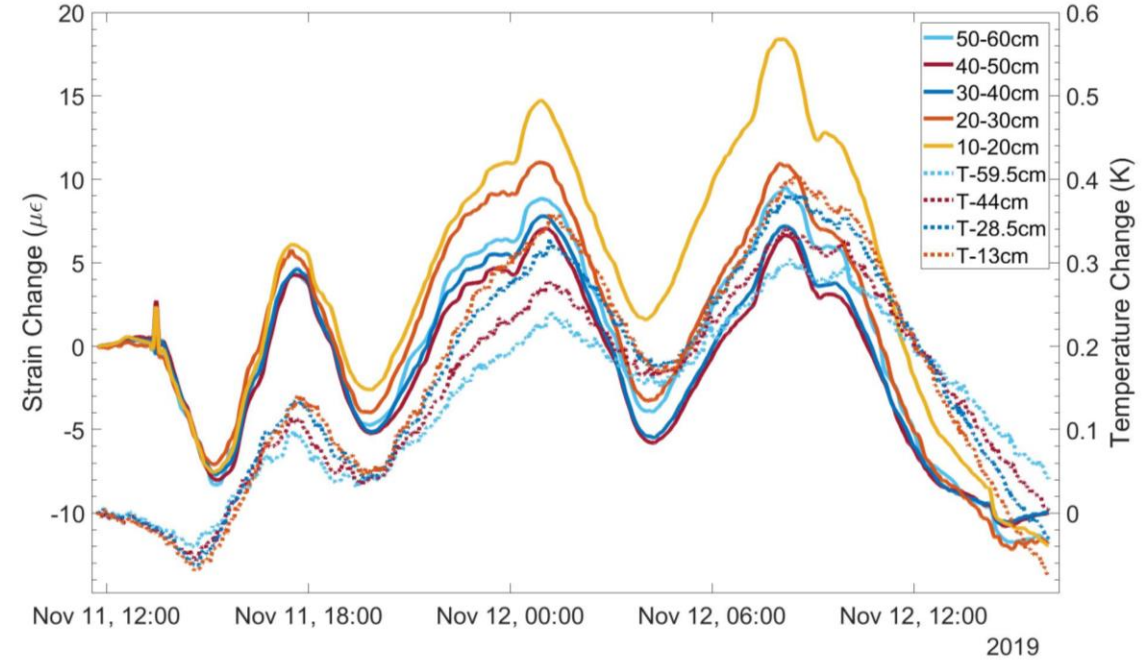

Figure 4: Strain change and temperature change time series during ambient conditions over one day. The peaks and dips in temperature and strain were used to find the coefficients of thermal expansion reported in Table 1.

Reflector Pair	**Temperature Compensation**
10-20cm	13με /C
20-30cm	100με /C
30-40cm	90με /C
40-50cm	65με /C
50-60cm	100με /C

Table 1: Coefficient of Thermal Expansion of the strain sensing regions determined during ambient conditions.

The temperature measured at the upper most temperature sensor (t60) is routinely higher compared to the other data during most of the experiments. The temperature at the

sensor second from the top (t44) is used to characterize the temperature at the upper strain sensor (s5060).

Characterizing water flow using load cells

The water used during an experiment was measured as a function of time by logging the weight of a tank used to store water for the test. Three load cells with a capacity of 15 N each (Honeywell FSG15N1A) were placed between two square polycarbonate plates (30 x 30 x 1 cm thick). (Honeywell, n.d.). A 19 L tank was placed on the polycarbonate plate, and the apparatus was calibrated by adding known volumes of water to the tank and recording the voltage change. The sum of the voltages from the three load cells are used to convert to volume of water using

$$V(g) = ((8042.4 \ +/-10\ ) * voltage) + 30.78 \quad (4$$

+/-10 g

The total weight on the scale is the sum of the individual weights recorded by each load cell.

For injection and pumping out, a 5-gallon bucket holds the water. During gravity drainage, a lower bin had to be used so the outlet hose could be placed at a lower height. In the raw data mass data, these changes are noticeable in the raw time series data.

The load cell data can be used as one method to approximate the water level in the column. This is done by taking the volume of water injected to reach the final height of the water level during the tests, around 73 cm, and dividing by the total volume of the column over this interval. This ratio is the average fillable porosity. It is less than the

true porosity due to water already being present in unsaturated portions of the column.

Data Acquisition System

Data from the pressure, temperature, and load sensors were recorded using a LabJack U6-Pro data acquisition system with 2 CB-37 expansion boards. This 5-volt data acquisition system works by recording voltages from voltage output sensors. The system has 16 channels and records data with 32-bit precision. It was configured using the manufacturer software LJLogUD. This program was used to measure the 16 channels at a rate of 2 or 4 Hz depending on the experiment.

Strain Measurement

Fiber Packaging

The coupling between porous media and optical fiber is poor because there is a small frictional force associated with the small surface area of the fiber. The fiber needs to be packaged in a way to allow the strain to be transferred and also to provide protection from breaking. Preliminary work shows that laminating fiber between polyester film can create a large surface area that generates frictional forces that couple the fiber to the sand. The polyester film also strengthens the fiber and reduces risk of breakage.

The fiber is packaged using 3M 396 tape. This tape sticks particularly well to itself and to the fiber. Daniel Hestenes, a collaborator, created a device to attach the fiber to the tape. The tape goes through a series of rollers that laminate the fiber between two pieces of tape (Figure 5).

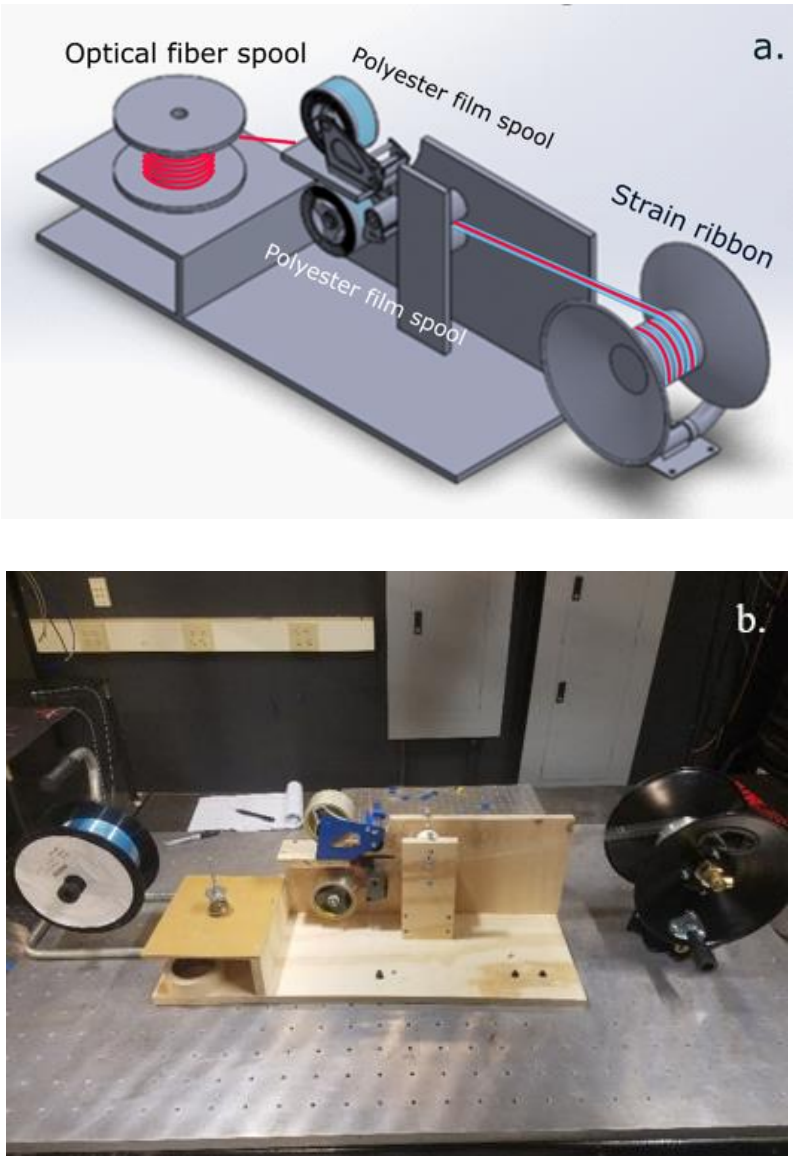

Figure 5: a. Computer generated model of laminating for assembling the optical fiber ribbon. b. Photograph of the actual device.

The laminating device laminates optical fiber between two pieces of tape to create a strain ribbon. Two spools are attached to a mounting bracket, which is slotted to accommodate several sizes of tape. The mounting bracket has a centered hole through its

length which places the fiber near the center of the tape. The fiber is then further aligned to the center of the tape with a small eyelet. The tape with the fiber passes through two plastic rollers. The plastic rollers are mounted in a vertically slotted hole and are manually tensioned using a pair of bolts. The packaged fiber is collected on a reel, which is used to pull the tape through the device.

This device aligns the two pieces of tape. It also minimizes the bubbles formed from incomplete contact between the two pieces of tape while keeping adequate tension on both the fiber and tape.

The strain ribbon used in these experiments was made from 2-inch-wide 3M 396 tape, which was subsequently trimmed to 1-inch wide. The fiber used on the inside of the inside of the column is not properly attenuated at the bottom. Some of the light leaks through causing an incomplete reflection. This was partially mitigated by blotting the bottom end of the fiber with black ink. Resultant from this, there are some instances where the signal from the bottom pair of reflectors ‘jumps’ or anomalously responds. This was fixed in subsequent designs by using an open knot at the bottom of the fiber.

A device was constructed a device to measure the coefficient of friction between the strain ribbon and sand. A normal force is placed on the ribbon, which itself rests on a brick with sand bonded to its surface. The axial force on the ribbon is incrementally increased with a dead weight, and displacement is monitored with a dial indicator. The axial force required to initiate displacement is recorded and then the test is repeated. The normal force is then increased, and additional tests are conducted.

Results show that the shear force increases with the axial force (Figure 6). The coefficient of friction is the ratio of the shear force required to initiate displacement under a certain normal force. The coefficient of friction between the tape and sand 0.37 +/- 0.05.

This finding is consistent with a test conducted by MCG Geotechnical Engineering Inc. and the Bureau of Reclamation in Colorado on the coefficient of friction between polyethylene sleeves that line pipes and various porous media. Their value of coefficient of friction between polyethylene sleeves and sand is between 0.22 and 0.49 (Gemperline & Rinehart, 2018).

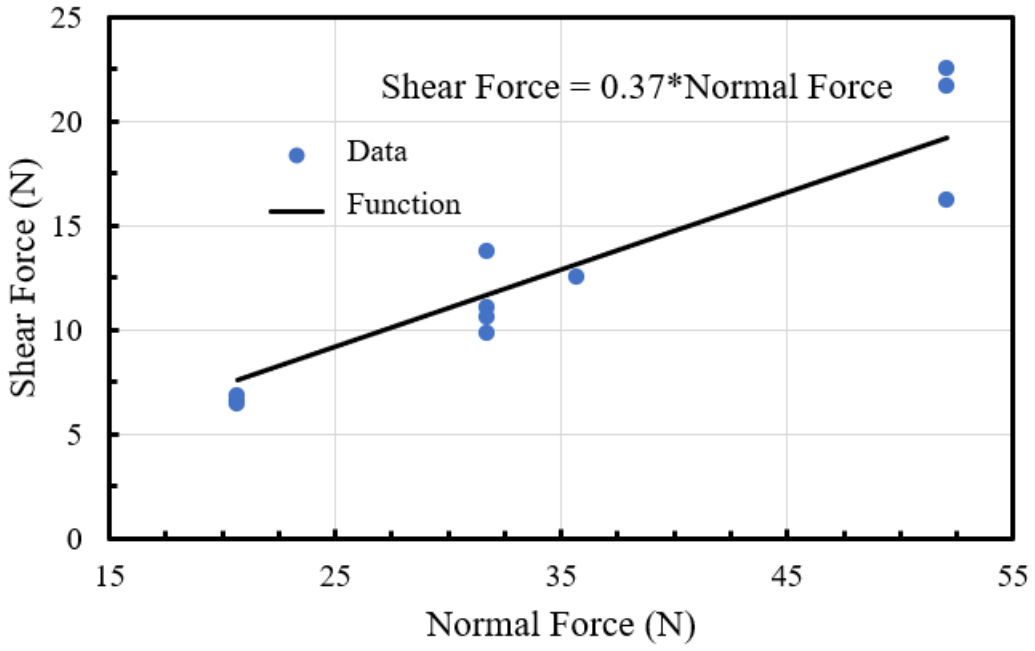

Figure 6: Shear force plotted with the normal force for friction tests. The coefficient of friction is the ratio of the shear force and normal force.

The compliance of the fiber packaging was measured using a loading machine. The machine pulls the material at a very precise load and strain is recorded by a Fiber Bragg grating sensor. The compliance is the ratio between the strain and the load.

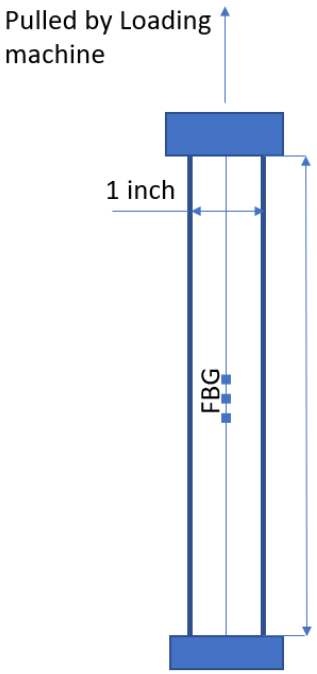

Figure 7: Simple model showing the device for measuring compliance.

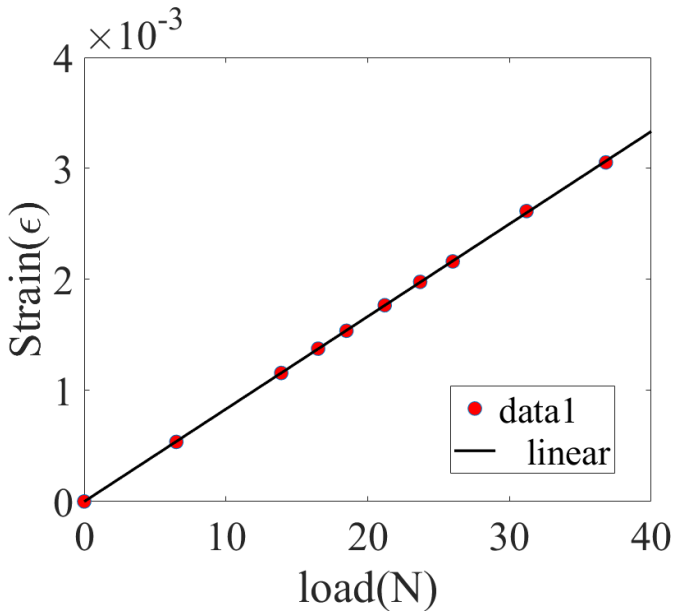

Figure 8: Strain measured using the FBG and the load on the machine stretching the optical fiber packaging.

The data are near linear under these loads and the compliance is calculated to be approximately 80 με/N.

Fiber Sensor Geometry and Installation

The strain ribbon contains two sets of reflectors. One set of reflectors was embedded in sand along the center axis of the column and another was attached to the outer wall of the column. The strain ribbon was attached to the bottom of the column by a hook that is embedded in the epoxy base. The fiber was under tension with a force of 10 N while the column was filled with sand. The reflector spacing is 0.1 m. Heat-shrink tubing was used to reinforce the fiber where the fiber comes out of the sand. The other set of reflectors were taped along the outside of the column to measure changes in strain on the column itself. These outer reflectors also have a spacing of 0.1 m.

CHAPTER THREE: SOIL PARAMETERS

Hydromechanical parameters of the sand are needed to describe the flow and deformation during the experiments. These parameters were measured using laboratory methods.

SATURATED HYDRAULIC CONDUCTIVITY

The saturated hydraulic conductivity of soil was measured using a falling head test. For this test, the PVC column used in preliminary investigations was used. It was fully saturated from below and standing water formed with a depth of 10.8 cm. The head was recorded, and an outflow tube was place above the water level. The end of the outflow tube was lowered to 1.2 cm above the surface of the sand, and the water was drained into a pan on load cells. The sand remained fully saturated during the test, and the weight of the accumulating water was recorded using the load cells.

This testing method measures saturated hydraulic conductivity in a setting similar to the experiments.

The hydraulic conductivity was determined by assuming mass conservation at constant density, which leads to:

$$Q_{in} = Q_{out} + \frac{dV}{dt} \quad (5$$

$$Q_{in} = 0 \quad (6$$

$$V = Ah \quad (7$$

$$\frac{dV}{dt} = A\frac{dh}{dt} \quad (8$$

According to Darcy's Law

$$q_{out} = -K\frac{dh}{dx} = K\frac{h}{L} \quad (9$$

Converting to Q

$$Q_{out} = \frac{KA}{L}h \quad (10$$

Substituting into (8)

$$0 = \frac{KA}{L}h + A\frac{dh}{dt} \quad (11$$

$$\frac{dh}{dt} = -\frac{K}{L}h \quad (12$$

Separation of variables

$$-\frac{K}{L}dt = \frac{dh}{h}$$

Integrating both sides

$$-\frac{K}{L}\int dt = \int \frac{dh}{h} \quad (13$$

Gives

$$t = -\frac{L}{K}\ln\left(-\frac{K}{L}h\right) \quad (14$$

The initial condition is

$$h = h_0 \; at \; t = 0 \tag{15}$$

Gives

$$C_1 = \ln\left(-\frac{K}{L}h_0\right) \tag{16}$$

Substituting for C_1

$$t + \ln\left(-\frac{K}{L}h_0\right) = -\frac{L}{K}\ln\left(-\frac{K}{L}h\right) \tag{17}$$

Rearranging

$$h = h_0 e^{-t\frac{K}{L}} \tag{18}$$

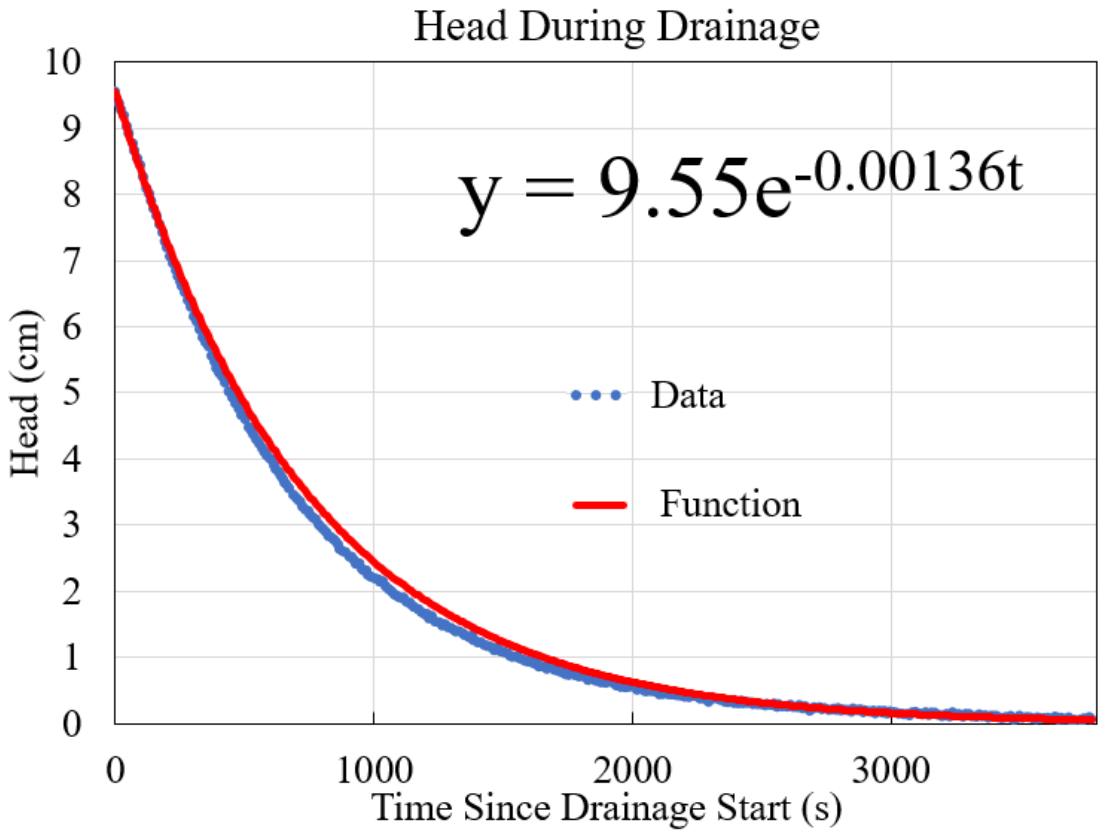

Figure 9: Head in outflow column time series with exponential decay equation displayed.

Using Equation 18 and the best fit line in Figure 9 the hydraulic conductivity of the sand is approximately $K = 0.025$ cm/s. The volume of water used to fill the column during the test gives the porosity. The packed sand in this smaller column has a porosity of approximately 0.28.

GRAIN SIZE DISTRIBUTION

Sieve tests were conducted to measure the grain size distribution. A mass of porous media was poured into a series of sieves on a shaker designed to vibrate the material allowing for maximum separation. The grain size distributions for the different materials present in the column are shown below.

Sand

The sand forms the region in the column where strain is measured. 4562 grams was sorted using 63, 125, 250, 300, 500, 710, 1000, and 1180 micron sieves. The distribution of sand grain sizes is shown in Figure 10. The grain size data indicate that this is a medium-grained (median grain size is 400 micron), well sorted (coefficient of uniformity, D60/D10 = 450/200 = 2.25) sand. This material was obtained from a local hardware store.

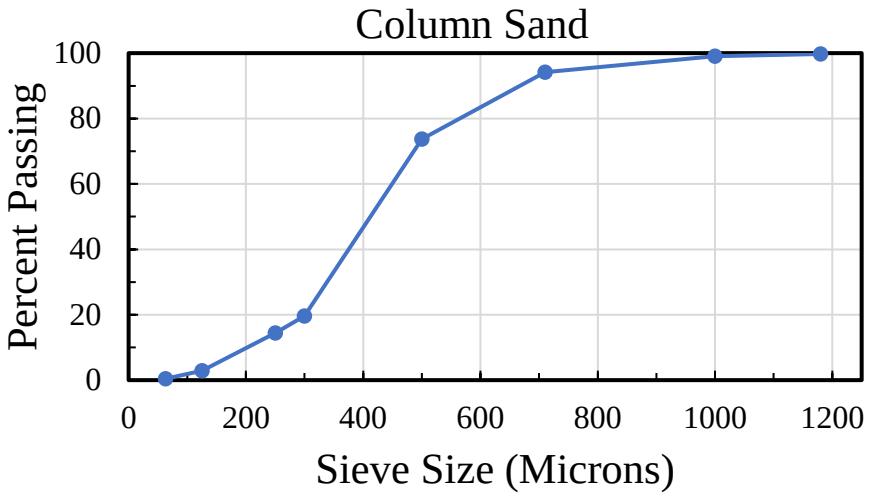

Figure 10: Grain size distribution for the sand used to fill the column.

Middle Layer Gravel

The gravel separates the column sand from the injection gravel. 4000 grams was sorted using 250, 300, 500, 710, 1000, 1180, 2000, and 2830 micron sieves. The distribution of gravel sizes is shown in Figure 11. The separation gravel is what forms the layer between the injection gravel and the column sand. It is made of commercially available well pack sand.

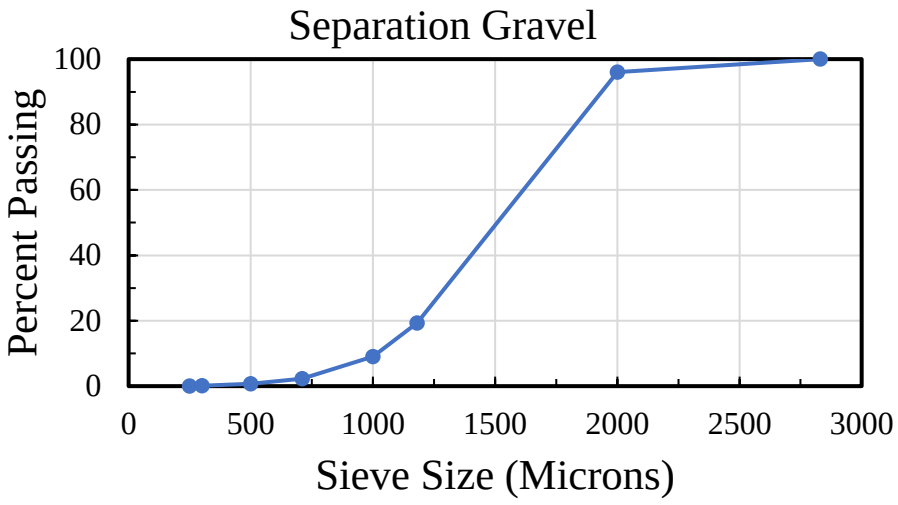

Figure 11: Grain size distribution for the separation gravel layer.

Injection Layer Gravel

This layer is where the water is injected from a peristaltic pump. 4500 grams was sorted using 300, 500, 710, 1180, 2000, 2830, and 4000 micron sieves. The distribution of gravel sizes is shown in Figure 12. The median grain size for the gravel is considerable larger than that of the sand. The hydraulic conductivity of this gravel layer should also be much higher.

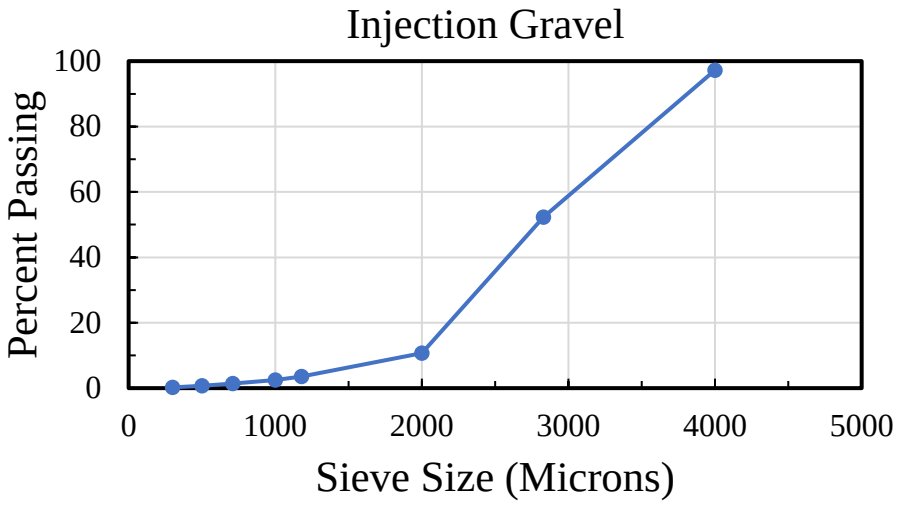

Figure 12: Grain size distribution for the gravel used as the injection site for the column.

DRY BULK DENSITY

The dry bulk density of the medium-grained sand used in the experiments was measured as loose, unpacked material, and after packing and gentle agitation similar to that used when the column was packed. The tests were completed three times and the results indicate that the bulk density of the loose sand in an air-dry condition is 1.54 +/- 0.02 gm/ml. The bulk density of the same material after packing is 1.64 +/- 0.02 gm/ml. Packing increases the density by approximately 6 percent.

WATER RETENTION CURVE

The soil water retention curve (SWRC) is important to determining how water is stored in the column. The SWRC was measured using a hanging column and aspects of the procedure outlined in the ASTM standard method for determining the Soil Water Characteristic Curve (ASTM, 2003). A Buchner funnel was used to hold the sand and

prevent air entry when suction was applied. The pressure applied during the experiment was well below this limit. A graduated burette is used to record the volume of water pulled from the sample with drops in head. This gives results accurate to the nearest 0.1 ml.

Two different retention curves were made. One retention curve with the sand in a non-packed state and one with a higher resolution with the sand in a compacted state similar to what is seen in the column.

Curve fitting software (TableCurve 2.0) fitted the results from the experiment to the van Genuchten equation (van Genuchten, 1980), giving the η and α parameter values as well as the θ_s and θ_r. Results are summarized in Table 2.

Ambient Conditions

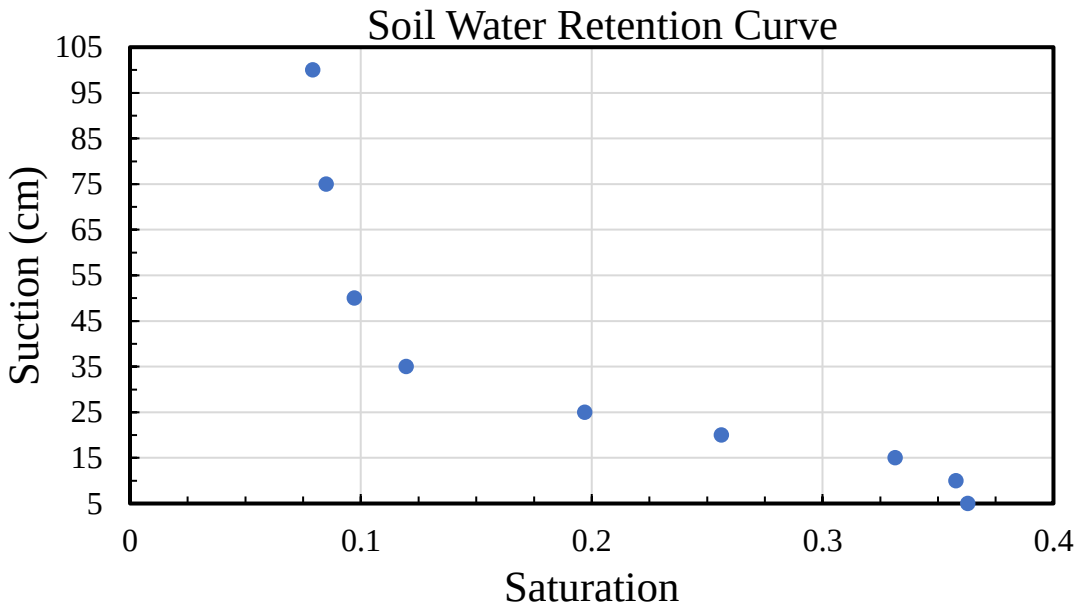

Figure 13: Soil Water Retention Curve under lose sand conditions (porosity of approximately 0.36) and a wide coarse range of suction values.

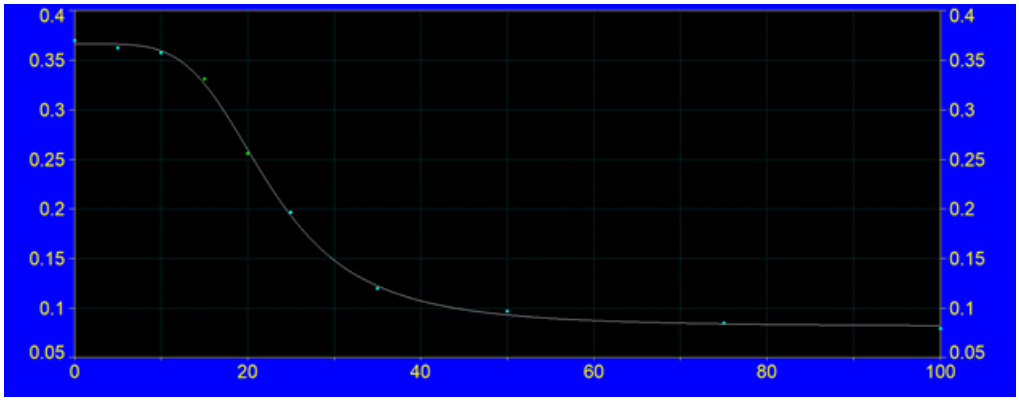

Figure 14: Curvefitting of the van Genuchten equation to the data above. Resultant values are $\alpha = 0.048\ cm^{-1}$, $\eta = 4.65$, $\theta_s = 0.36$ and $\theta_r = 0.08$. Curve fitted using the software TableCurve. $r^2 = 0.999$.

Packed Sand

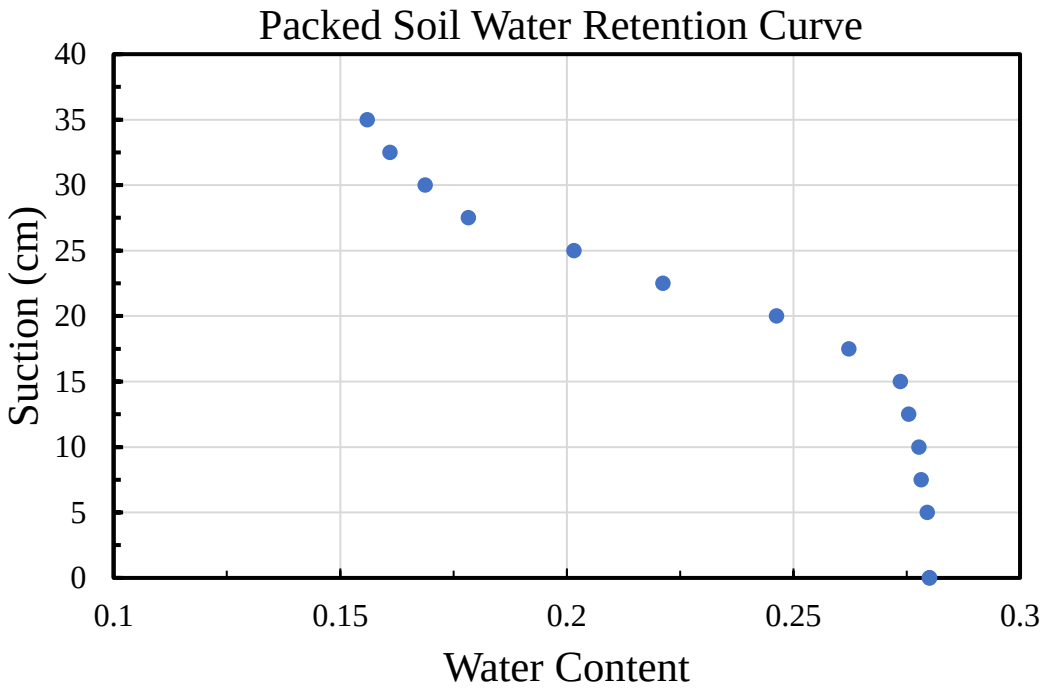

Figure 15: Soil water retention curve with packed sand similar to what is seen in the column. Porosity is approximately 0.28.

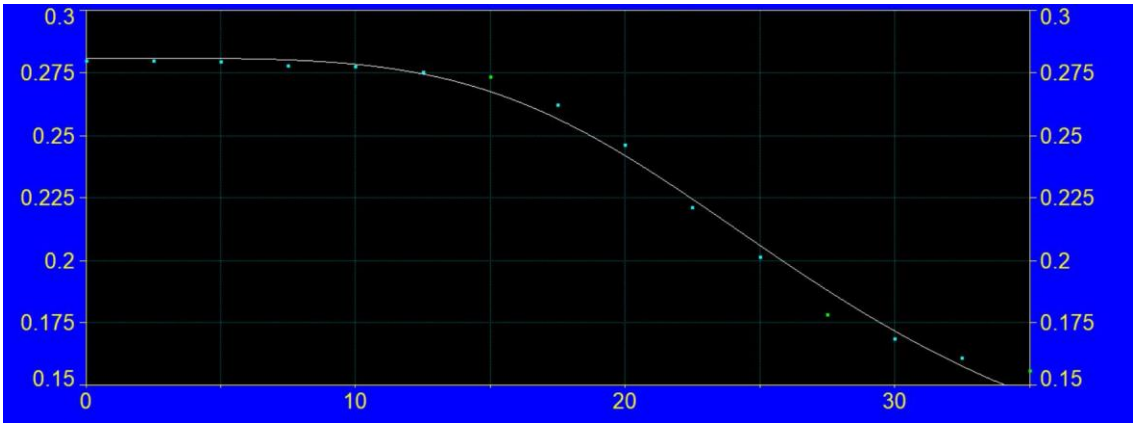

Figure 16: Curvefitting of the van Genuchten equation to the data above. Resultant values are $\alpha = 0.039\ cm^{-1}$, $\eta = 4.34$, $\theta_s = 0.28$, and $\theta_r = 0.08$. Curve fitted using the software TableCurve. $r^2 = 0.990$.

Parameter	Ambient	Packed
α	$0.048\ cm^{-1}$ +/- 0.001	$0.039\ cm^{-1}$ +/- 0.002
η	4.65 +/- 0.05	4.34 +/- 0.1
θ_s	0.36 +/- 0.002	0.28 +/- 0.002
θ_r	0.08 +/- 0.001	0.08 +/-0.005

Table 2: van Genuchten parameters for ambient and packed sand.

ELASTIC MODULI

A staged quasi-consolidated drained (QCD) triaxial shear test was performed to estimate the elastic modulus. The specimen was prepared by gently hand tamping the material in an air-dry state into a membrane-lined vacuum split mold. The mold with porous stones and end caps on the top and bottom of the tamped material was placed on the base of a triaxial cell. A vacuum was applied to the bottom of the sample before

releasing the mold-membrane vacuum and removing the mold. The triaxial cell was then filled with water and the mold vacuum was released.

The test was conducted in stages under loading conditions similar to the experiments. Each stage involved loading the specimen, under a given effective confining stress, at a target strain rate of 0.003 in/hr to a target 0.07% shear strain. All testing was performed under drained conditions. A formal saturation and consolidation stage, as would be performed in a consolidated drained triaxial shear test such as ASTM D7181, was not performed at any stage of the testing. However, the material was gently 'saturated' in the second stage and some consolidation occurs as a function of an applied effective confining stress and load. Thus, this testing is referred to as staged 'quasi-consolidated' drained triaxial shear testing.

The first stage was performed with the material at the as prepared air-dry state under 0.5 psi effective confining stress. Upon completion, the specimen was unloaded to a load equal to the effective confining stress.

The material was then 'saturated' by injecting de-aired water into the specimen, from bottom to top, using a small pressure head (burette water column with no backpressure). The specimen was considered 'saturated' after at least one pore-volume of water was passed through the specimen, assuming 28% porosity.

The effective stress was maintained at 0.5 psi for the second stage, and the specimen was once again deformed to 0.07% strain. Upon completion, the specimen was unloaded until the load was equal to the effective confining stress (0.5 psi at this stage).

The effective stress was then increased to 2 psi, sheared to 0.07% strain, and unloaded to the effective confining stress (2 psi at this stage) for the third stage. This process was repeated under 5 psi and 15 psi effective confining stresses for the fourth and fifth stages. Each stage was terminated at 0.07% strain.

The axial strain was essentially a linear function of the axial stress during all the tests, suggesting that the tests were within the elastic range of the sand. The slopes of axial stress as a function of axial strain were measured for the different stages, and the slopes were assumed to be the effective Young's modulus. The results (Figure 17-22) range from 18 to 40 MPa. The modulus increases with confining pressure, and the modulus of the saturated sand is less than that of the air-dry sand (Table 3).

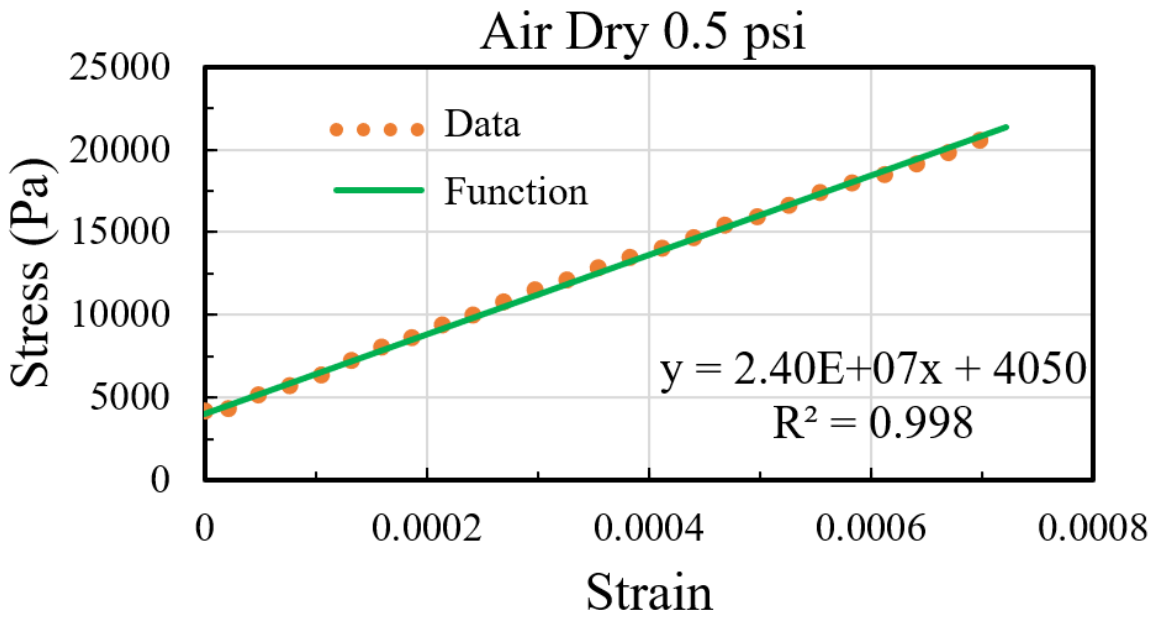

Figure 17: Stress and strain during triaxial test. The Young's Modulus is 24 MPa.

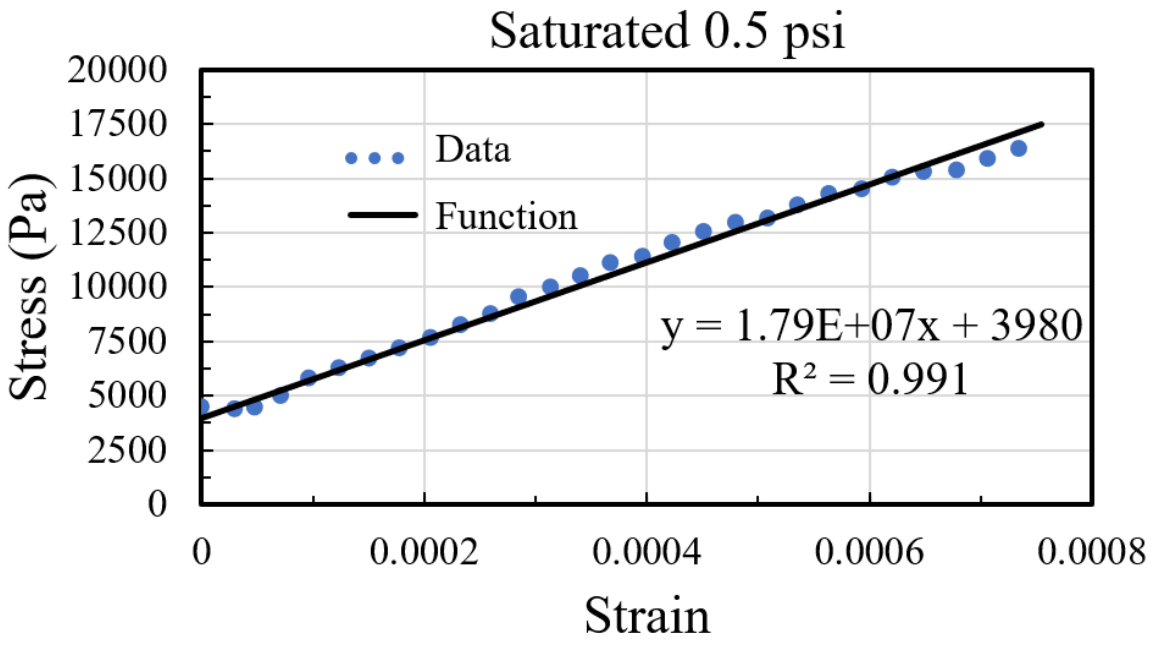

Figure 18: Stress and strain during triaxial test. The Young's Modulus is 18 MPa.

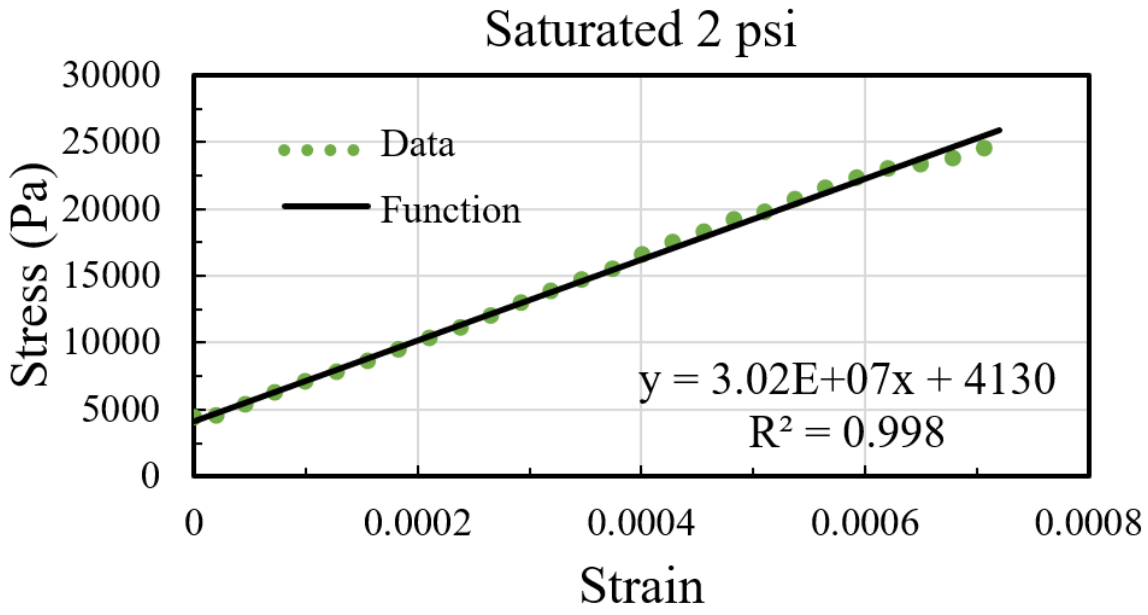

Figure 19: Stress and Strain during triaxial test. The Young's Modulus is 30 MPa.

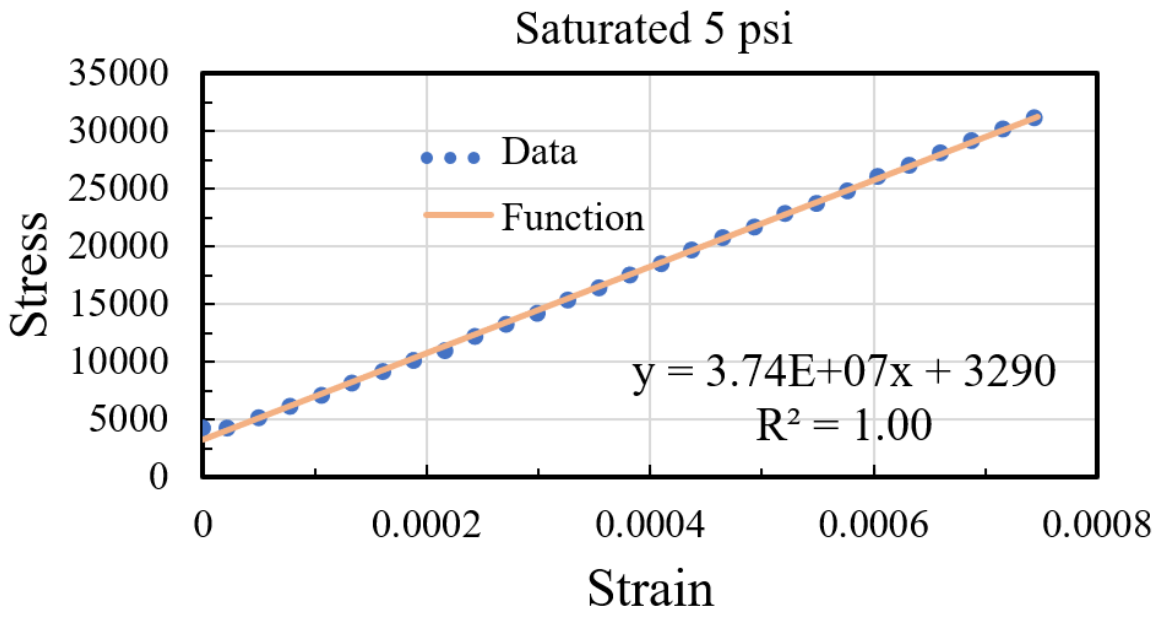

Figure 20: Stress and strain during triaxial test. The Young's Modulus is 37 MPa.

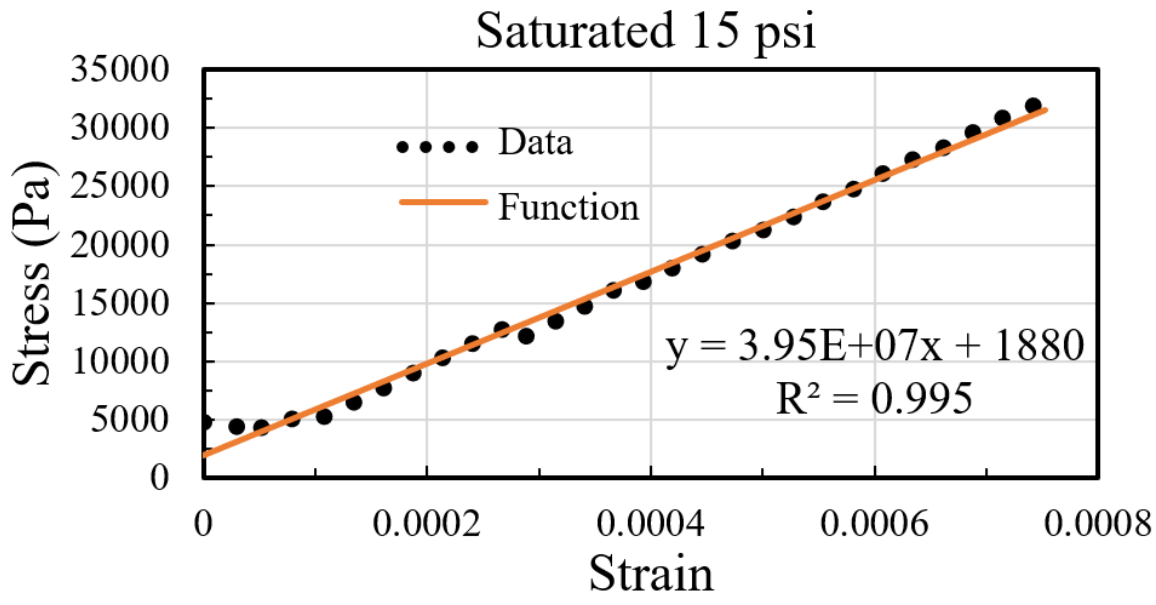

Figure 21: Stress and strain during triaxial test. The Young's Modulus is 40 MPa.

Confining Pressure	Young’s Modulus
0.5 psi “Air-Dry”	24 MPa
0.5 psi Saturated	18 MPa
2 psi Saturated	30 MPa
5 psi Saturated	37 MPa
15 psi Saturated	40 MPa

Table 3: Young's Modulus values for various confining pressures.

CHAPTER FOUR: COLUMN LOADING

COLUMN LOADING TEST

Strain was measured at five intervals in the sand, and at five intervals along the outer wall of the pipe. The strain was measured as displacement between two reflectors separated by 10 cm. This gives the strain averaged over a 10-cm-long interval. The midpoints of the reflectors occur at distances of 15, 25, 35, 45, 55 cm above the base of the column, and the sand extended to a height of 72 cm. The total height of the column is 75 cm.

The column was loaded with weights and the strain was measured in the sand and in the wall of the column. The load was applied by placing weights on a polystyrene cylinder with a diameter that is approximately 1 cm less than the inside of pipe. A 2.5-cm-wide slot was cut along the radius of the loading column and the strain ribbon was put in the slot during loading. This allowed the load to be applied without contacting the strain ribbon. Steel disks were placed on the loading cylinder to generate forces of 1.4, 2.8, 5.4 and 11.4 N. A loading test was conducted by placing steel disks on the loading cylinder, measuring the strain at each reflector pair for approximately 5 seconds. Then the weights were removed for 5 seconds, and the test was repeated approximately 10 times. This produced a step-like time series of increasing and decreasing strain. Trends in the strain also occurred during the test, presumably because of temperature changes. The average strain resulting from the applied load was determined with a trend lines that were manually fit to the upper and lower steps in the time series.

Four suites of tests were conducted using loads applied to dry sand soon after the column was filled. Three suites of tests were conducting later when the sand was completely saturated. Additional tests were conducted by applying load to the wall of the column instead of on the sand. The tests are named for where the load was applied (LS=load on sand; LW=load on wall) the moisture state of the sand (DS = dry sand, WS = wet and fully saturated sand) and the applied load in grams force. So, test LS-DS-560 applied a weight of 560 g to the dry sand.

Observed Strains

The strains at a particular elevation increased with the applied load. This is the expected response, so the strains were normalized to the applied load to facilitate plotting (Figure 22). The strain in the sand increases markedly with elevation in all the tests. Strains in the saturated sand are generally greater than strains in the dry sand at the same elevation. The maximum ratio is approximately 0.7 1/N at the upper end of the column when the sand is saturated, and the ratio decreases to approximately 0.1 1/N at lower end of the column (Figure 22).

In contrast, the strain ratio in the wall of the column ranges from 0.02 to 0.1 1/N. The strain ratio in the wall appears to be independent of elevation and there appears to be negligible difference between tests using dry and saturated sand (Figure 23).

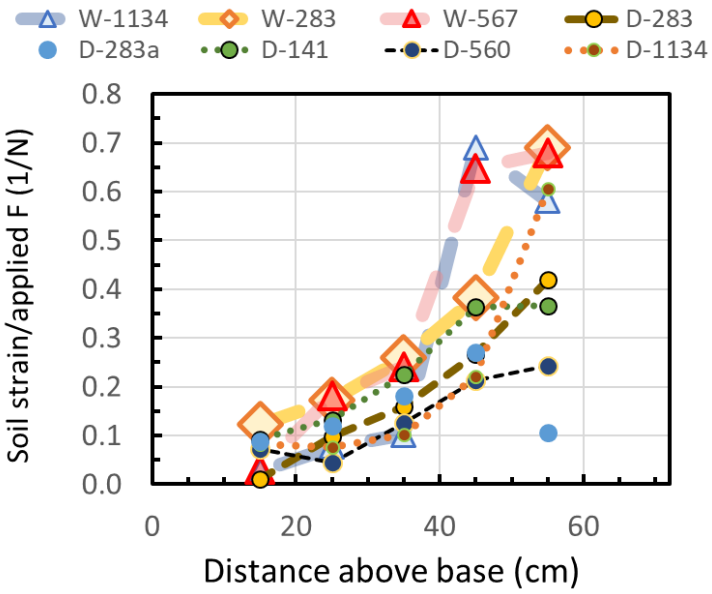

Figure 22: Ratio of the strain in sand to the applied force as a function of distance above the column base for tests with different applied loads and different saturation states (D=dry; W = saturated). The x axis extends over the full height of the column.

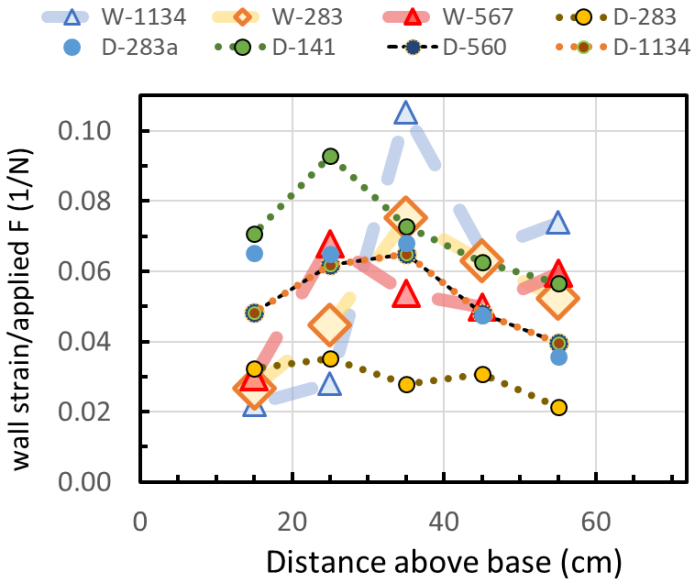

Figure 23: Ratio of the strain in wall of the PVC column to the applied force as a function of distance above the column base for tests with different applied loads and different saturation states (D=dry; W = saturated). The x axis extends over the full height of the column.

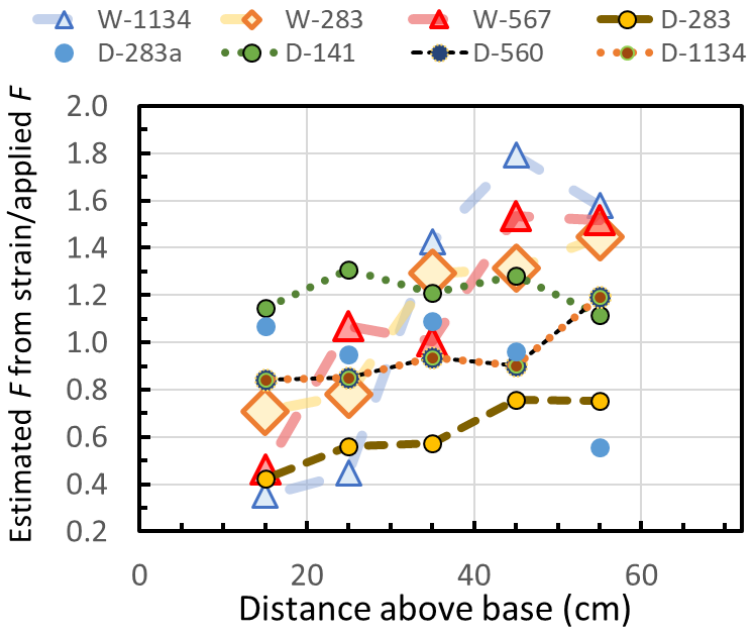

Figure 24: Ratio of the total force estimated from the strain to the applied force as a function of distance above the column base for tests with different applied loads and different saturation states (D=dry; W = saturated). The x axis extends over the full height of the column.

Estimated force

It was assumed that the applied force was uniformly distributed at a particular elevation within the sand and also within the PVC column. It was also assumed that the applied force could transfer from the sand to the PVC column. So, for example, the fraction of the load carried by the sand could increase if the fraction carried by the column decreased with elevation, providing the total force summed to the applied load. A force balance indicates that the average force in the sand at the elevation of sensor *i* is

$$F_{si} = \varepsilon_{si} E_i' A_c \qquad (19$$

where ε_{si} is the strain in the sand at sensor *i*, E_i' is the effective elastic modulus at sensor *i*, and A_c is the cross-sectional area of the column (0.0314 m^2). The average force in the wall of the column is

$$F_{wi} = \varepsilon_{wi} E'_{PVC} A_w \quad (20$$

where ε_{wi} is the strain in the sand at wall sensor *i*, E_{PVC}' is the effective elastic modulus of PVC, and A_w is the cross-sectional area of the wall (0.0066 m^2).

The total force at the elevation of each sensor is assumed to equal the force generated by the applied weight

$$F_a = F_s + F_w \quad (21$$

We assumed that the effective elastic modulus of the sand could vary with depth as a result of packing, interaction with the wall, or other factors. The effective modulus of the PVC wall was assumed to be uniform.

A series of optimization analyses was conducted by determining the elastic moduli E'_{PVC} and the five E'_{si}. The objective function was the sum of the squared residuals between the applied force and the sum of *Fs+Fw*. Analyses were conducted for all the test conducted using wet sand, all the tests conducted using dry sand, and all the tests as an aggregate.

The elastic modulus of the PVC pipe is in the range of 2 to 3 GPa, whereas the sand is in the range of 5 to 30 MPa according to the results. The results also indicate that the force carried by the PVC column can be greater than that in the sand, even though the

weight was applied to the sand. The ratio of $F_s/F_{applied}$ is generally less than 0.2, and it is less than 0.1 at the bottom of column, according to the analysis. The ratio F_w/F_s decreases with elevation, which is consistent with Figure 22.

The ratio of $(F_w+F_s)/F_{applied}$ typically increases with elevation and it generally ranges between 0.4 and 1.6 (Figure 24). Ideally, this ratio would equal unity.

The optimization analysis estimates an effective elastic modulus, *E'* at each depth. Assuming the PVC column restricts horizontal strain to zero, vertical force is related to the vertical strain according to uniaxial Hooke's Law (Wang, 2000) using

$$F_a = A_s\sigma_{zz} = A_s\frac{E}{(1+\nu)}\frac{(1-\nu)}{1-2\nu}\epsilon_{zz} \quad (22$$

$$F_a = E'A_s\epsilon_{zz} \quad (23$$

$$E' = \frac{E}{(1+\nu)}\frac{(1-\nu)}{1-2\nu} \quad (24$$

$$E = C_1E' \quad (25$$

$$C_1 = \frac{(1+\nu)(1-2\nu)}{(1-\nu)} \quad (26$$

Assuming the Poisson's ratio for sand ranges from 0.25 to 0.4 implies that C_1 ranges from 0.83 to 0.47, and using ν=0.3 gives C_1 = 0.75. This allows Young's modulus to be estimated from the strain data (Figure 25). The results indicate that Young's modulus decreases slightly from the middle to the top of the column. Estimates based on all the data are in the range of E_s =15 MPa to 20 MPa, and E_{PVC} =2.4 GPa. Estimates using only the data from dry sand indicate a stiffer modulus for sand, in the range of E_s =

30 MPa, and E_{PVC} =2.2 GPa. In contrast, estimate using only the data from wet sand indicate a softer modulus for sand, in the range of E_s =5 MPa to 10 MPa, and E_{PVC} =2.4 GPa.

The results of the loading tests are consistent with both general published values and those measured using geotechnical tests. Published estimates for the Young's modulus of loose sand range from 10 to 80 MPa depending on axial strain (Satoshi Yamashita,1 Michele Jamiolkowski, 2000). Values for *E* of PVC pipes range from 2.4 to 2.9 GPa, according to (Neelam & Kalaga, 2002). The Young's modulus of saturated sand used in the experiments ranged from 18 to 30 MPa as the confining stress increased from 0.5 psi to 2 psi in a triaxial test, which is consistent with the average values of *E* from the loading tests (Figure 22). The triaxial tests indicated that Young's modulus of wet sand is less than (approximately ¾) that of dry sand. The loading tests also indicate that dry sand is stiffer than wet sand, although they indicate the difference between the dry and saturated conditions is larger than it was in the triaxial tests.

The results of the loading tests indicate that the strain measured by the optical fiber ribbon is approximately equal to the values expected from elastic deformation of sand in a tube of PVC. This is an initial confirmation that the strain data measured by the optical fiber is meaningful. The results also indicate that there is significant interaction between the load carried by the sand and the enveloping PVC tube, and this interaction will affect the results of strain measurements in the sand. This interaction likely accounts for much of the variability in the strain data, and uncertainty in moduli estimates.

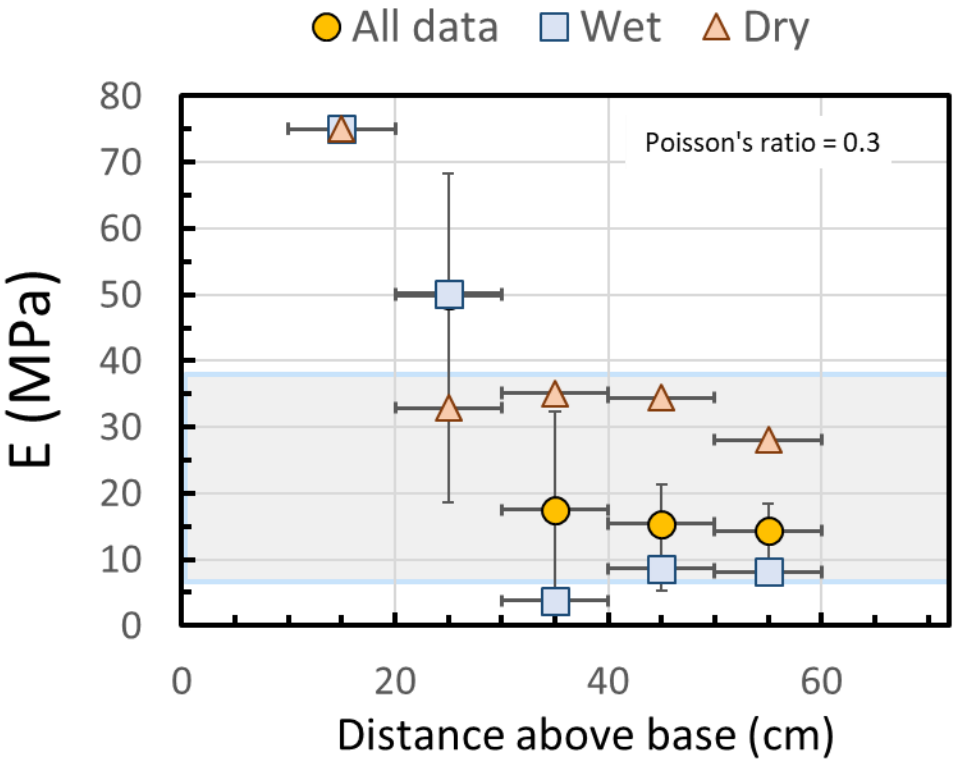

Figure 25: Young's modulus of sand using parameter estimation that requires internal forces to sum to the applied force. $\nu = 0.3$ is assumed. Grey band is the range of moduli in the mid to upper parts of the column.

CHAPTER FIVE: POROELASTIC TESTS

A suite of tests was conducted by increasing saturation and then draining the column while measuring pressure and strain. These were conducted in two ways, either by injecting into the base of the column or by infiltrating from above. The water was then either drained by gravity or pumped out of the column. Strain, pressure, temperature, and mass of water injected/drained were measured. The water used for injection was taken from tap and was left overnight in a basin, so the water temperature equilibrates with the room temperature. This was done to minimize strain due to temperature fluctuations in the column.

The suite of injection tests includes four tests where water was injected at 0.1 L/min for approximately 2,000 seconds to completely fill the column and cause ponding at the surface of the sand. One test was conducted where water was injected for approximately 1,600 seconds to partially fill the column. The tests were conducted over a three-month period, from October 2019 to January 2020, with several days to several weeks between each test. An initial goal was to evaluate the effects of completely filling the column, but it was realized near the end of the testing program that it would also be useful to have results from a test where the column was partially filled to avoid complications that occurred when the water level approached the top of the column. Only one of the partially filled tests was completed because of time constraints, but it provided a useful baseline and will be described first.

PARTIAL-FILL INJECTION TEST

An injection test was conducted to evaluate the strain response during injection and drainage without incurring effects associated with the injected water reaching the surface. The test was conducted 28 days after the previous injection test and the initial hydraulic head was nearly uniform over the height of the column, indicating no flow and that the water was in gravity equilibrium.

The test consisted of injecting at a constant rate for 1,610 s (27 min), shutting off the pump for approximately 600 s (10 min) and then starting it again in reverse at t =2,277 s (38 min). The water level in the sight tube attached to the bottom of the column started at an elevation of 11 cm and it was at 47 cm after the pump was turned off at the end of the test. This was sufficiently below the surface of the sand (elevation of 72 cm) so the interaction between the wetting front and the sand was expected to be minimal. The pump was turned on and off two more times, once between t =4,500 s and 4,700 s, and again between t =5,300 s and 5,400 s.

Results

Filling the column with water generally caused pore pressure and axial strain to increase (become more tensile), and these trends reversed during draining. These are the expected effects, but the details of the pressure and strain responses vary among the different sensors and lead to some insights about the filling and draining process.

Pore pressure

Pore pressure was measured using tensiometers in the column that were connected to transducers at a common datum below the bottom of the column. As a result, the pressure measured at the transducers was proportional to the total head. The pore pressure head at the tensiometers was determined by subtracting the elevation head from the measurements made by the transducers. The transducer locations were determined by measuring up from the bottom of the column, and this measurement is used in the name of the transducer. The bottom of the column was 0.5 cm above the transducers, so the elevation head used to convert total head to pressure head used the transducer location plus 0.5 cm.

The pressure head at the start of the test was -30 cm at the p44 tensiometer and +11.3 cm at the bottom tensiometer (p6) (Figure 27). The pressure heads at the lower three tensiometers are roughly linear with a gradient of 1.1. This is slightly greater than the expected value of 1.0 during hydrostatic conditions. The difference is probably because of a slight offset in the transducers. The pressure head at the p44 tensiometer is approximately 8 cm above the projection of 1.1 gradient at the start of the test. This is probably because the p44 tensiometer was filled before the test and water from the porous cup elevated the head. Data from the p60 sensor was erratic during this test, so those data are omitted.

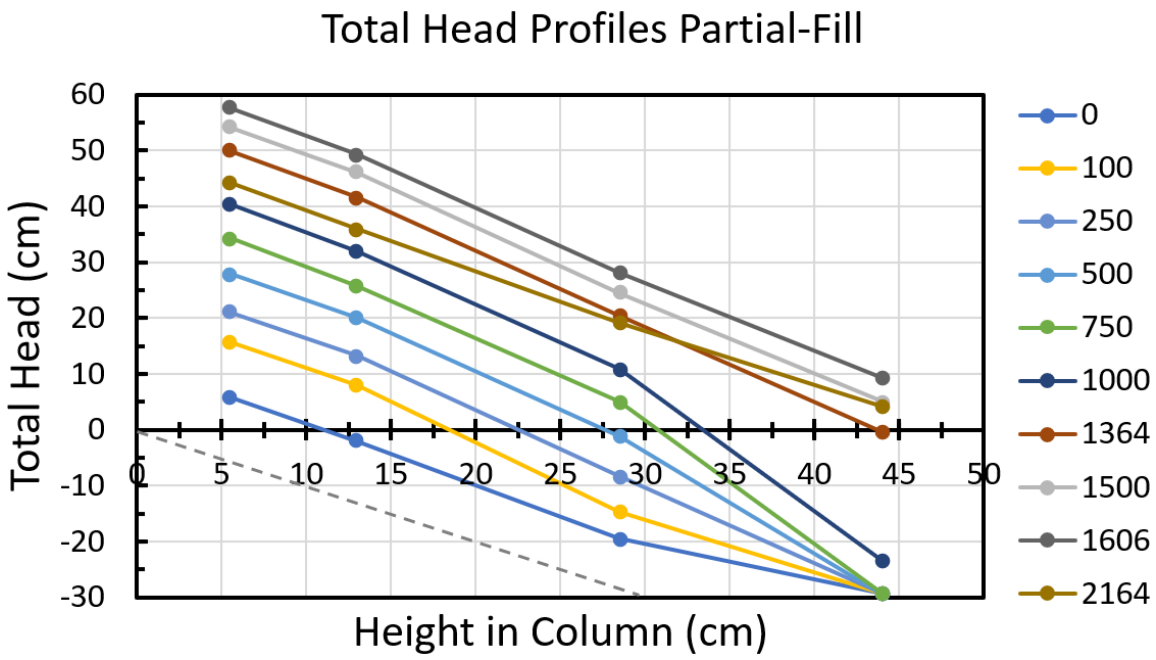

Figure 26: Pressure head profiles at different times during the partial-fill injection test. The times in seconds relative to turning on the pump are shown in the legend. The dashed line is a reference with a slope of -1.

The pressure head gradient increased from 1.1 before injection to approximately 1.3 during injection (Figure 26). The heads in the bottom three sensors increase with time, but the gradient is similar. This indicates that the total head gradient change due to pumping is approximately 0.20 during injection. The volumetric flux is ($Q = 1.66 \times 10^{-6}$ m^3/s); $A = 0.031$ m^2, 5.4×10^{-5} m/s, which indicates a saturated hydraulic conductivity of 2.7×10^{-4} m/s. This is consistent with independent measurements of *K* (Figure 9).

The pressure head increases at the 28 cm sensor within a few tens of seconds after the start of injection, and it increased at the sensor 44 cm approximately 800 s later. This indicates the pressure was propagating and at rate of approximately 16 cm over 800 s, or 0.02 cm/s. The elevation change in the equilibrium head was 39 cm during injection, and it occurred over 1,600 seconds, which is an average rate of rise of 0.024 cm/s. The

ratio of the flux/velocity 0.54/2.0 = 0.27 is the average fillable porosity, which is consistent with the retention curve.

The elevation of the point of zero pressure (PZP) corresponds to the height of the water table in an aquifer and can be identified by interpolation of the data in Figure 26. The elevation where the pressure profiles cross the zero-pressure axis is the PZP. The PZP is at 12 cm initially, and it is at 32 cm after 750 s, according to Figure 27. The PZP was determined at different times as one measure of how the pressure propagates up the column.

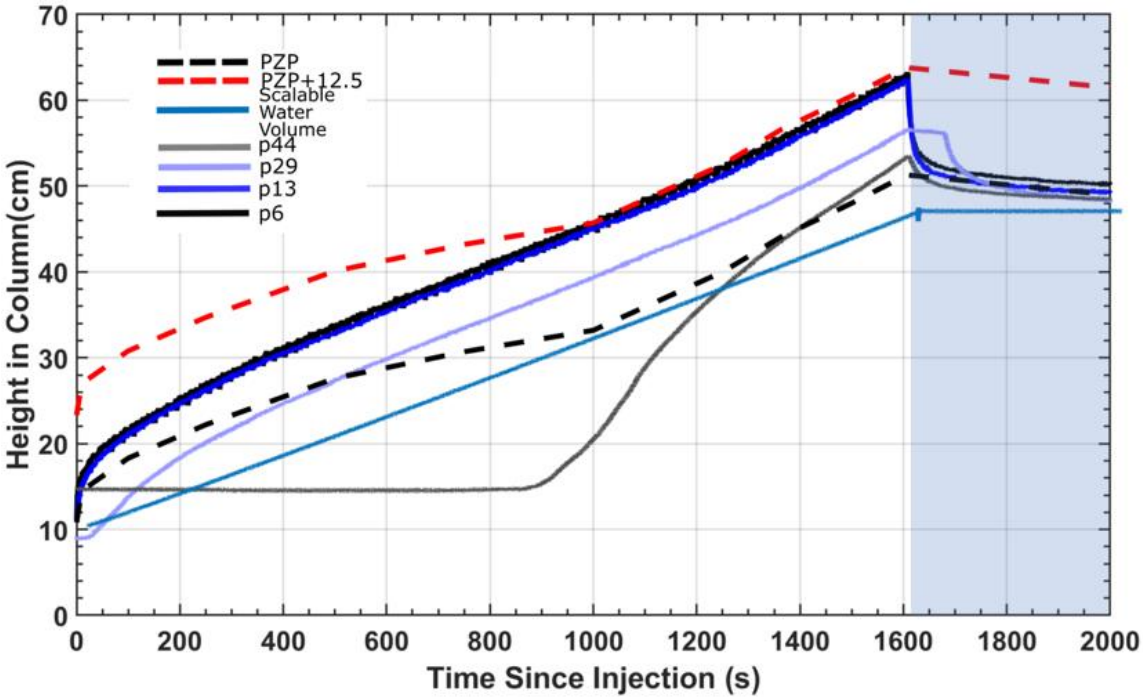

Figure 27: Pressure head, scaled water volume, and transition zone (PZP to PZP + 12.5 cm) height as functions of time for the injection portion of the infiltration fill-up test. Blue band is the period of no-flow

The time series of the total head (Figure 27), the data measured at the horizontal bank of transducers for the lower three transducers (p6, p13, p29), starts at essentially the

same value of 11 cm, which is consistent with equilibrium conditions (Figure 26). The total head increases first at the bottom and then the transducers that are progressively higher in the column increase. The total head increases sharply during the first tens of seconds, but then the rate drops to approximately 0.022 cm/s (2.2 Pa/s) at the bottom transducers (p6, p13 and p29) and this rate is roughly constant during injection. The total head is unchanged initially in the upper transducer, p44, but it rapidly increases to approximately 0.05 cm/s (5 Pa/s) at approximately 850 seconds.

The weight of the injected water was determined with a load cell and those data are plotted on Figure 27 using normalization. The normalization procedure involves converting the weight to volume of water and dividing by the cross-sectional area of the pipe, *A*. This value was then divided by the average fillable porosity, which was determined from tests where the water level reached the surface of the sand. In those tests, the average fillable porosity was determined as

$$n_f = \frac{V_t}{A(h - hi)} \qquad (27$$

where n_f is 0.25, h_s is the total height of the sand in the column, h_i is the initial height of the water level in the column, and V_T is the total volume injected when the water level reaches the surface of the sand. The normalized volume of water is

$$V = An(h - h_i) \qquad (28$$

The rate of injection was constant, so the normalized volume of injected water increases linearly with time, is steady when the pump is turned off, and then decreases linearly with time during the pumping out portion of the test.

The PZP was determined by interpolation at multiple times and compiled into a time series. These data show that the PZP started at an elevation of 12 cm and moved upward during filling to a maximum height of 51 cm, and then it dropped during draining (Figure 28). It generally followed the scaled water volume, but there are systematic variations. For example, the PZP rises faster than the volume curve at the beginning of injection and it is 6.5 cm above the curve after 100 seconds. However, the PZP flattens and falls below the volume curve with time (Figure 28). This behavior is reasonable because the volume curve is normalized to the average fillable porosity. The fillable porosity is less than the average near the bottom of the column, whereas it is greater than the average near the top of the column because the water content has redistributed by gravity drainage prior to the test. The PZP is at approximately 32 cm at t =850 s, and the data indicate (Figure 26) that the pressure at p44 first starts to change at this time. This indicates that the zone where the pressure transitions to ambient is approximately 12 cm high.

The PZP reaches a maximum elevation of 51 cm when the pump is turned off. The data indicate that the maximum height of transition zone is approximately 12 cm higher at 63 cm. This is approximately 9 cm below the surface of the sand, ensuring that there is negligible pressure interaction with the surface.

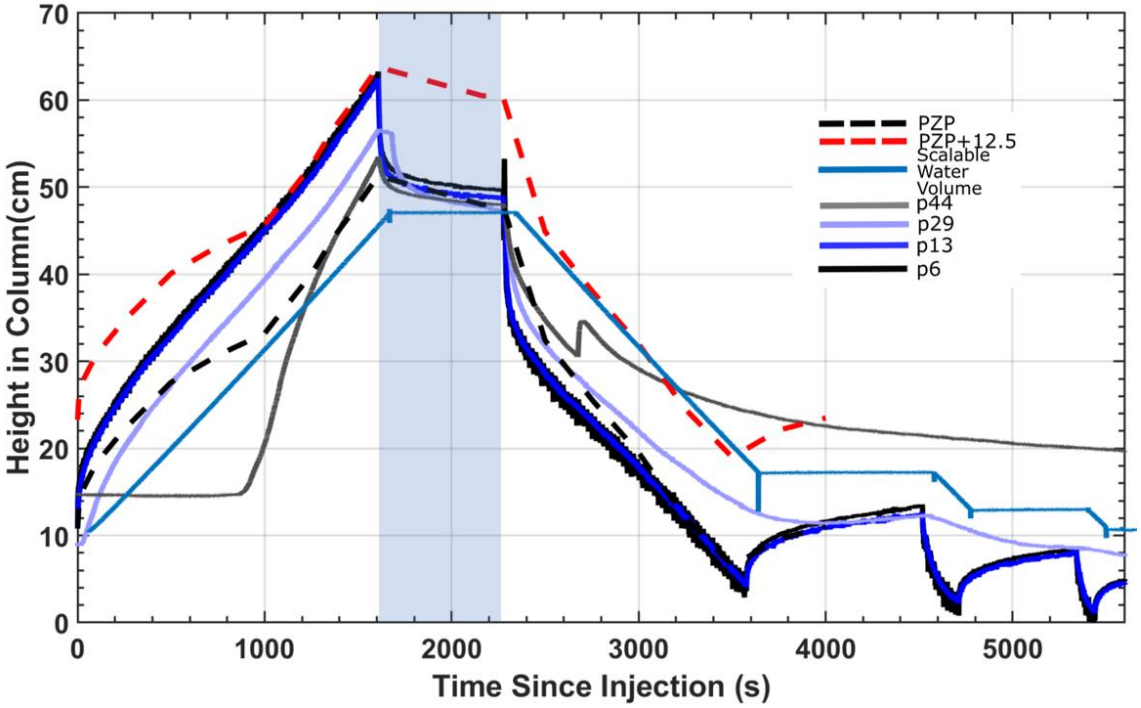

Figure 28: Total heads (solid lines), scaled water volume (straight blue line), and transition zone (PZP to PZP + 12.5 cm) height as functions of time for the partial-fill test. Blue band is the period of no-flow.

The data from the transducers indicates that there are three main zones defined by pressure during imbibition; 1.) Ambient, 2.) Transition and 3.) Positive. In general, where the pore pressure is initially negative, the pressure remains at ambient conditions and then it increases sharply when the transition zone arrives. The rate of pressure increase diminishes when the pressure becomes positive. The pressure and head gradients are steeper in the transition zone than in the ambient and positive pressure zones (Figure 26). These profiles indicate the transition zone is between 10 cm and 15 cm wide. Combining this with other pressure data, an average value of 12.5 cm is used for the height of the transition zone.

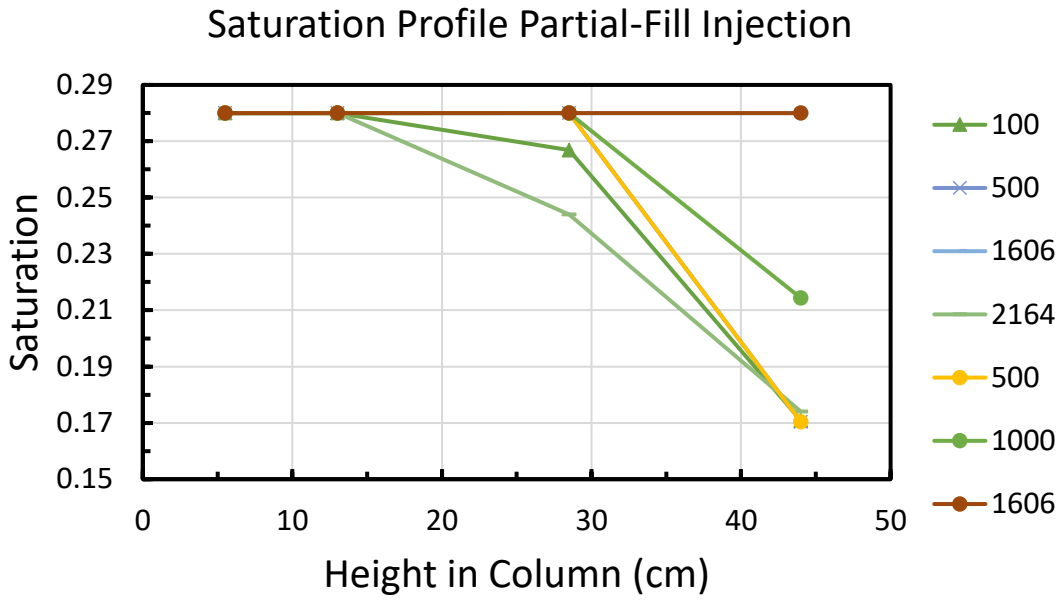

Figure 29: Saturation profile during partial fill injection determined using the retention curve in Figure 15. The times in seconds relative to turning on the pump are shown in the legend.

The pressure data along with the retention data can be used to estimate the water content as a function of elevation. The sand at the p6 and p13 tensiometers is completely saturated at the start of the test (Figure 29). The water content at p29 is 0.24 and at the p44 transducer has an initial saturation of 0.17. The maximum change in water content is approximately 0.1 and occurs at the top sensor, p44. All sensors are saturated at the end of injection t =1,600 s.

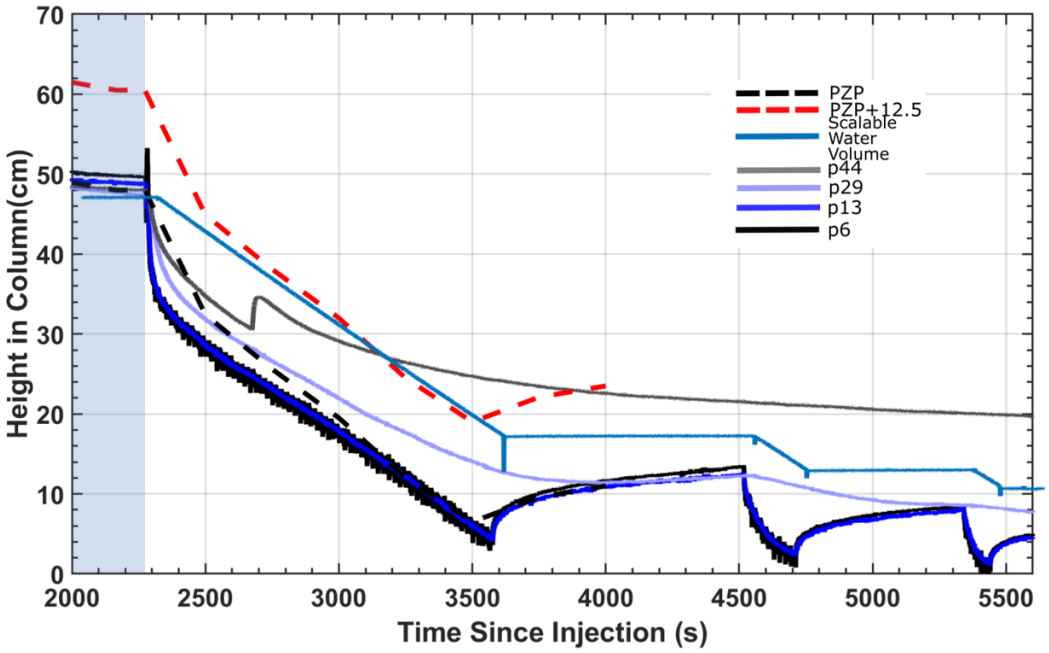

Figure 30: Total head, scaled water volume, and transition zone (PZP to PZP + 12.5 cm) height as functions of time for the drainage portion of the infiltration fill-up test. Blue band is the period of no-flow.

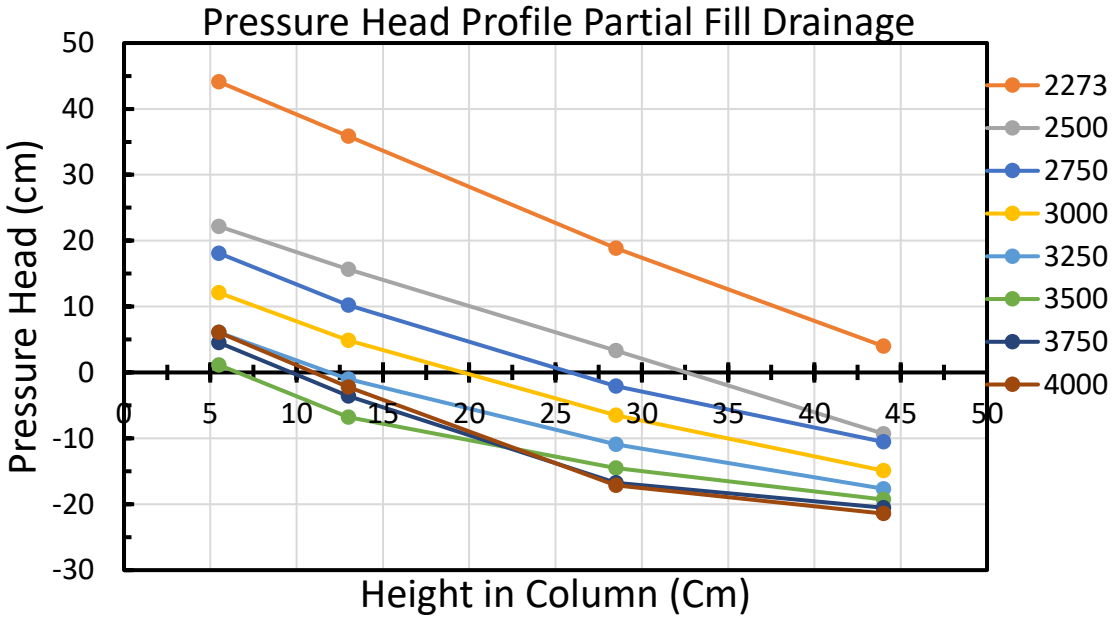

Figure 31: Pressure head profiles at different times during the drainage portion of the partial-fill injection test. The times in seconds relative to turning on the pump are shown in the legend.

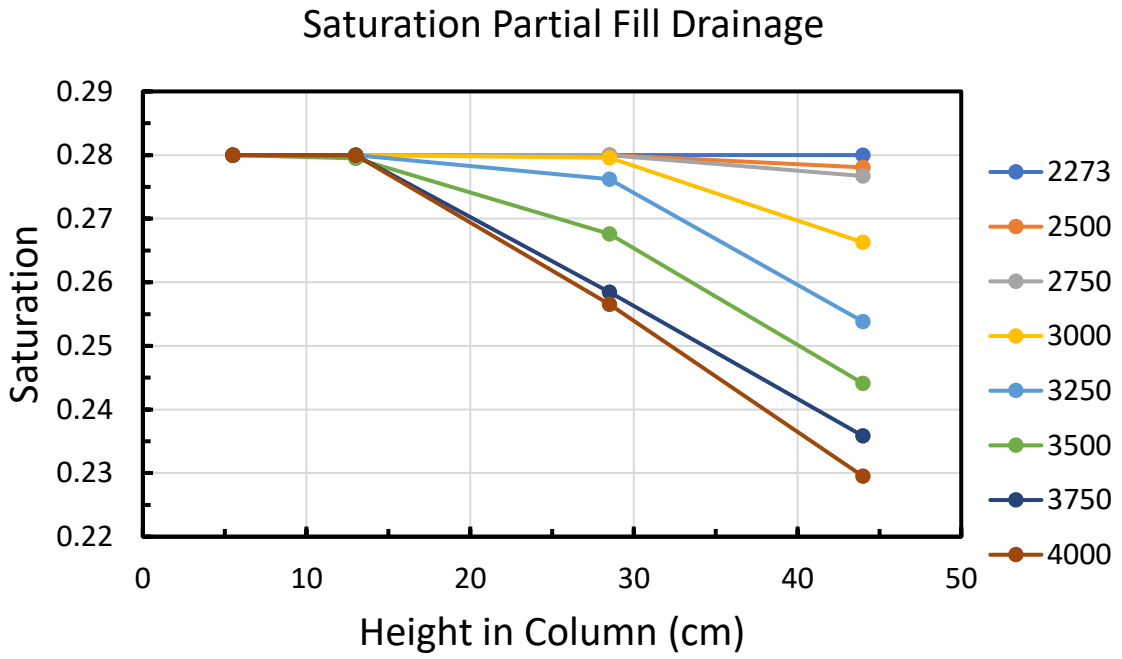

Figure 32: Saturation profile partial fill drainage. The times in seconds relative to turning the pump on at the start of the test are shown in the legend. P5 and p13 are almost fully saturated throughout the test.

Pumping out from the base of the column initiates drainage and causes a rapid pressure decrease for approximately 20 seconds (Figure 30). After this period, the pressure in p6 and p13 begin dropping at a rate of 0.023 cm/s. The pressure at p29 drops at a similar rate that diminishes over time. The pressure at p44 initially follows the similar rate but it also slows from this trend. The pressures at p28 and p44 lags that of the lower two transducers and the rate of drop diminishes, particularly when the PZP drops below the level of the tensiometer. The initial drop in head is consistent with the development of a vertical head gradient of 10/40=0.25, which is similar to the 0.2 head gradient determined during filling. The PZP also drops rapidly during the first tens of

seconds, but this rate diminishes and approaches the 0.02 cm/s rate recorded by the transducers after a few hundred seconds of pumping out (Figure 30).

Water is pumped out of the column for approximately 1,000 s and the pump is turned off at t = 3,600 s. The total head at p6 and p13 increase abruptly when the pump is turned off, but there is only a slight effect at p28 and negligible effect at p44 (Figure 30). A head increase of approximately 5 cm occurs in a few seconds, but the head continues to rise at a slower rate for nearly 1,000 seconds. The rapid initial increase in head likely occurs as the head gradient flattens when the flow stops. Water will continue to drain out of the partially saturated sand, and this is assumed to cause the continued rise in head at p6 and p14 and the slight drop in head at p29 (Figure 30).

The scaled water volume is higher than the pressure heads at the lower three tensiometers (p6, p14, p29) and less than the pressure head at p44. The PZP is slightly higher than the pressure head at the lower pressure sensors at earlier drainage times but begins to follow it after 800 seconds of drainage (t = 3,100 s).

The head continues to drop at p44 and p29 after the pump is shut off and this causes the water content to decrease (Figure 32). At 4,000 s the water content reaches a low of 0.23 in p44. Water content at p29 drops to 0.26 at t = 4,000 s. Sand at p13 and p6 remain almost fully saturated during drainage.

Turning on the pump causes an abrupt change in head as the hydraulic head gradient of 0.2 to 0.25 becomes established. After that, the head advances at a rate of approximately 0.02 cm/s, which is consistent with the velocity expected from the flow

rate and average fillable porosity. This corresponds to a pressurization rate of 2 Pa/s. The head gradient is negative and induces upward flow during injection, it goes to zero when the pump is turned off. The total head gradient changes sign and causes downward flow when the pump is reversed. The head gradient caused by the pump dissipates within 100 to 200 seconds after the pump is turned off, and this causes the head to stabilize. However, gravity drainage occurs when the pump is turned off after pumping water out of the column, and this causes the pressure to increase over a longer time period (at least 1,000 seconds).

Strain

Strain data were recorded between five pairs of reflectors in an optical fiber between 10 and 60 cm above the datum. Elevations of the pressure sensors roughly correspond with the elevations of the strain sensing regions (Figure 1). The PZP was at 12 cm and the top of the pressure transition zone is inferred to occur at approximately 25 cm at the start of pumping. The lowest pair of strain sensors, at 10 cm and 20 cm and labeled "s1020", was within the transition zone at the start, and s2030 also contained part of the transition zone. The height of the transition zone increased to approximately 63 cm during the test. As a result, sensor s4050 was completely below the transition zone at the end of the test, and the interval spanned by sensor s5060 was within the pressure transition zone.

Strain during filling

Soon after the start of pumping, tensile (positive) strain occurred at the lowest two sensors (s1020 and s2030), essentially no strain occurred at the middle sensors (s3040 and s4050) and slight compressive strain occurred at the uppermost sensor (s5060). The tensile strain rate was initially roughly constant (~0.02 με/s) at the lower two (s1020 and s2030) sensors, the rate abruptly decreased after several hundred seconds. In contrast, the strain rate at the other sensor was small initially, but then it progressively increased to approximately 0.02 με/s followed by a flattening, a pattern similar to the strain at the lower sensors. The increase in slope occurs first in s3040, then s4050 followed by s5060. The linear portion of the increasing strain between each pair of sensors can be fit by a curve with the same slope ~0.02 με/s, and the curves are offset by approximately 400 s. The sensors are 10 cm apart, so that indicates the linear portion of the increasing strain moves at a rate of approximately 10cm/400s or 0.025 cm/s. (Figure 33). This indicates the band of linearly changing strain is moving at a rate similar to the velocity of the water.

Strain is expected to increase as the sand dilates due to an increase in pore pressure. The period when the strain increases linearly at each sensor occurs at approximately the time when the transition pressure zone is between the reflectors on the fiber sensor. The pressure increases at approximately 2 Pa/s in the lower tensiometers where the strain rate is approximately 0.02 με/s. Assuming the sand column behaves as an ideal, 1D poroelastic material, the ratio of pressure change to strain leads to

$$C_1 = \frac{1-\nu}{(1+\nu)(1-2\nu)} \quad (29$$

$$\frac{\Delta P}{\epsilon_{zz}} = C_1 E \quad (30$$

where E is Young's modulus, α is the Biot-Willis coefficient, and ν is Poisson's ratio (Wang, 2000). Assuming α is unity and ν could range between 0.25 and 0.45 as a result of changes in saturation constrains C_1 to $1.2 < C_1 < 3.8$. The ratio of the pressurization and strain rates gives $(2.5\ \text{Pa/s})/(2\text{x}10^{-8}\ 1/\text{s}) = 125$ MPa and using C1 leads to an estimate of Young's modulus of $30\ \text{MPa} < E < 100$ MPa, with the lower value associated with saturated conditions. Measurements of Young's modulus during the column loading tests indicate values in the range of $7 < E < 37$ MPa. The values from the triaxial test indicate $18 < E < 40$ MPa, depending on saturation and confining pressures (Figure 17-Figure 21). Each method covers a significant range, but all three indicate $E \sim 30$ MPa.

These results indicate that the periods of linear increase of strain are consistent with the linear increases in pressure that occur simultaneously, but the magnitude of the observed strain rate less than what is expected from Young's modulus measurements measured independently. It is possible that the relatively stiff PVC tube could have caused the sand to behave as if it were stiffer than indicated by the triaxial test. It is also feasible that the effective modulus at the small strains (less than 10 με) that occur during the partial-fill is stiffer than the modulus at the larger strains (greater than 100 με) used in the triaxial test.

The transition zone is bounded by the PZP on the bottom and is assumed to be 12 cm thick, and the position of this zone is related to the strain signal. The position of the pressure transition zone was plotted on the time series (Figure 33) and compared to the strain time series. This shows, for example, that the top of the transition zone (PZP +12.5 cm) is at roughly 35 cm at t = 400 s when the strain at s3040 first starts to increase. The top of the transition zone is at approximately the bottom of the sensing interval for s4050 when the strain at that sensor starts to increase at approximately t = 700 s (Figure 33). Interestingly, the strain at s5060 becomes slightly negative during injection and it starts to increase when the top of the transition zone reaches 50 cm height at approximately t =1,100 s.

Each strain curve flattens when it reaches 10 to 15 με, and the time when this occurs is approximately equal to the time when the PZP arrives at the top reflector in the strain sensing pair. For example, the slope of the signal from s2030 flattens at approximately t =800 s. and the PZP is at 30 cm at this time, and a similar effect occurs at s3040 (Figure 33).

Pump off

The pressures drop sharply when the pump is turned off as the water returns to hydrostatic conditions, and this is accompanied by slight drops in strain. After that, the strain increases slowly by several με during the period the pump is off.

Strain during draining

When the pump is reversed and turned back on, the strain initially becomes tensile in the lower sensors, but it reverses and becomes compressive with time. Data from the

lowest sensor, s1020, was erratic, however, the general trend occurs through despite the erratic data points. The largest tensile strain occurs in the lowest sensor, and it lasts the longest. The strain at s2030 increases by approximately 10 με and reaches a maximum at 2,850 s, approximately 600 s after the pump was turned on. A similar effect occurred at s3040, but the strain only increased by 8 με and the peak was reached after 350 s, and the effect was even smaller and briefer at s4050 (Figure 33). No tensile strain was observed at the upper sensor, which started to compress as soon as the pump was turned on (Figure 33 and 35). The peak compressive strain propagates from one sensor to another in approximately 250 s, giving a propagation rate of 0.04 cm/s.

After the initial tensile period is over, the strain decreases (becomes compressive) at a rate of 0.02 to 0.03 με/s at the lower three sensors (with the exception of s1020). The strain at s5060 during draining decreases at a slower rate (0.01 με/s) than at the sensors below it, just as the strain at that sensor increased at a slower rate during filling.

The strain decreases during draining and it drops below the original strain in all but s2030. When the pump is turned off at approximately t = 3,500 s, the strains rebound in all the sensors, increasing at a rate that is several times slower than the rate of decrease. Strains decrease again when the pump is turned back on at t = 4,500 s, and then increase again when it is turned off at t = 4,700 s. This pattern is repeated through another cycle of recovery from t = 4,700 to 5,300 s, and pumping from t = 5,300 to 5,400 s and subsequent recovery (Figure 33 and 35). Strain at the upper sensor, s5060, recovers to essentially the value at the beginning of the test. Strain in the other sensors are compressive, within 10 με of the starting strain, but the trends are increasing and they

may recover to within a few με with sufficient time. Strain at s2030 is 15 to 20 με more tensile at the end of the test than at the beginning (Figure 33 and 35).

Summary

The observations from the partial-fill test indicate

1. Pore pressure during injection and draining forms three zones: 1.) positive pressure; 2.) transition from positive to ambient; 3.) ambient pressure. The transition zone is bounded on the bottom by the point of zero pressure and on the top by ambient pressure. The height of the transition zone is approximately 12 cm, based on pressure data during filling. The transition zone moves upward at an average velocity of approximately 0.02 cm/s, which results in a pressurization rate of 2 Pa/s. The initial pressurization rate is faster than this, around 7 Pa/s at the upper two sensors, but it decreases with time.
2. The sand expands and experiences tensile strain when the pressure increases during imbibition, and it contracts with compressive strain during drainage. The occurrence of strain appears to be related to the location of the pressure transition zone. Changes in strain progress up the column at approximately the velocity of the water during injection. The strain is negligible or negative in the region above the transition zone, but it increases roughly linearly as the transition zone passes between the strain sensing region between the reflectors. The linear portion of the strain rate is 0.15 με/Pa.
3. The strain rate decreases and, in some cases, it changes sign when the pressure transition zone rises above the strain sensing interval.

4. There are several exceptions to the occurrence of tensile strain associated with increasing pressure. One of these occurs after the transition zone has moved past the strain sensors and the strain is either unchanged or decrease while the pressure continues to increase.

Another exception occurs when the pump is first shut off. The pressures drop due to the flattening of the negative vertical head gradient caused by the upward flow, and this generally causes strain to increase.

One more exception occurs as the head gradient increases later in the experiment. This occurs when the pump is first turned on to drain the column. This causes the pressures to drop abruptly, and this results in an abrupt increase in strain.

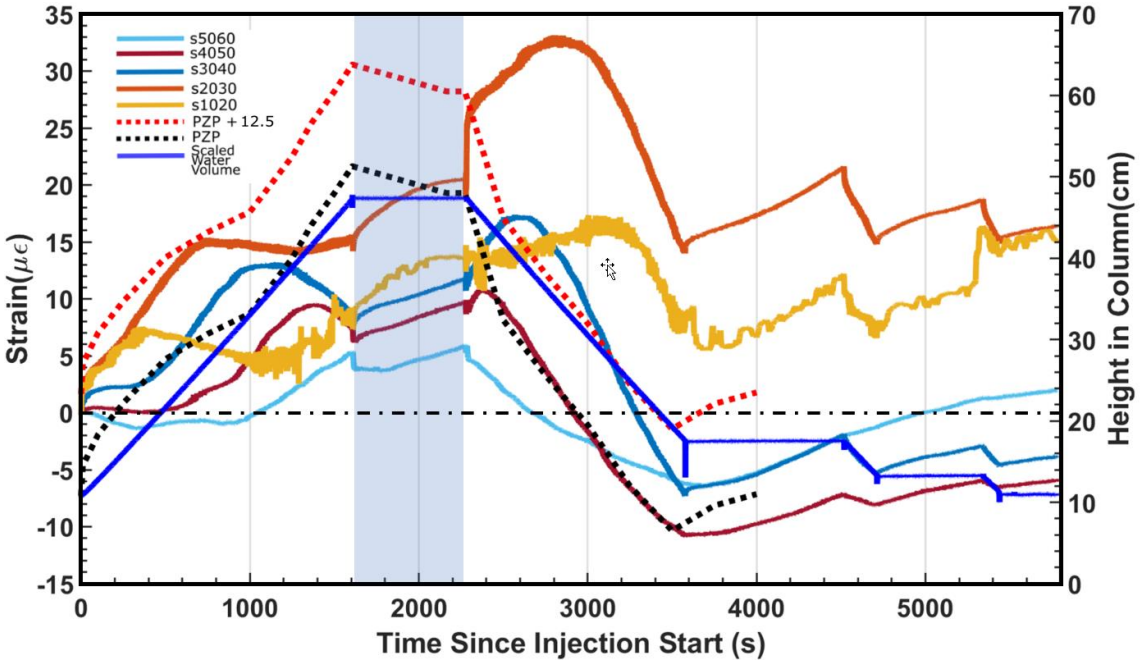

Figure 33: Strain, scaled water volume, and transition zone (PZP to PZP + 12.5 cm) height as functions of time for the infiltration fill-up test. Blue band is the period of no-flow.

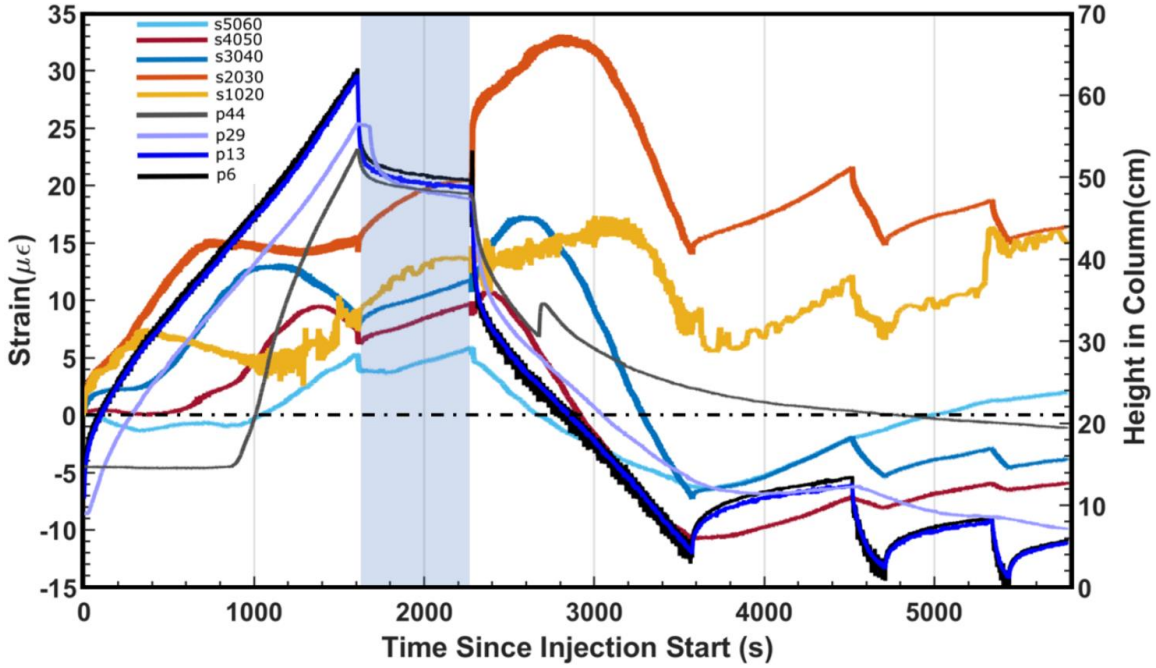

Figure 34: Strain and total head as functions of time for Partial-Fill test. Blue band is the period of no-flow.

Distributed Strain and Pressure in the Column

The strain and pressure at different sensors create a complex dataset that is difficult to fully appreciate when plotted together (e.g. Figure 33 and Figure 34). As a result, subsets of the data from similar height intervals along the column are described separately to identify relevant details.

10-20cm

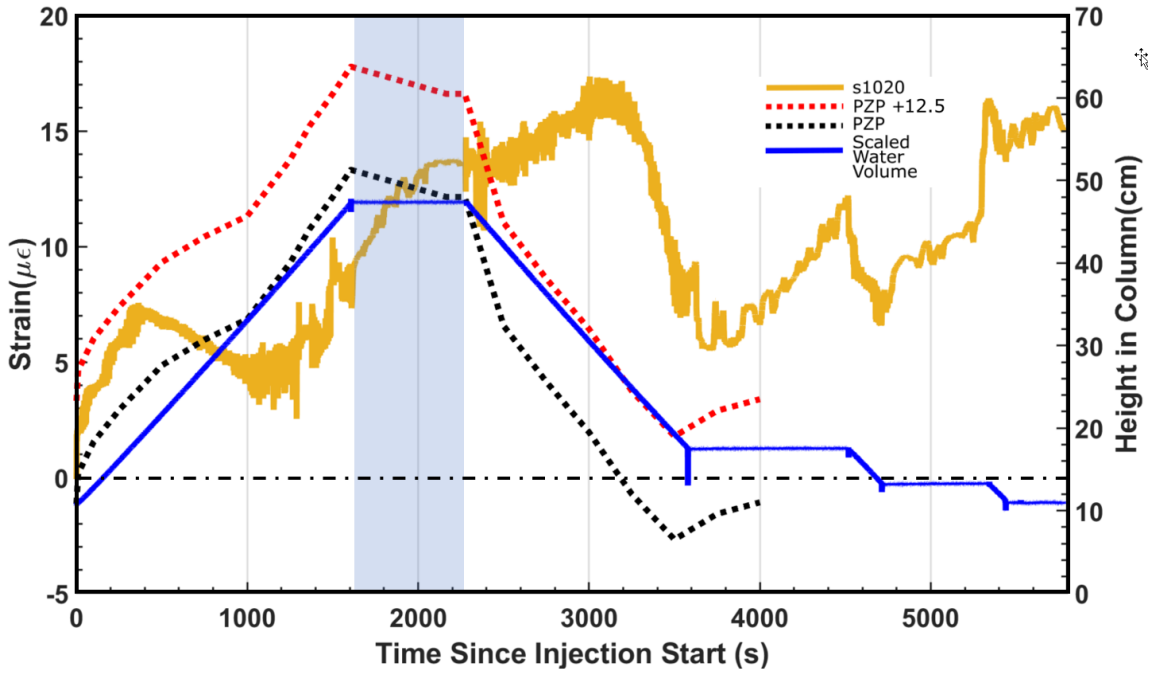

Figure 35: Strain at s1020, scaled water volume, and transition zone (PZP to PZP + 12.5 cm) height as functions of time for the Partial-Fill test. Blue band is the period of no-flow.

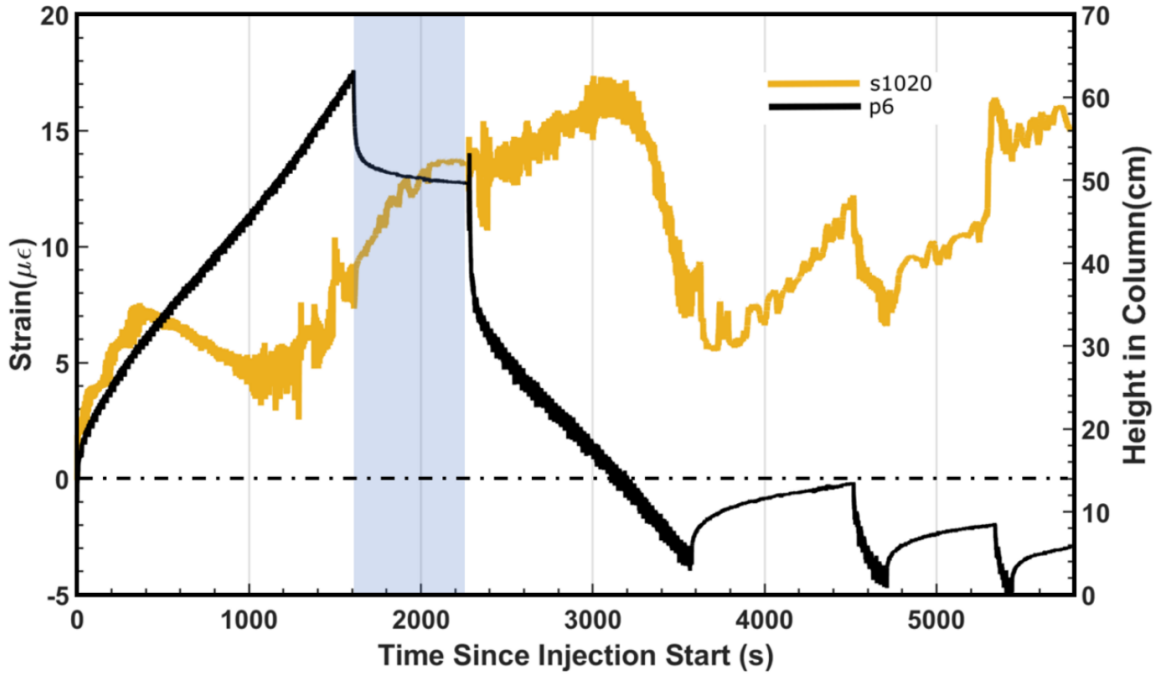

Figure 36: Strain at s1020 and total head at p6 as functions of time for Partial-Fill test. Blue band is the period of no-flow.

The s1020 sensor is the lowest in the column and the bottom reflector is slightly (5 cm) above the gravel, the p6 pressure sensor is below the s1020 interval in the gravel.

The data at s1020 includes high frequency fluctuations of variable amplitude (up to several με/s) and abrupt jumps (up to 5 με/s) that complicated the signal compared to the data from the other sensors (Figure 35 and Figure 36). The heads measured at p6 includes a regular periodic fluctuation with an amplitude of up to 4 cm and a period of 2 seconds. This period corresponds to the rotation rate of the pump and the periodicity is due a result of pulsation caused by the peristaltic pump. Some of the variation in strain in s1020 may also be caused by the pump. Abrupt offsets in the data from s1020 were corrected manually.

This region is tensioned initially by 2 με when the pump is turned on. This initial shock lasts for 1 seconds. After this period, the strain increases in a linear fashion of 0.2 με/s. This abruptly stops at t =350 s and the region is gradually compressed by 2 με. This continues until the pump is turned off.

The strain is more erratic data during drainage (Figure 33 and Figure 34). These jumps downwards are assumed to be artifacts and are ignored for this graphical analysis. Upon drainage, the strain gradually tensions to a value of 17 με 900 seconds after drainage begins (t = 3,100 s). After this tension peak, the region compresses at a rate of 0.02 με/s until the pump is turned off. Tensioning occurs when the pump is turned off as the saturation increases from delayed yield from storage.

20-30cm

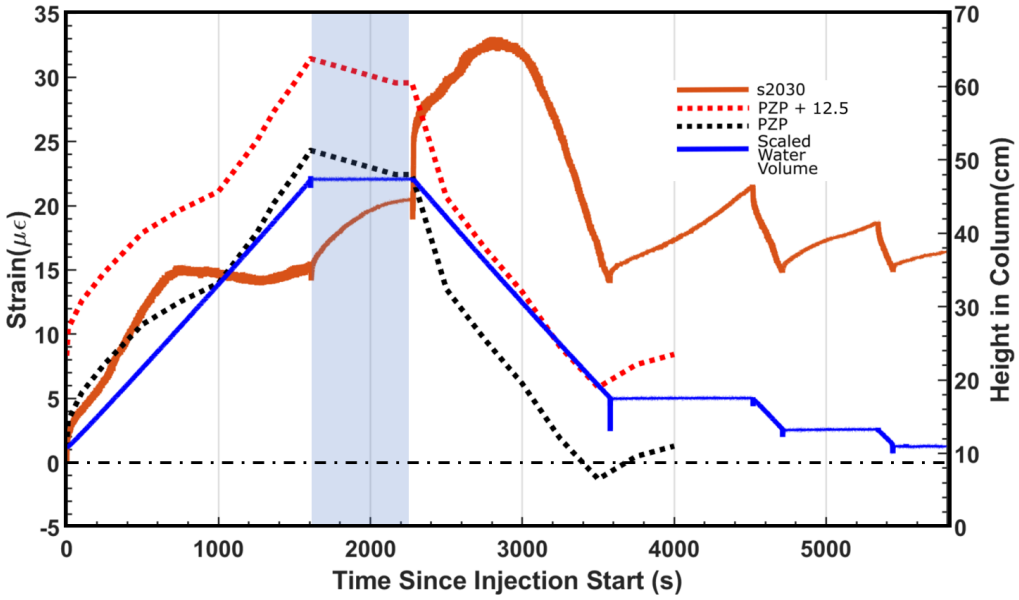

Figure 37: Strain at s2030, scaled water volume, and transition zone (PZP to PZP + 12.5 cm) height as functions of time for Partial-Fill test. Blue band is first the period of no-flow.

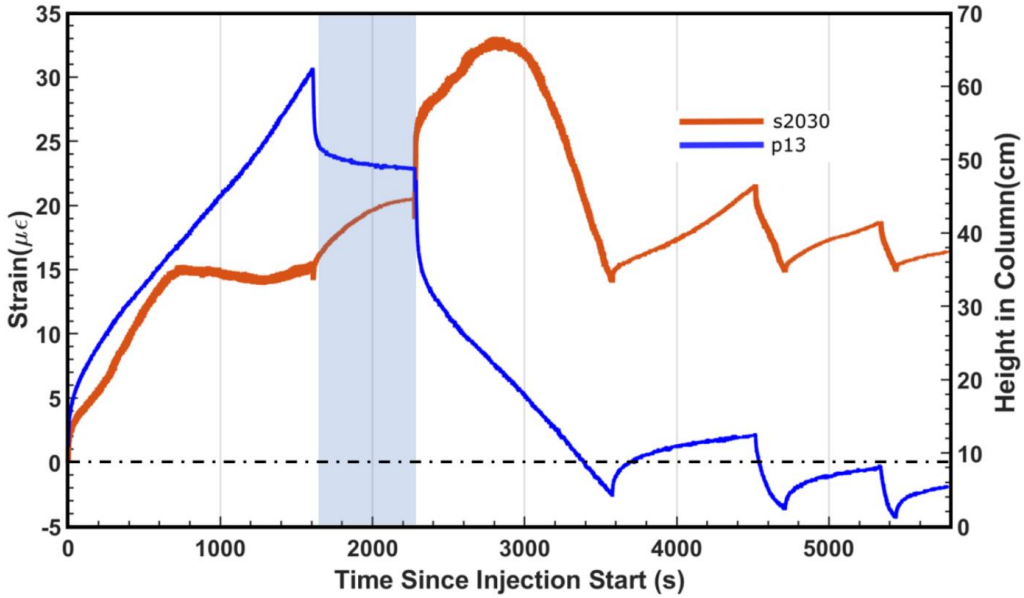

Figure 38: Strain at s2030 and total head at p13 as functions of time for Partial-Fill test. Blue band is the period of no-flow.

The region between 20 and 30 cm is initially tensioned by 1.5 με when the pump is turned on (Figure 37 and Figure 38). The strain increases at a rate of 0.2 με/s from time 50 to 700 s. Then the region begins slowly compressing at a rate of 0.007 με/s. Slight tensioning occurs around 1,300s.

When the pump is turned on in reverse, the strain tensions sharply by 5 με at the start of drainage. After this, the strain increases at a rate of 0.02 με/s and reaches a maximum net of 15 με 600 seconds after drainage began (t = 2,600 s). The region is linearly compressed at a rate of 0.035 με/s until the pump is again turned off (t = 3,600 s).

Tension occurs when the pump is off and water continues to drain from upper regions of the column. Tensioning is immediate after the pump is turned off and jumps to a steady rate of 0.0057 με/s. Turning the pump back on to pump out remaining water causes compression at a rate of 0.034 με/s.

30-40cm

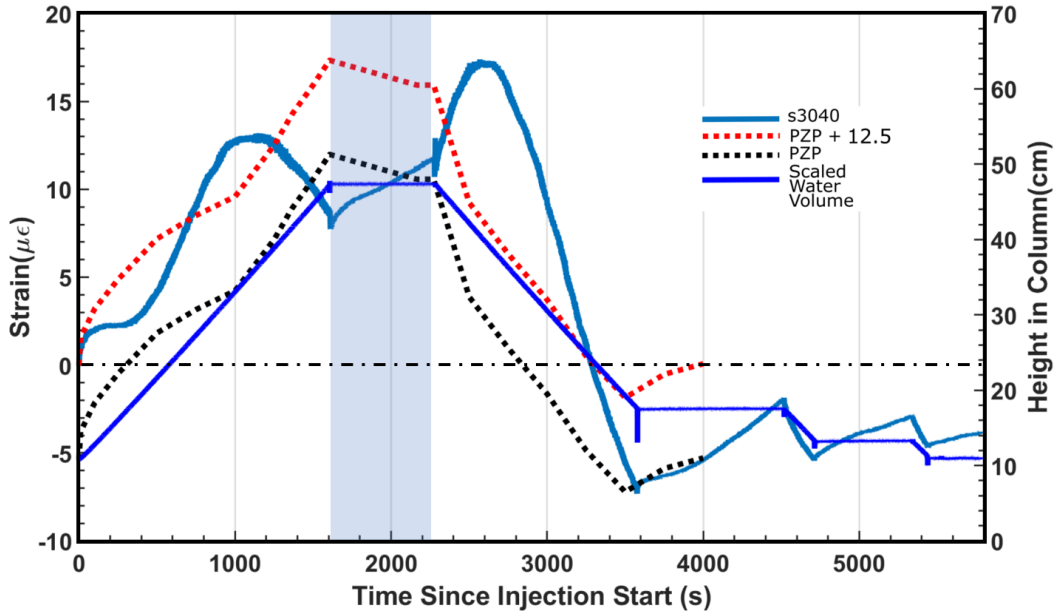

Figure 39: Strain at s3040, scaled water volume, and transition zone (PZP to PZP + 12.5 cm) height as functions of time for Partial-Fill test. Blue band is the period of no-flow.

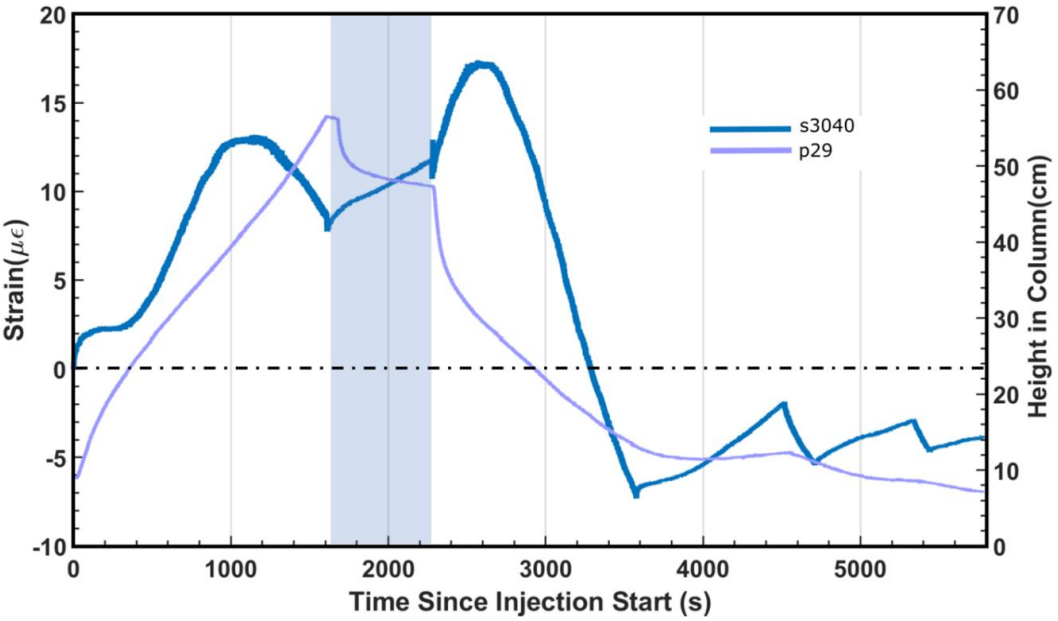

Figure 40: Strain at s3040 and total head at p29 as functions of time for Partial-Fill test. Blue band is the period of no-flow.

The region between 30 and 40 cm experiences a small increase of strain (0.5 με) from the pump being turned on (Figure 39 and Figure 40). The strain stabilizes with slight tensioning until time 330 s when it begins increasing linearly at a rate of 0.2 με/s. This stops at 1,000 s. The tension rounds out into compression and then decreases linearly at a rate of 0.011 με/s until the pump is turned off.

Tensioning occurs during drainage at a rate of 0.03 με/s rounding off to a maximum tension of 6 με greater than before drainage at a time of 300 seconds after drainage (t = 2,700 s). After rounding off, the strain compresses linearly at a rate of 0.029 με/s until the pump is shut off.

Immediate tensioning occurs when the pump is shut off. This is similar to the underlying sensor, but the magnitude is less than in the lower regions. This starts as a jump moving to a tensioning rate of roughly 0.0054 με/s. Compression at a rate of 0.018 με/s occurs when the pump is turned on again to remove the remaining water.

40-50cm

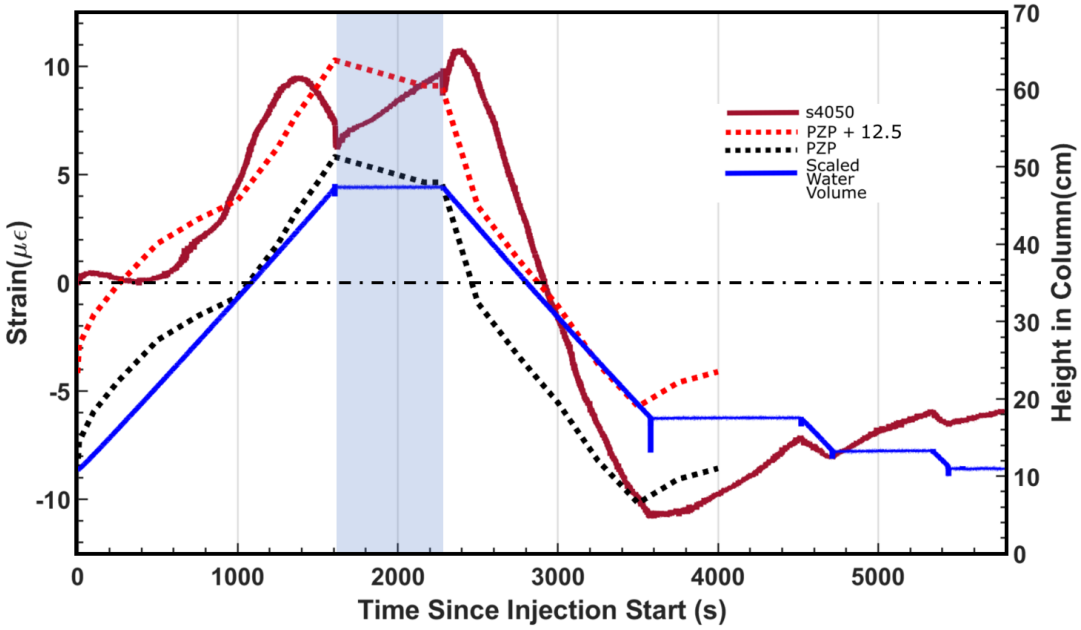

Figure 41: Strain at s4050, scaled water volume, and transition zone (PZP to PZP + 12.5 cm) height as functions of time for Partial-Fill test. Blue band is the period of no-flow.

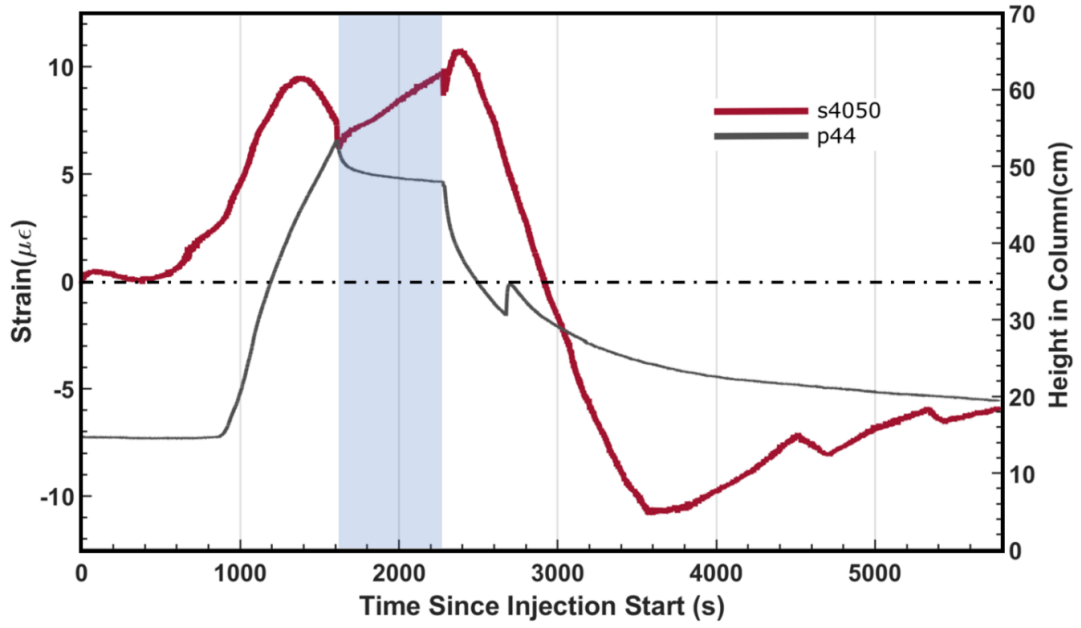

Figure 42: Strain at s4050 and total head at p44 as functions of time for Partial-Fill test. Blue band is the period of no-flow.

Strain remains stable in the 40 to 50 cm region, compressing slightly, after the pump is turned on (Figure 41 and Figure 42). Tension begins at t = 500 s and begins to linearly increase at a rate of 0.02 με/s. This tensioning reaches a maximum at time 1,500 seconds and decreases until the pump is turned off.

The pressure is constant until t = 900 s, and then it increases sharply. The increase in pressure occurs 350 s after the increase in strain. This occurs because the pressure sensor is 4 cm above the lower reflector in the strain sensor. The leading edge of the pressure transition zone is at an elevation of 40 cm at *t* = 500 s and it is at 44 cm at *t* = 900 s (Figure 42).

Slight tensioning occurs during drainage up to a value of 1 με 90 seconds after drainage starts (*t* = 2,400 s). After this, the region is compressed at a rate of approximately 0.02 με/s until the pump is again turned off. Around *t* = 3,200 seconds, the rate of compression slows.

Turning the pump off at *t* = 3,600 s ceases compression. Compression occurs at a rate of 0.004 με/s when the pump is turned back on.

50-60cm

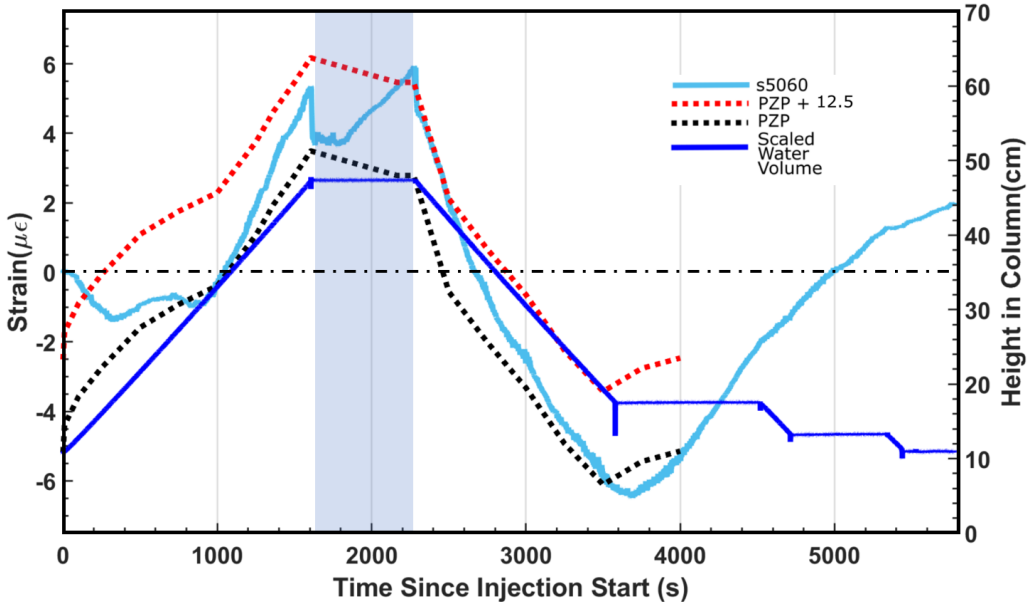

Figure 43: Strain at s5060, scaled water volume, and transition zone (PZP to PZP + 12.5 cm) height as functions of time for Partial-Fill test. Blue band is the period of no-flow.

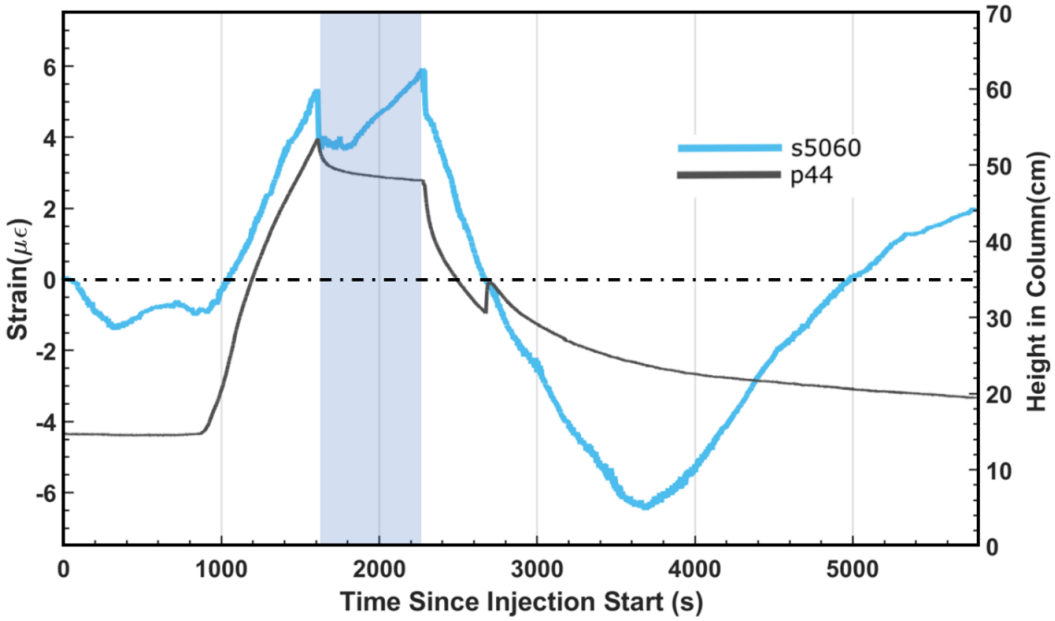

Figure 44: Strain at s5060 and total head at p44 as functions of time for Partial-Fill test. Blue band is the period of no-flow.

Compression occurs during the first part of this experiment reaching a value of 3 με. At t = 1000 s, tensioning occurs and linearly increases at a rate of 0.02 με/s. Turning the pump off causes s slight compression of 1.3 με.

Instant compression of 1 με occurs when the pump is turned on to drain the column. After this, the strain decreases at a rate of roughly 1.2 με/s.

Compression slows when the pump is turned off. This compression stops and tensioning begins 90 seconds after the pump is turned off. This tensioning has a rate of roughly 0.0065 με/s. The tension rate slows when the pump is turned back on.

COMPLETE-FILL TESTS: FILL AND DRAIN WITH PONDING

A series of tests was conducted by completely filling the column until water accumulated at the surface and then draining it by pumping or gravity.

The tests were conducted by injecting until water reached depths of around 1 cm at the surface of the sand, which will be referred to as “ponding”. The pump was turned off and injection stopped after ponding occurred. No water flows in or out of the column when the pump is turned off. This period of no flow continues for five to ten minutes. After this the column is either drained using the pump by gravity. The outflow tubing from the column is monitored for air entry, and the pump is turned off when air enters the outflow tubing. Sometimes the pump is turned back on after the total head rises above the injection port. Gravity drainage tests are typically allowed to drain for several hours. Most of the drainage occurs shortly after the drain is opened. The water that accumulates during drainage is measured as a function of time using a load cell.

Results

The pore pressure increases during injection, is nearly constant during the no-flow period when the pump is turned off and decreases during drainage. The axial strain becomes tensile as the pore pressure increases during injection, and this trend is reversed with compressive strains occurring when the pore pressure decreases during draining. These effects are expected and are similar to the partial-fill test, but details of the pore pressure and strain response vary among the different sensors and unexpected effects occur during ponding.

Many of the basic aspects of the tests with ponding are similar to the partial-fill test. These similarities will be noted in some cases, but in other cases the details of the complete-fill test will be repeated even though they are similar to those described earlier. This was done to put clarity before brevity.

Pore Pressure

The pore pressure data during the complete-fill test on October 19, 2019 (referred to as the 10/16 test) will be described below. The data from this test are used because all the sensors were working, the temperature change is small, and the data are representative of the other injection tests. The gravity drainage description is taken from a test on October 25, 2019 (referred to as the 10/25 test), and it is generally typical of the other gravity drainage tests.

Pore pressure was measured using tensiometers that were connected to transducers at a common datum below the bottom of the column. As a result, the pressure measured at the transducers was proportional to the total head. The pore pressure head at the tensiometers was determined by subtracting the elevation head from the measurements made by the transducers. The transducer locations were determined by measuring up from the bottom of the column, and this measurement is embedded in the name of the transducer. The bottom of the column was 0.5 cm above the transducers, so the elevation head used to convert total head to pressure head used the transducer location plus 0.5 cm. This is the same approach used for the partial-fill test.

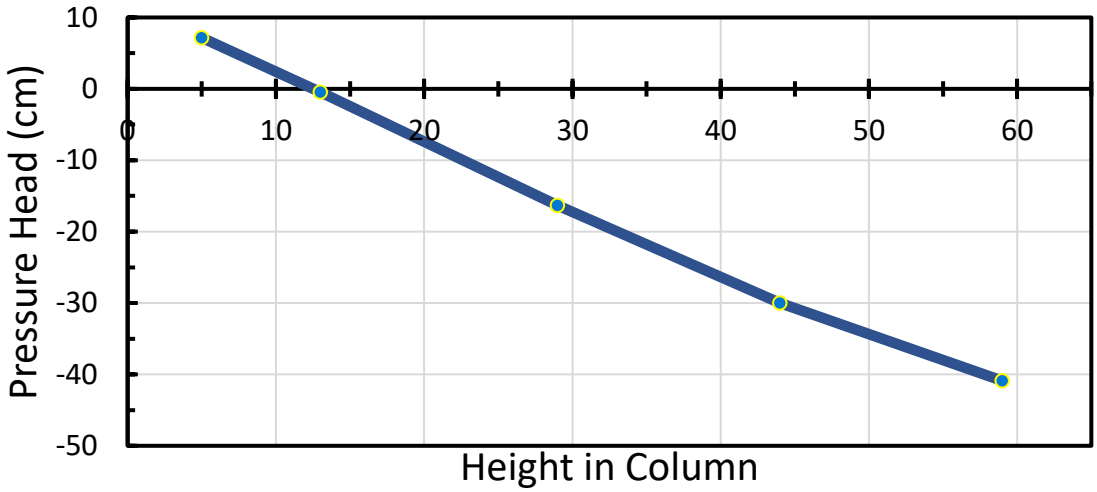

Figure 45: Pressure head profile before the 10/16 injection test.

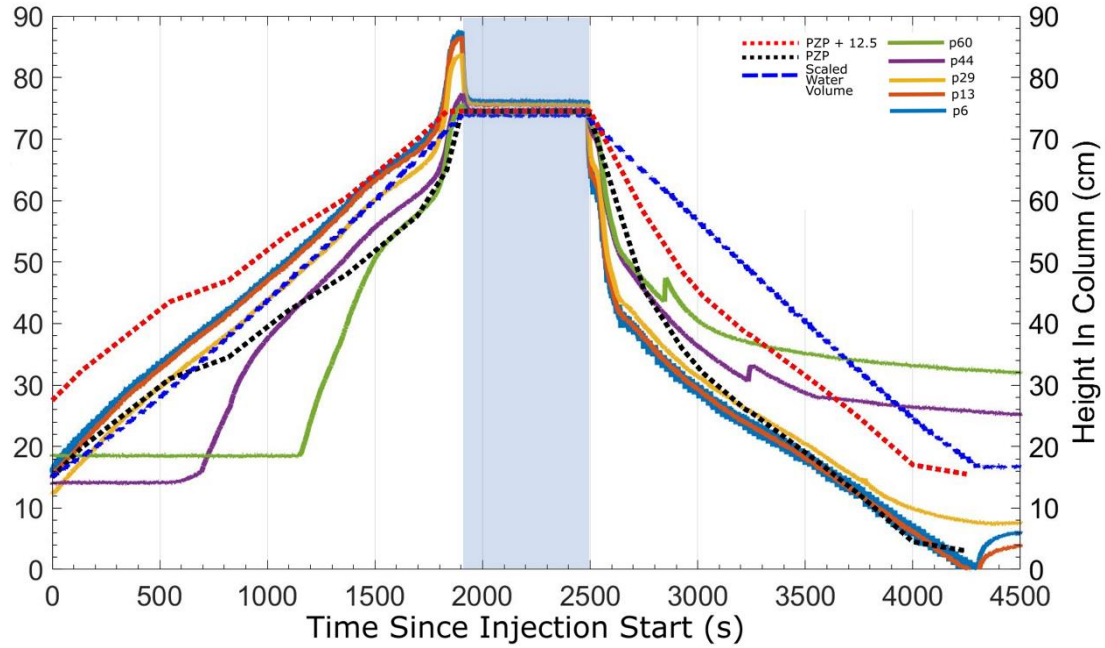

Figure 46: Total head, scaled water volume, leading edge, and point of zero pressure (PZP) as a function of time. Blue shaded regions are when the pump was off.

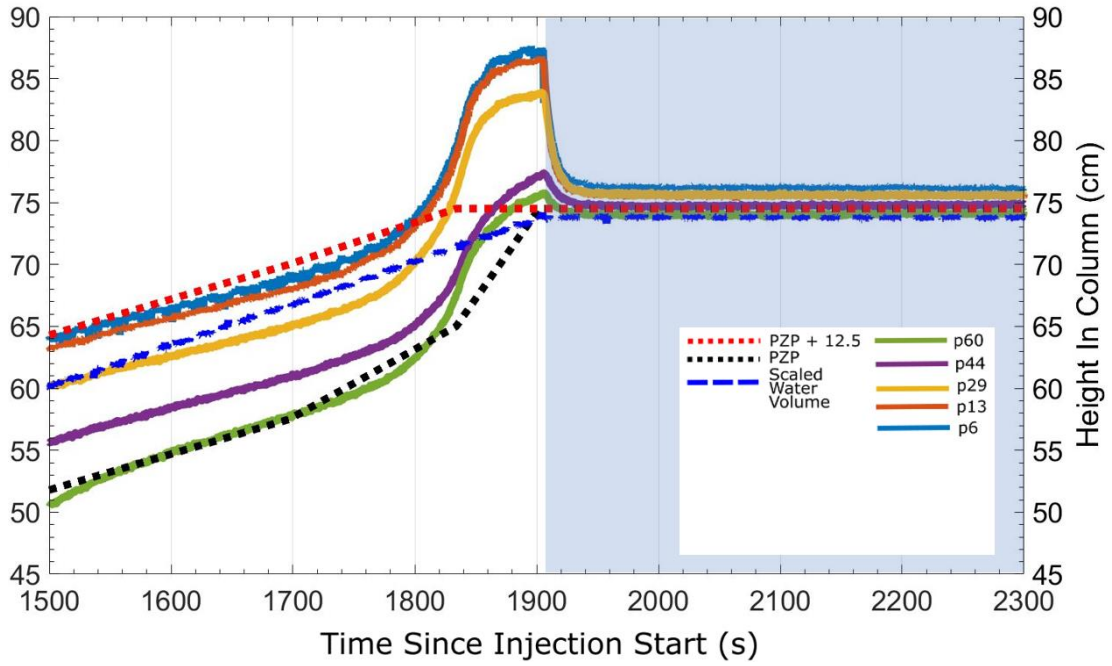

Figure 47: Detail of data series as a function of time. Detail is of the ponding event and no flow region.

Initial Conditions and Procedures

This suite of Complete Fill experiments included four tests conducted between October and November of 2019. The total head measured above the transducers at the beginning of the tests generally ranged between 10 and 15cm depending on the time since the last test. This means that the point of zero pressure started at an elevation of 10 to 15 cm. Slow drainage occurs for several days after a test, so the initial heads during tests conducted in this time period were higher than heads conducted after the heads have fully equilibrated.

Water was added to the top two tensiometers (p44 and p60) the beginning of each test. This was necessary because air entered these transducers between tests in some cases. The start of injection was delayed for tens of minutes after filling the transducers to

give the transducers time to equilibrate. Nevertheless, this time may have been insufficient for full equilibration to occur and may explain why the initial total heads in the upper tensiometers are higher than in the lower three transducers. The water content around p44 and p60 was likely increased by flow from the porous cup on the tensiometer. The conclusion is that the pore pressure was in equilibrium in most of the column, and it was slightly elevated in the upper part of the column because of filling of the tensiometers.

Pressure head data are available for five sensor locations during the 10-16 test. Data from the lower four transducers prior to injection (Figure 45) can be fit with a line with a slope of 1.0. The pressure heads at p44 and p60 are a few cm above the line with a slope of 1.0.

In the time series of the total head for the 10/16 test, the data measured at the horizontal bank of transducers start between 1,000 and 1,500 Pa, which is expected to be equilibrium conditions. Pressure in the lower three tensiometers (p6, p13, and p29) increases at roughly a constant rate of 3.4 Pa/second when the pump is turned on, while the pressure at the upper two transducers remains constant (Figure 46). The pressure at p44 starts to increase at 700 s and at p60 it increases at t =1150 s. The transducers are separated by 15 cm, so the pressure front is advancing at approximately 15 cm/450 s =0.03 cm/s. The pressure at p44 and p60 initially increases at approximately double the rate of the underlying transducers, approximately 7 Pa/s, and the rate drops to around 3.5 Pa/s after approximately 300 s. The rate of advance of the pressure front (0.03 cm/s) is consistent with the pressurization rate of 3.5 Pa/s. This indicates that the faster rate of

initial pressurization occurs while the transducer is sampling the transition zone. Assuming a rate of 0.03 cm/s and a duration of 300 s indicates the transition zone is approximately 9 cm long, which is consistent with other estimates (within a few cm).

The head gradient is steeper in the transition zone than in the underlying positive pressure zone. The steepest pressure head gradient in the transition zone is between 2 and 2.4 (e.g. times 545 and 1,094 in Figure 49).

The rate of pressure change increases sharply at approximately 1,750 s in p60, p44 and p29, and it starts to increase slightly later (at t = 1,750 s) in the deeper tensiometers, p13 and p6 (Figure 47). The pressure reaches a maximum rate of 30 Pa/s, approximately ten times faster than during most of the test. This rapid pressurization occurs when the top of the transition zone, as indicated by the PZP + 12.5 line, reaches the top of the sand at z = 72 cm (grey line in Figure 47) This rapid pressurization is brief, however, as the rate diminishes to 2 Pa/s in the upper three tensiometers, and it is several times greater than this in the lower two at t = 1,880 s when the PZP reaches the surface of the sand. The rates continue to diminish until the pump is turned off at 1,900 s.

The head reaches a maximum value of 87 cm at p6 when the pump is turned off. The heads drop abruptly when the pump is turned off and the sensors drop to 74 cm. This indicates that there is no flow during this time when the column is fully saturated and the pump is turned off.

The pressure head gradient is 1.0 when the column is fully saturated (Figure 49). During injection, the pressure head gradient is 1.2, an increase of 0.2 due to flow. The

flux is 5.4 x 10^{-5} m/s, so the hydraulic conductivity is 2.7 x 10^{-4} m/s, which is the same as during the partial-fill test, and essentially the same as measured during the falling head test (2.5 x 10^{-4} m/s; Figure 9)

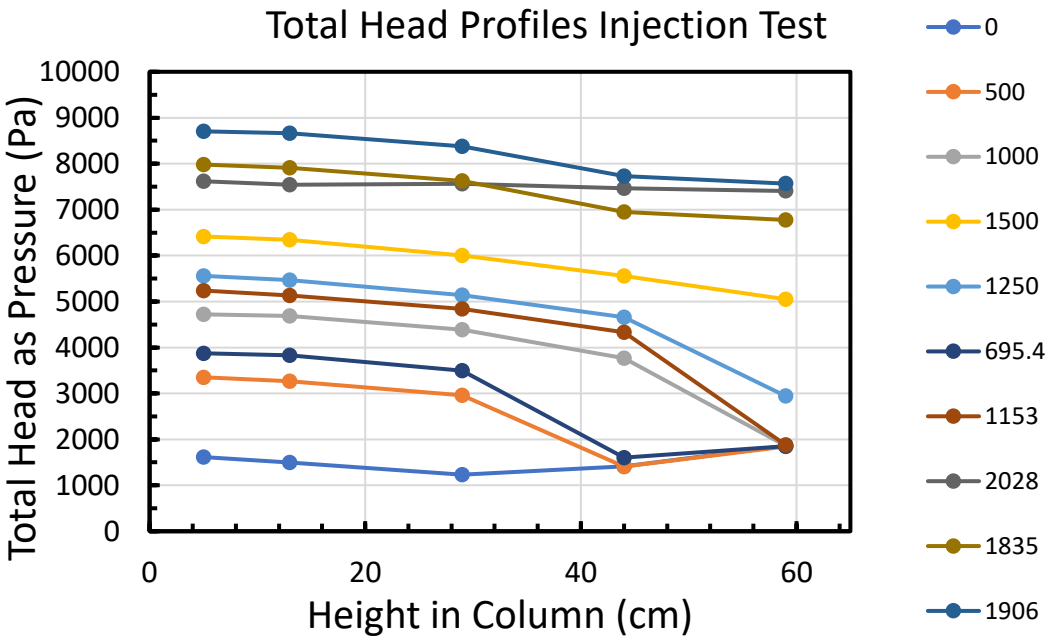

Figure 48: Total head profiles during the injection portion of the 10/16 test.

Wetting Front and Leading Edge

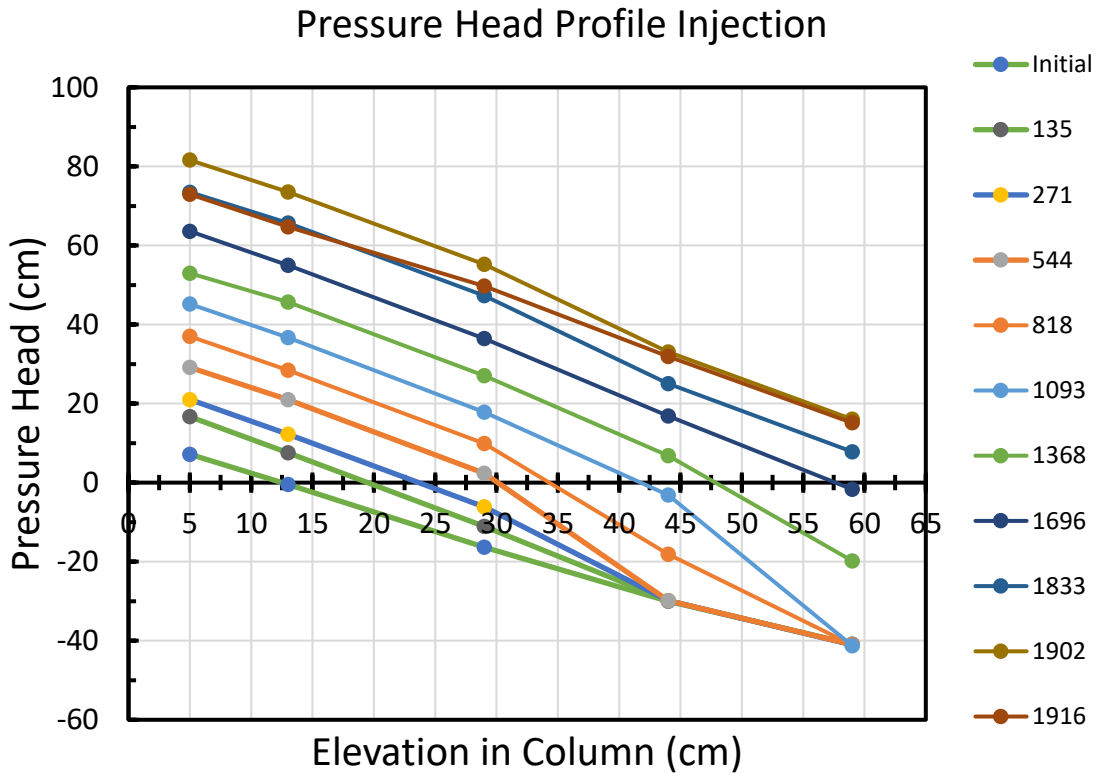

Figure 49: Pressure head profiles for injection test. Legend corresponds to seconds since injection started.

The partial-fill test described earlier resulted in data that indicates the pore pressure occurs in three zones: 1.) positive pressure, 2.) transition; 3.) ambient. The length of the transition region is estimated using the profiles of the pressure head during injection (Figure 49). The pressure head gradient is roughly uniform and equal unity in the bottom of the column and it varies slightly about unity in the overlying tensiometers before injection starts (Figure 48). A line with a slope of unity is shown in Figure 48 for reference. The point of zero pressure is at approximately 15 cm before the pump is turned on (Figure 49). The pressure head increases at the bottom three tensiometers, but it remains unchanged in the top two transducers when the pump is turned on. The

pressure head gradient steepens to at least 2 in the transition zone, and it flattens above this

This plot (Figure 49) shows regions where the pressure gradient changes with transducer height in the column. The rectangle drawn shows a region where the pressure gradient breaks from the gradient in the lower 3 transducers. The 44cm transducer records a pressure of slightly above initial equilibrium conditions at this time. It is inferred that the wetting front transition zone is just arriving at this transducer. From this, the transition zone length is estimated to be around 13cm.

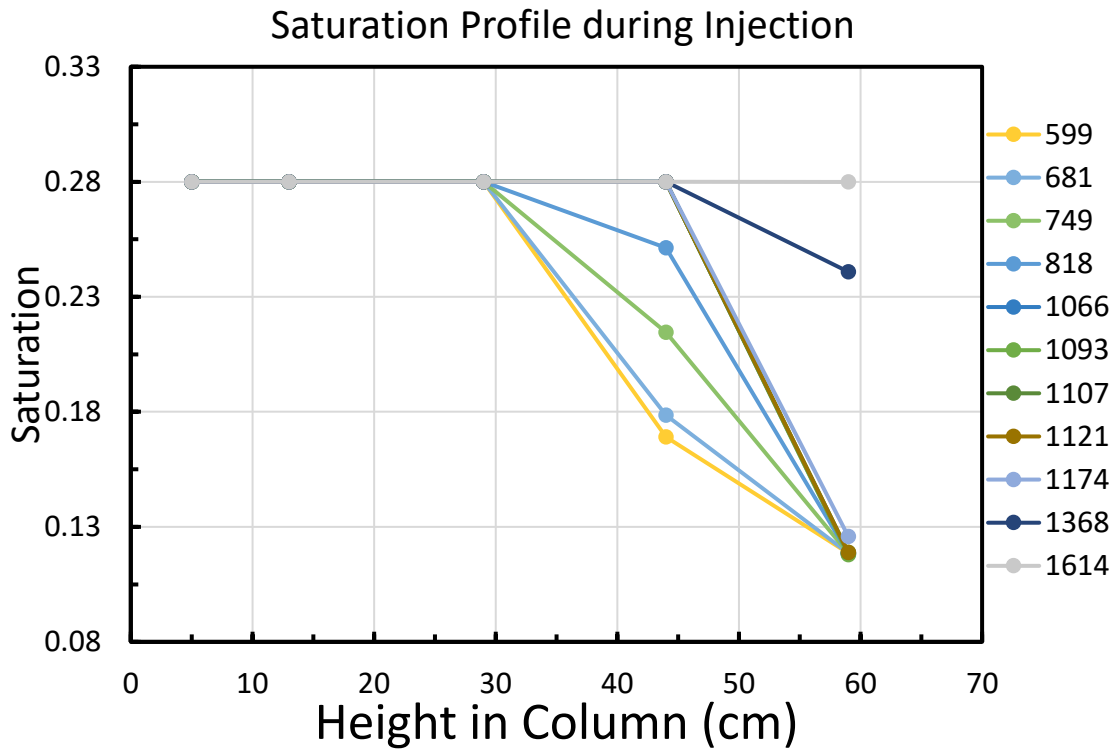

Figure 50: Saturation profiles during injection. a=0.039 cm^{-1} and n=4.3.

Water content profiles are created using the pressure head values along with the moisture retention data (Figure 50). Sand at the p5 and p13 sensor is fully

saturated from before the start of the test. The initial water content at p29 is slightly less than the saturated water content (0.28). The sand at p44 and p60 have initial suctions of 0.17 and 0.12 respectively. Suction pressure decreases as the wetting front moves up the column. The saturation increases to the porosity, 0.28. The saturation for a tensiometer can be found at a particular time using this method. Increasing saturation appears to occur at a tensiometer when the PZP is between 8 and 15 cm below that tensiometer.

Combining data from the pressure and saturation profiles during injection, the length of the transition zone is estimated to be 12.5 cm above the PZP.

Drainage by Pumping Out

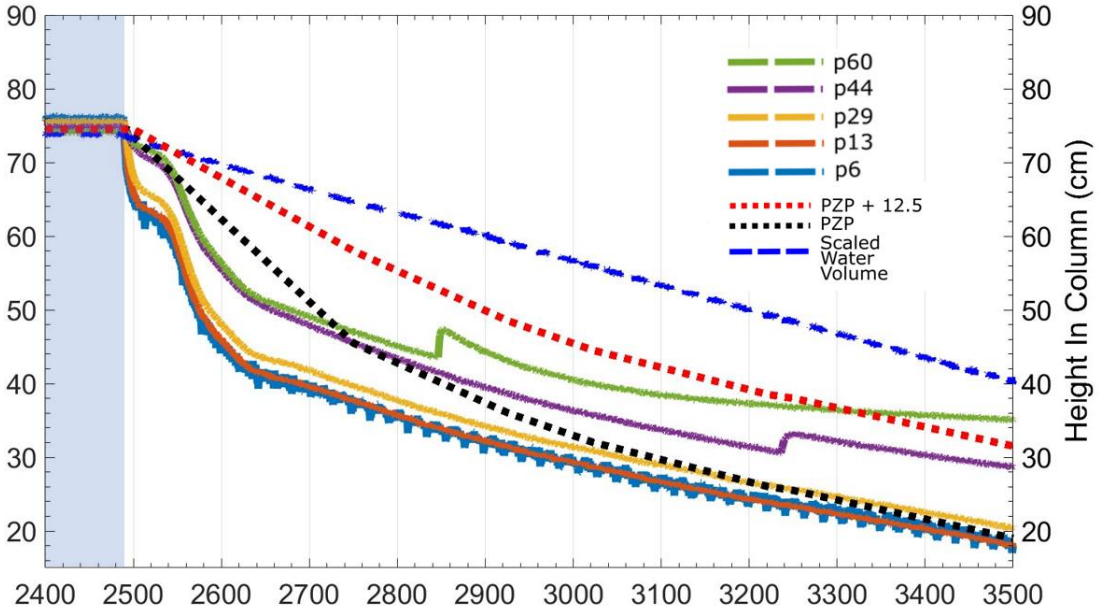

Figure 51: Total head, normalized water volume, point of zero pressure (PZP) and PZP +12.5 cm as functions of time during drainage of the 10-16 complete fill test. The pump was turned on at t =2480 s to drain water from the column. Water is ponded on the sand up to t =2540 s.

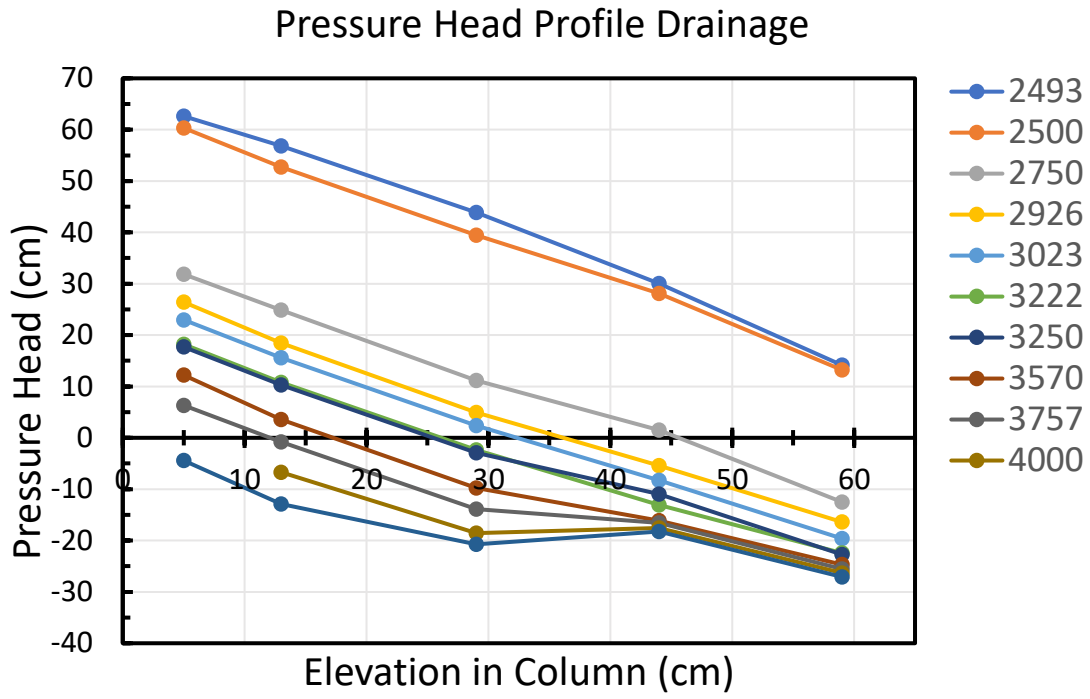

Figure 52: Pressure head profiles for the drainage portion of the injection test.

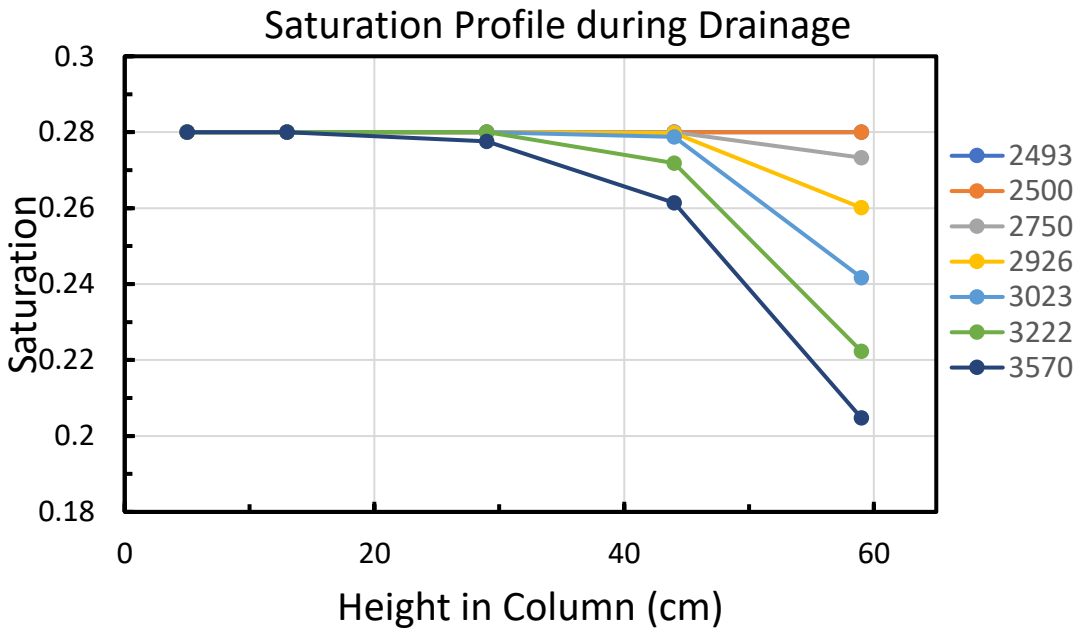

Figure 53: Saturation profile for the drainage portion of the injection test.

Drainage of the column by pumping out causes a sharp initial drop in pressure. The p6 transducer records a drop of 1,000 Pa (Figure 51). The drop slows for a brief period, presumably as the pond drains, and then sharply drops again. The pressure in the lower three transducers drops at a similar rate. The topmost sensor breaks from the trend first at around t = 2,630 s. After that the sensor second from the top breaks from the trend 930 seconds later. The upper two sensors jump in pressure during drainage events. These events are not completely understood but reliably happen in every test. The gradient of drainage by pumping out is 0.87 (Figure 52).

Pressures in the bottom three transducers rise when the pump is turned off. The rise is sharp at first and then slows. The upper two transducers do not respond to continued cycles of drainage.

Saturation in the column drops in the upper three transducers (p60, p44, p29). At time 3,570 s, p60 drops to a saturation of 0.21, p44 drops to a saturation of 0.26, and p29 drops to a saturation of 0.275. The lower two transducers do not drop appreciably below complete saturation (0.28) (Figure 53).

Gravity Drainage

Pressure drops more quickly during gravity drainage than during drainage by pumping out. The ponded water drains much more quickly, and the effects of its drainage are absent from the data. The pressure first drops in lower points of the column and the drop propagates upward. The pressure in p6 drops by 3,500pa in 5 seconds after the drain is opened (Figure 54 and Figure 55). This initial drop can be seen in the pressure head

profile of the gravity drainage (Figure 56). The total head at the p6 and p13 tensiometers drops by over 20 cm between the t = 3,185 and t = 3,187 second profiles while the total head at the p44 and p60 tensiometers stays nearly constant (Figure 56).

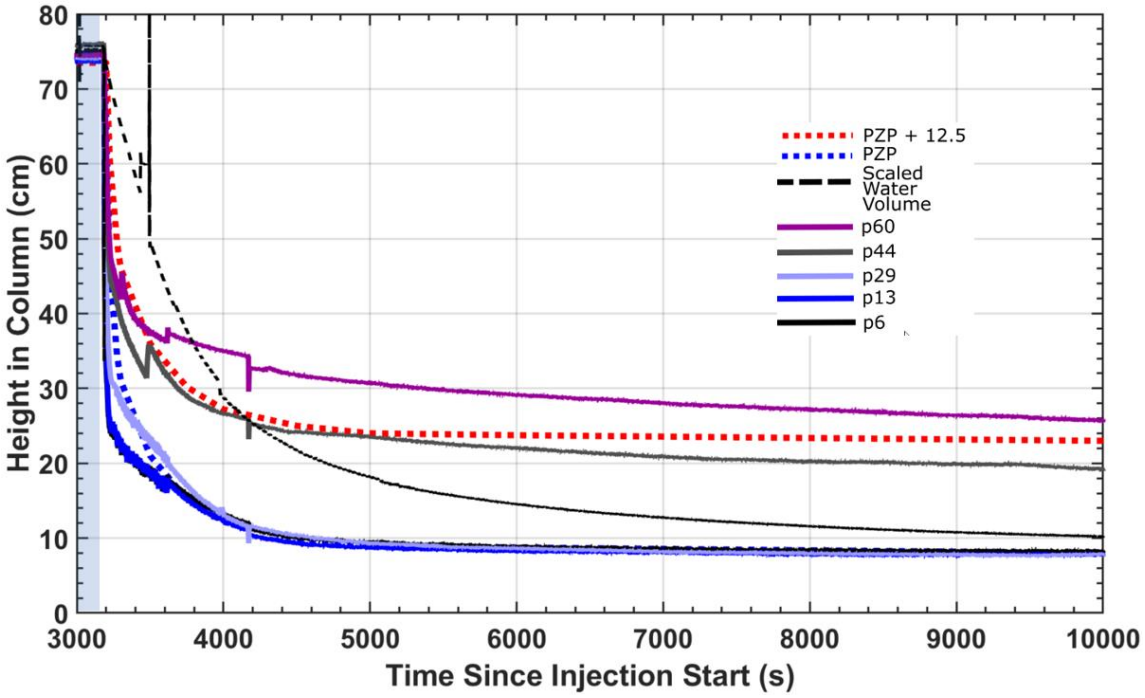

Figure 54: Total head, normalized water volume, point of zero pressure (PZP) and PZP +12.5 cm as functions of time during gravity drainage of the 10/25 complete fill test. The drain was opened at t = 3,185 s.

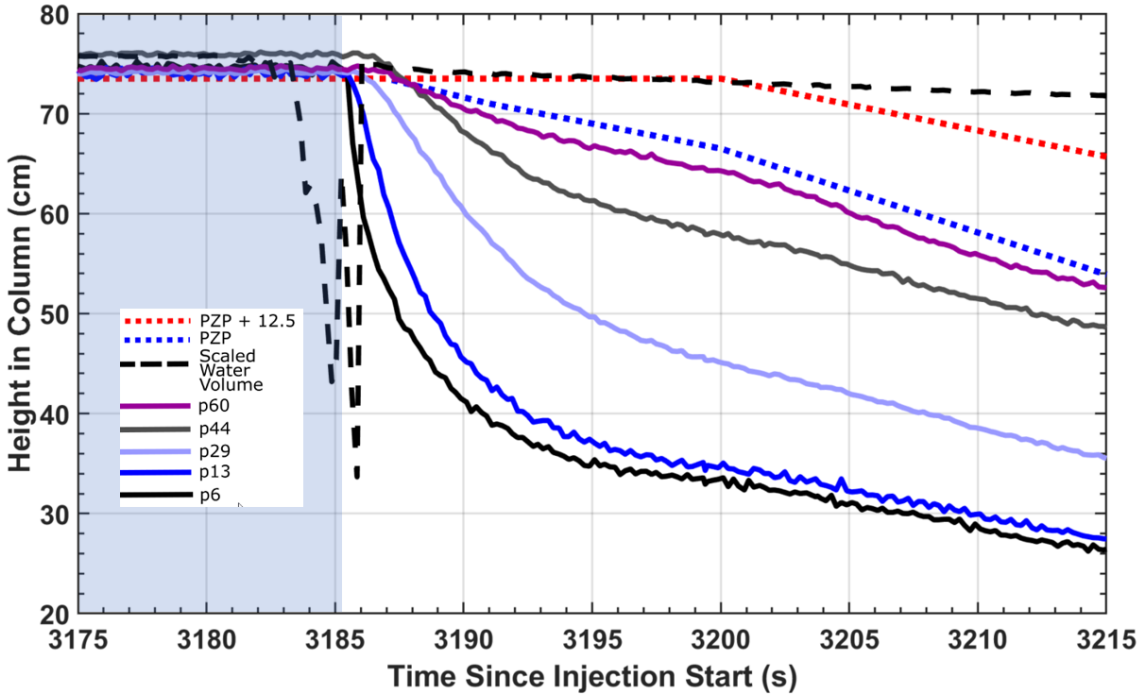

Figure 55: Total head, normalized water volume, point of zero pressure (PZP) and PZP +12.5 cm as functions of time during gravity drainage of the 10/25 complete fill test. Plot shows detail of the drain initially being opened at t = 3,185 s.

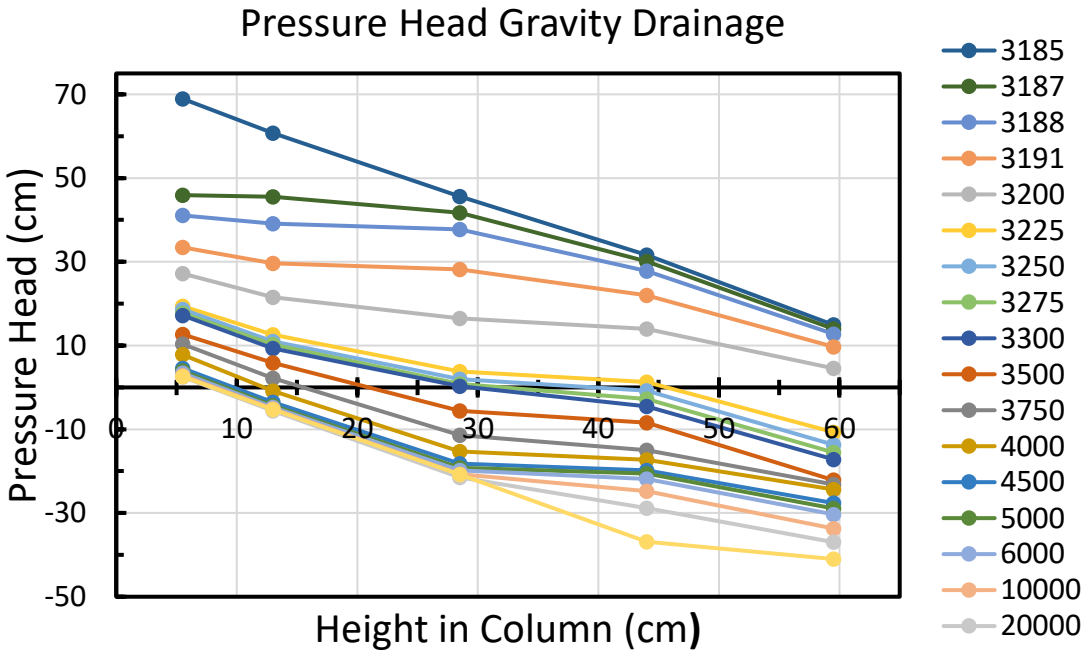

Figure 56: Pressure head during the gravity drainage of the 10/25 fill and drain test.

The total head changes little after 4,500 seconds in p6, p13, and p29. The total head at p44 and p60 continues to drop throughout the test (Figure 56).

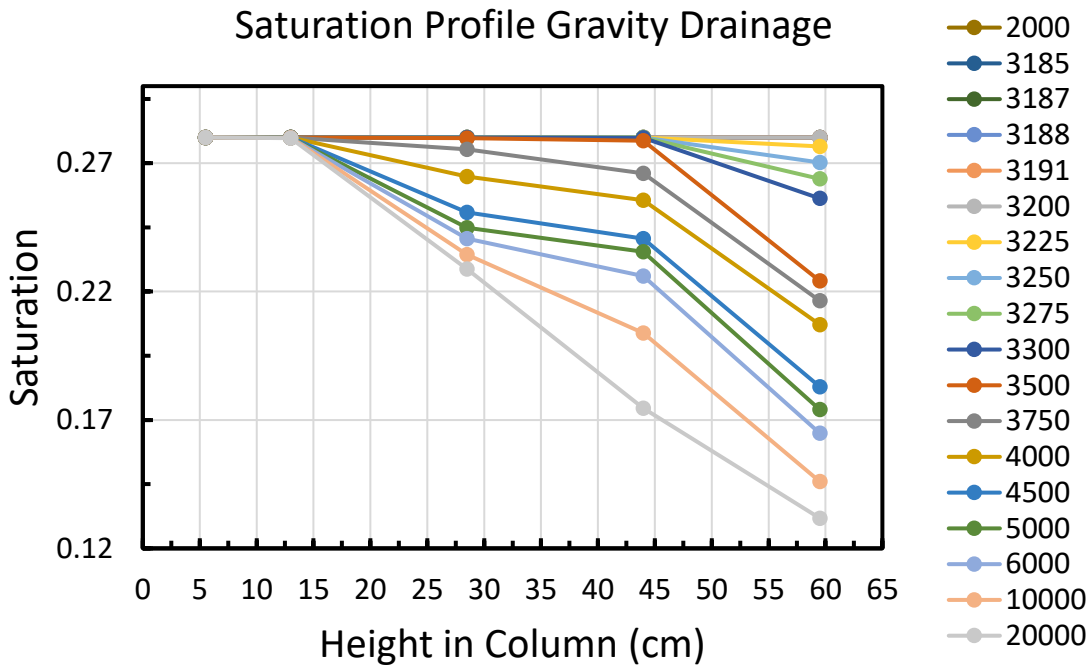

Figure 57: Saturation during the drainage portion of the 10/25 fill and drain test.

Saturation quickly drops in the sand at the p60 transducer (Figure 57). Saturation several hours after injection (t = 20,000 s) is similar to ambient saturation in the sand (Figure 15). The sand is saturated near the p6 and p13 transducers during the entirety of the test (Figure 57).

Strain

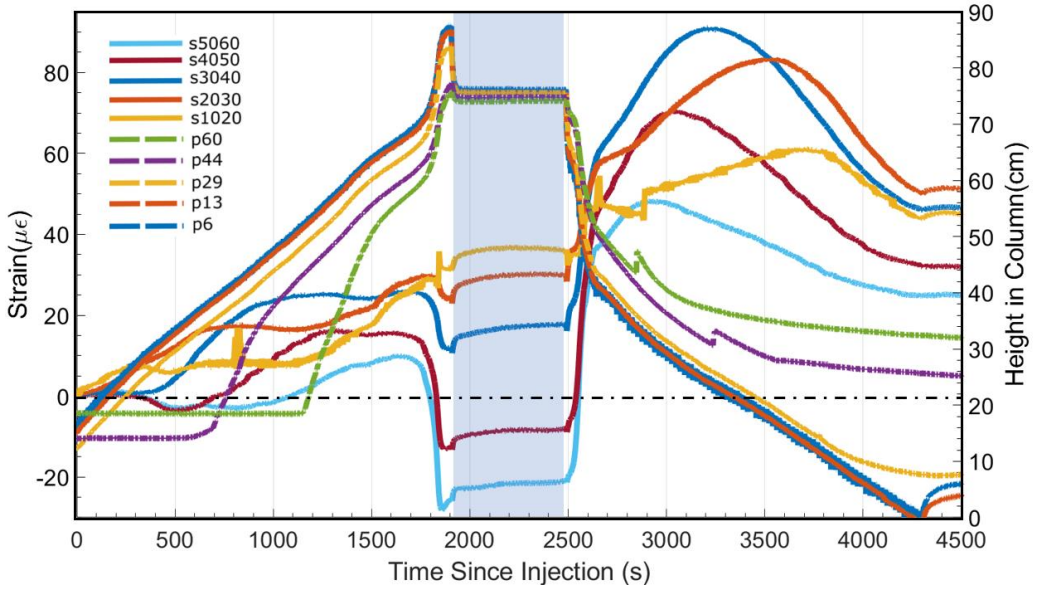

Figure 58: Strain and total head time series for the 10/16 fill and drain test. Blue band is the period of no-flow. Drainage by pumping out starts at t = 2,480 s.

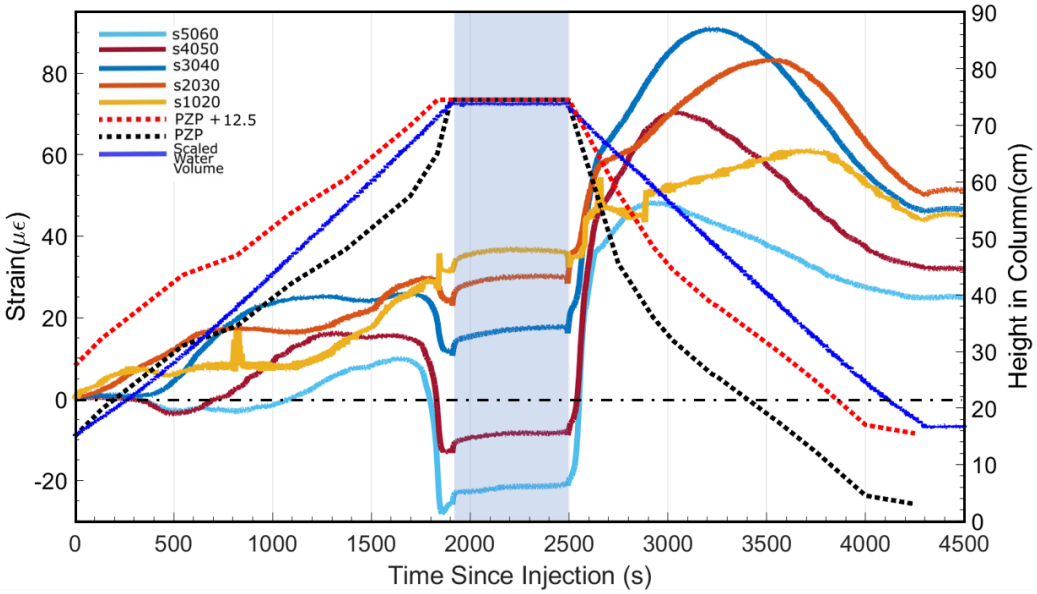

Figure 59: Strain, scaled water volume, and transition zone (PZP to PZP + 12.5 cm) height as functions of time for the 10/16 test. Blue band is the period of no-flow. Drainage by pumping out starts at t = 2,480 s.

Strain data was recorded between five pairs of reflectors between 10 and 60 cm above the datum. The PZP initially occurs between 7-15 cm due to residual saturation from previous tests. The top of the pressure transition zone is inferred to occur 20-25 cm above the datum at the start of pumping. The lowest pair of strain sensors, s1020 and s2030, lie within the transition zone at the start of the test. As pumping occurs, the transition zone moves up through the column encompassing all the sensors.

Strain During Filling

Strain occurs in the column during injection as the transition zone and PZP moves upwards through the column. Tensioning occurs when the transition zone reaches within +/- 5 cm of the bottom of the sensing region. The strain increases linearly during this period at a rate between 0.02 and 0.05 με/s. When the PZP reaches the top of the sensor (within +/-5 cm) strain rate lessens and either goes to zero or into slight compression.

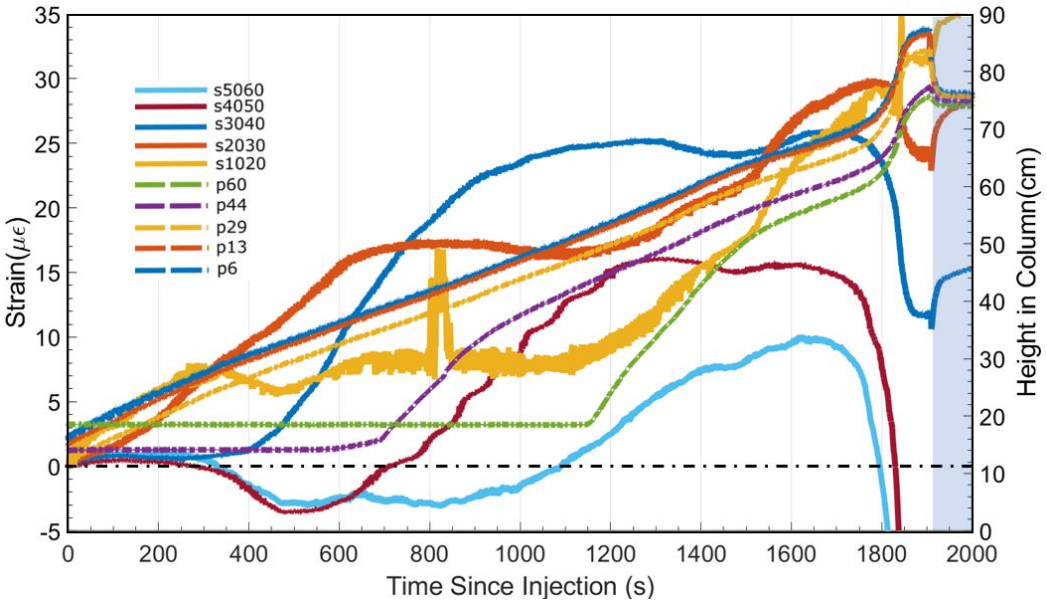

Figure 60: Strain and total head as functions of time for the 10/16 test. Blue band is the period of no-flow.

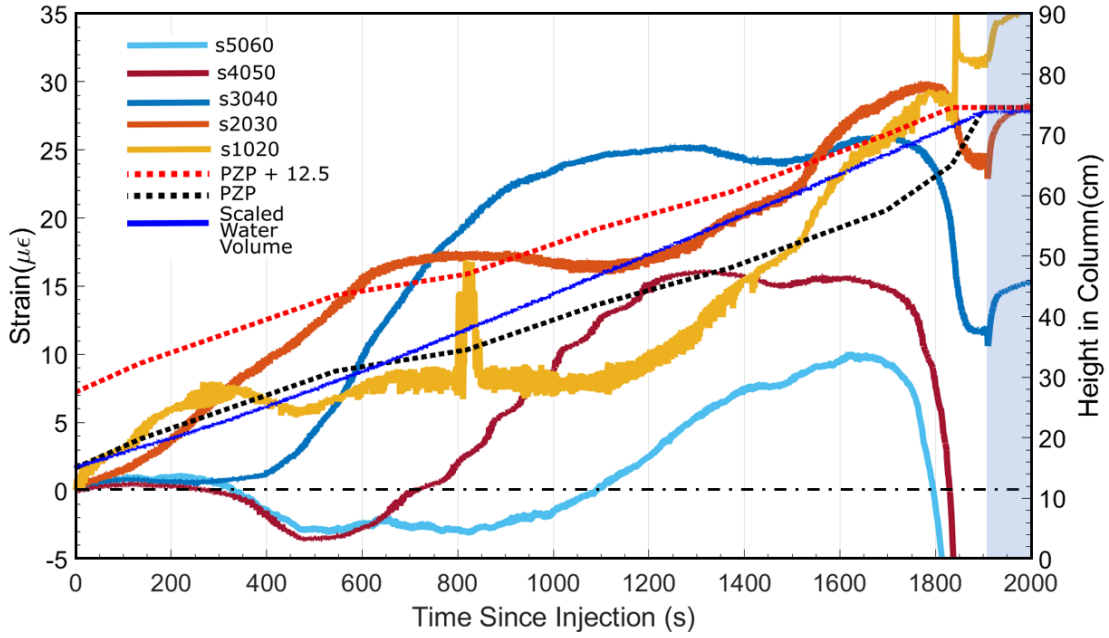

Figure 61: Strain, scaled water volume, and transition zone (PZP to PZP + 12.5 cm) height as functions of time for the injection portion of the 10/16 test. Blue band is the period of no-flow.

Strain early in the 10/16 test is similar to the Partial-Fill (Figure 26). Immediate tensile strain of between 1 and 3 με occurred when the pump was turned on at the lower three sensors with the highest tension in the lowest sensor (though this event is somewhat obscured by the line thickness). Essentially no strain occurs at the upper two strain sensing regions (s4050 and s5060). The strain at s2030, the second lowest sensor, increased at a rate of approximately 0.025 με/s for 600 s then leveled out and was roughly constant at 17 με over 600 s < t < 1200 s. The strain then increased a second time (1200s t < 1800s) at a rate similar to the first period of increase. This pattern of increasing, leveling out, and increasing again also occurred in the lowest sensor, s1020, but the signal is noisier than the one from s2030 and this reduces the confidence in the repeatability of the signal. The strain rate at s3040 was small initially, but then at t = 400

s it progressively increased to approximately 0.05 με/s and 600 s later the rate decreased to essentially zero (t = 1,000 s,). This resulted in a total of 25 με during test, which is the largest of any of the sensors. The strain started to increase roughly 600 s later (t = 1,600 s) but the strain was affected by interactions with the free surface, so it is unclear if the second period increasing strain that occurred at s1020 and s2030 would have also occurred at s3040.

The strain at the other two sensors, s4050 and s5060, was also constant at the start of the test, but it became compressive at roughly the same time the strain in the underlying s3040 became tensile. The strain decreased at a rate of -0.03 με/s, which is approximately half the rate of expansion at the underlying s3040 sensor. for approximately 100 s, resulting on 3 to 4 με of compression. This trend at s4050 reversed at approximately t = 600 s when the strain rate started to increase, reaching a rate of 0.035 με/s for a period that lasted 600 s and then flattening back to zero rate (at t = 1,200 s). PZP+12.5 at t = 600 s was at z = 44 cm, which is approximately at the bottom of the sensing interval, and the PZP at t = 1200 s was at z = 48 cm, which is approximate at the top of the sensing interval of s4050. These observations indicate that compression occurs in front of the leading edge of the transition zone, and it supports the findings from the partial fill test that a linear increase in strain occurs when the transition zone is within the sensing interval.

A similar effect occurs in the data from s5060 (Figures 61 and 62). Here the period of initial compression lasts until approximately t = 900 s, which is when PZP +

12.5 cm is at z = 50 cm, the bottom of the sensing interval. The strain rate then increases to 0.025 με/s, and the strain becomes affected by interaction with the free surface before this period ends.

Interactions with the free surface

The pressure and strain progress up the column as relatively uniform fronts, as outlined above, but these signals change sharply as the transition zone interacts with the free surface of the column. Four tests were conducted where the saturation increased upward and reached the free surface and the strain and pressure signals were generally similar. A video camera recorded the appearance of the free surface during wetting and ponding of a test on 10/27, so those data will be used to describe this response. The pressure and strain during all the tests where water ponded at the free surface resemble the results from the 10/27 test.

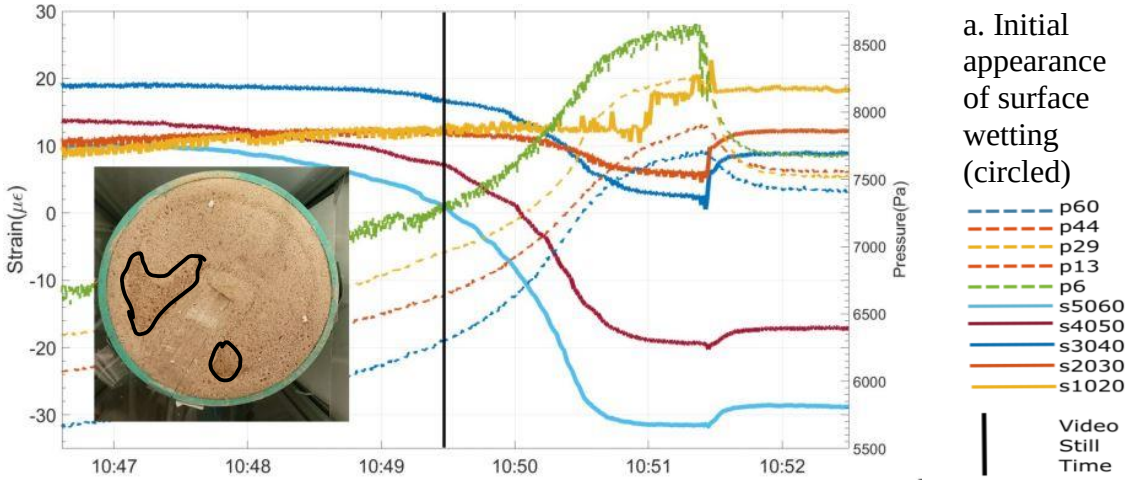

a. Initial appearance of surface wetting (circled)

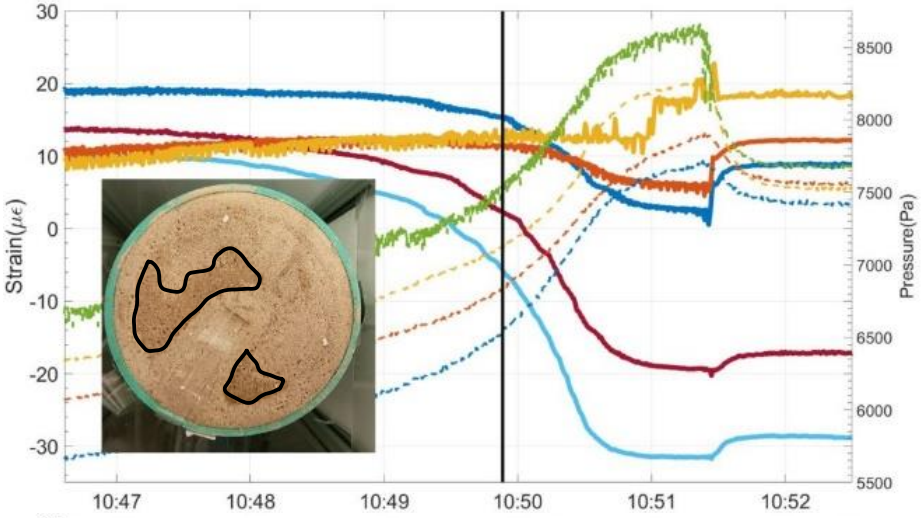

b. Continuation of surface wetting

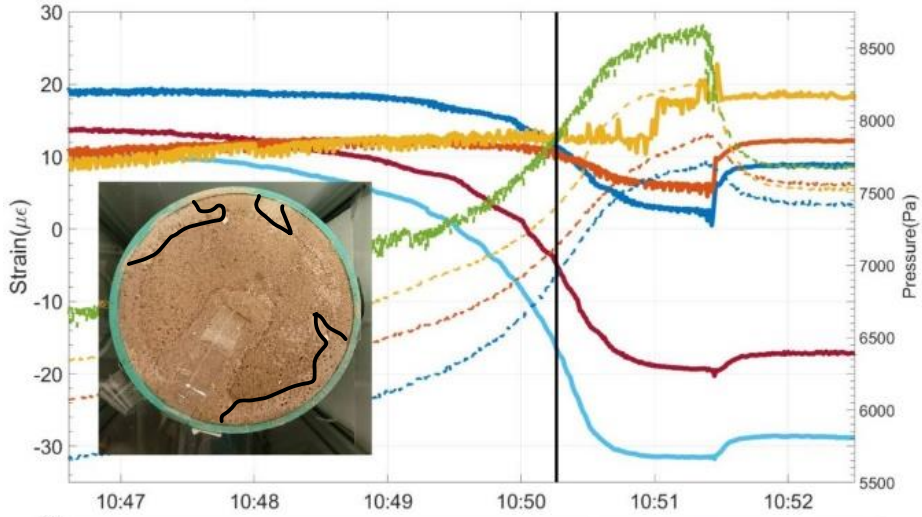

c. Continuation of surface wetting. Dry areas circled.

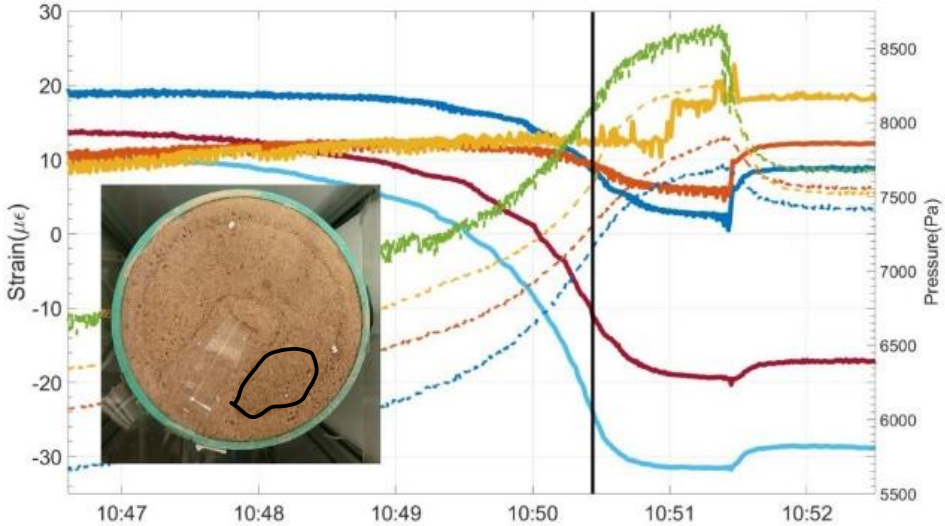

d. Appearance of surface saturation in lower regions of the surface. Saturation circled.

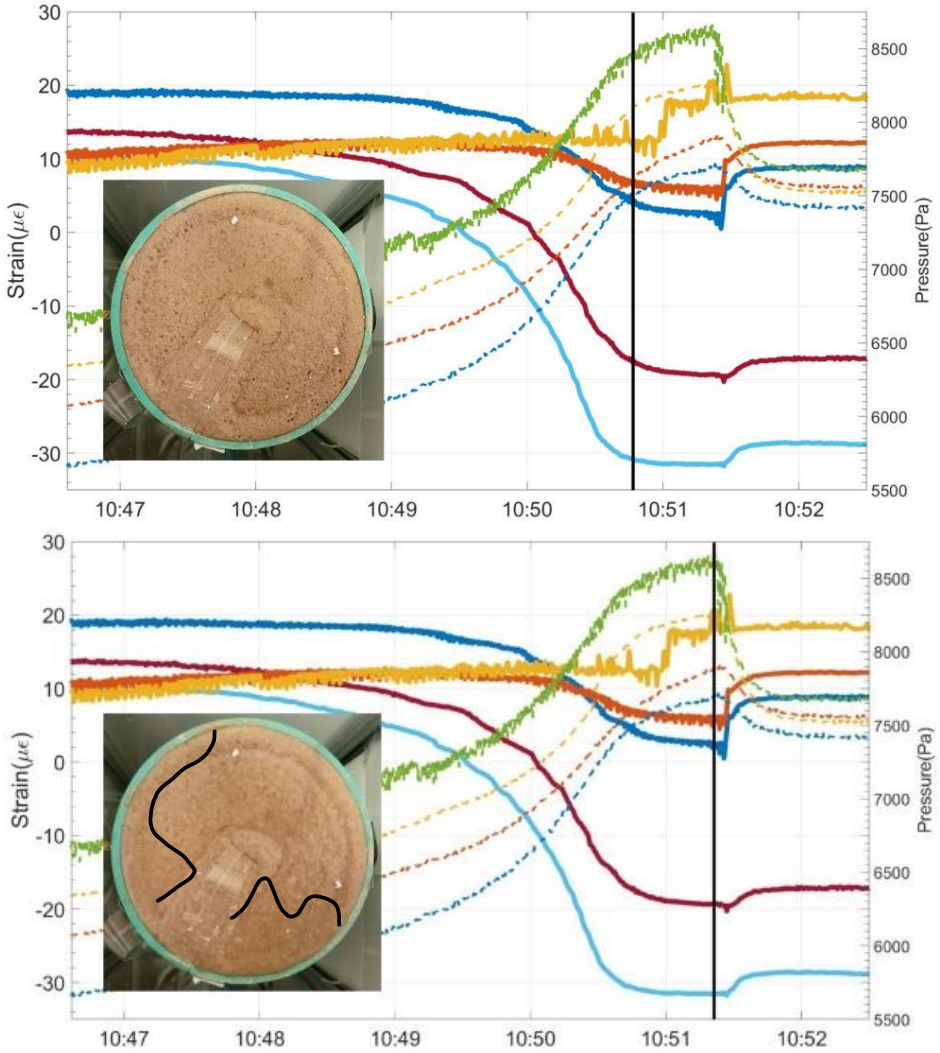

e. Full saturation of the surface.

f. Maximum saturation of surface. Areas of deep standing watter are circled.

Figure 62: Photographs taken from above the column during surface interactions along with strain and pressure time series from 10/27 test (pumping starts at *t* = 10:16). Image from time specified with vertical black line.

Compression of the sand in the column occurs as the pressure transition zone approaches the free surface and continues as the surface becomes saturated and covered by ponded water (Figure 62 a.-f.). For example, the strain at s5060 starts to decrease (become more compressive) at approximately t = 10:47 and the rate steepened for the next few minutes resulting in a total of 40 με of compression (-30 με relative to the initial conditions). The strain rate increases steadily for several minutes and reaches a

maximum of approximately -45 με/minute (-0.75 με/s) at *t* = 10:50. This is more than an order of magnitude faster than the dilational strain that occurred before the free surface interaction. This fast strain rate abruptly stops at approximately *t* =10:50:30, and the strain is essentially constant during the last 30 seconds of injection at s5060. The strain signal at the underlying sensors is similar to the one at s5060, the strain becomes increasingly compressive and then it abruptly stops before the pump is turned off. The time when this effect starts increases, and the magnitude of the strain change decreases with depth, however. This suggests that interactions with the free surface affect strain throughout the column, and this effect propagates downward from the free surface.

The pressure throughout the column is also affected during this period, and the changes in the strain signal outlined above appear to be related to changes in pressure and saturation. In general, pore pressure increases roughly linearly behind the pressure transition zone, but the slopes increase during interaction with the free surface. This appears to occur at roughly the same time as the decrease in the strain rate in Figure 63, although the increase in the pressurization rate appears to occur 100 s or more later than the decrease in the strain rate in the 10/16 test, as shown in Figures 61 and 62. The pressure increases and reaches maximum positive rates at the same time that the strain rate reaches maximum negative rates (e.g. at 10:50:30 for s5060 and p60, Figure 63d). Both the pressurization and strain rates flatten after this time.

The appearance of the surface of the sand changes as the water content increases and free water appears (images in Figure 63). The change is apparent at t = 10:49:30 when two arcuate bands become darker than the rest of the sand. The darker bands are

slight depressions in the surface of the sand, and the color change occurred because the water content increased in those regions (Figure 63a). The darkened region expanded with time, following the lowest lying topography in the surface, and by 10:50:15 it covered much of the interior of the column (Figure 63c). Free water appeared first as glistening droplets at the bottom of the arcuate bands at approximately 10:50:30, and then it progressively filled the shallow depressions in the surface (Figures 63 d-f). Free water covered the entire surface of the sand when the pump was turned off at t =10:51:25.

Images of the surface of the sand offer an explanation for the pressure and strain data. The data suggests that the pressure rate increased when the transition zone reached the sand surface. This caused the water content to increase and the surface to darken. Flow of water out of the sand was initially inhibited, however, and this caused the pore pressure to increase. A similar effect occurs where infiltrating water is initially excluded from entering a cavity (Philip & Knight, 1989). The maximum rate of pressure increase occurred just as the first signs of free water appeared at the surface of the sand. The rate of pressurization then quickly diminished to small values as the free ponded water spread across the surface of the sand.

The capillary exclusion effect appears to explain the changes in the pressurization rate, and the pressurization rate is related to the strain rate. Strain and pressurization rates are related during filling of the column, but the effect that occurs during interaction with the free surface is different from the earlier occurrences. Perhaps the most striking difference is that strain is positively correlated with pressure during most of the test, but they are negatively correlated during the period characterized by interaction with the free

surface—that is, an increase in pressure in the interior of the column is associated with an increase in strain (dilation), but an increase in pressure at the free surface is increasing is associated with compression. Moreover, the strain rate that occurs during the free surface interaction is much faster than when the pressure is changing within the column.

Turning off the pump causes the pressures to decrease as the 0.2 head gradient caused by the upward flow of water collapses. This means that the pressure drop is greatest in the bottom of the column and diminishes upward. The pressures measured by the sensors return to within 250 Pa of each other, which corresponds to essentially uniform head in the column (cite figure). Turning off the pump is accompanied by sharp tensioning in lower parts and a more gradual effect in the upper regions of the column. Presumably, these strains are a result of the pressure changes associated with stopping flow. Interestingly, the pressure and strain are negatively correlated during this period, just as they were during the interaction with the free surface. After this, strain and pressure stabilize until the drainage of the column is initiated.

Pump Off

The strain changes little when the pump is turned off.

Pumping Out Drainage

When the pump is turned on in reverse to drain the column, sharp initial tensioning occurs. A more gradual tensioning rate occurs after this that lessens and eventually turns negative (compresses). s5060 reaches a tension maximum first and then

begins compressing. This effect moves downwards to the lower sensors with progressively lower tensioning and peaks later in time (Figure 63 and Figure 64).

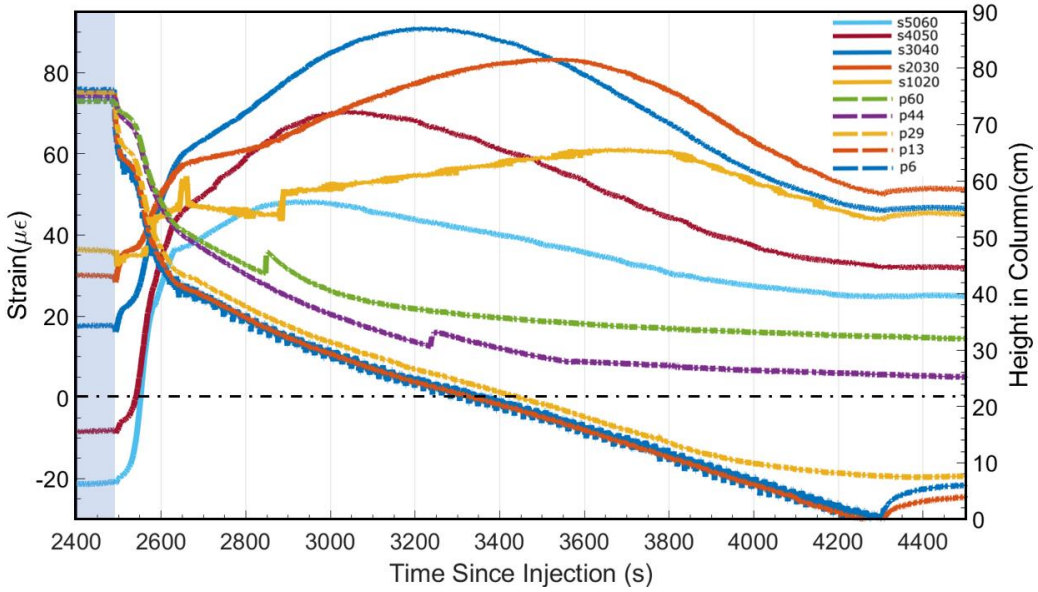

Figure 63: Strain and total head during the drainage portion of the 10/16 test. Blue band is the period of no-flow. Drainage by pumping out starts at t = 2,480 s.

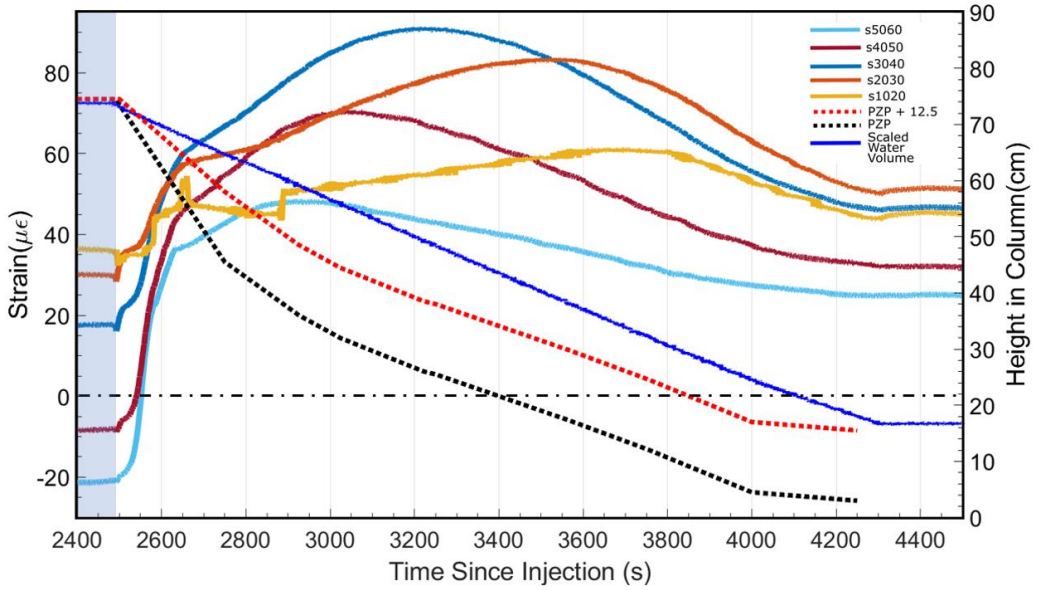

Figure 64: Strain, scaled water volume, and transition zone (PZP to PZP + 12.5 cm) height as functions of time for the drainage portion of the 10/16 test. Blue band is the period of no-flow. Drainage by pumping out starts at t = 2,480 s.

Gravity Drainage

The start of gravity drainage coincides with rapid tensioning. this tensioning rate lessens, reaches a maxima of as much as 65 με and then decreases. s5060 reaches a maximum (50 με) first and s1020 reaches a maximum (15 με) last with the sensors in between reaching the maximum in order of height above the datum. The largest strains occur at s3040 and s4050 and reach 65 με. The maxima reached from gravity drainage are less than the maxima reached during drainage by pumping in reverse. For example, the maximum strains that occurs at s3040 and s4050 during pumping in reverse are between 80 and 85 με, approximately 15 to 20 με greater than during gravity drainage. After the maximum is reached, compression occurs more gradually than tensioning (Figure 65 and Figure 66).

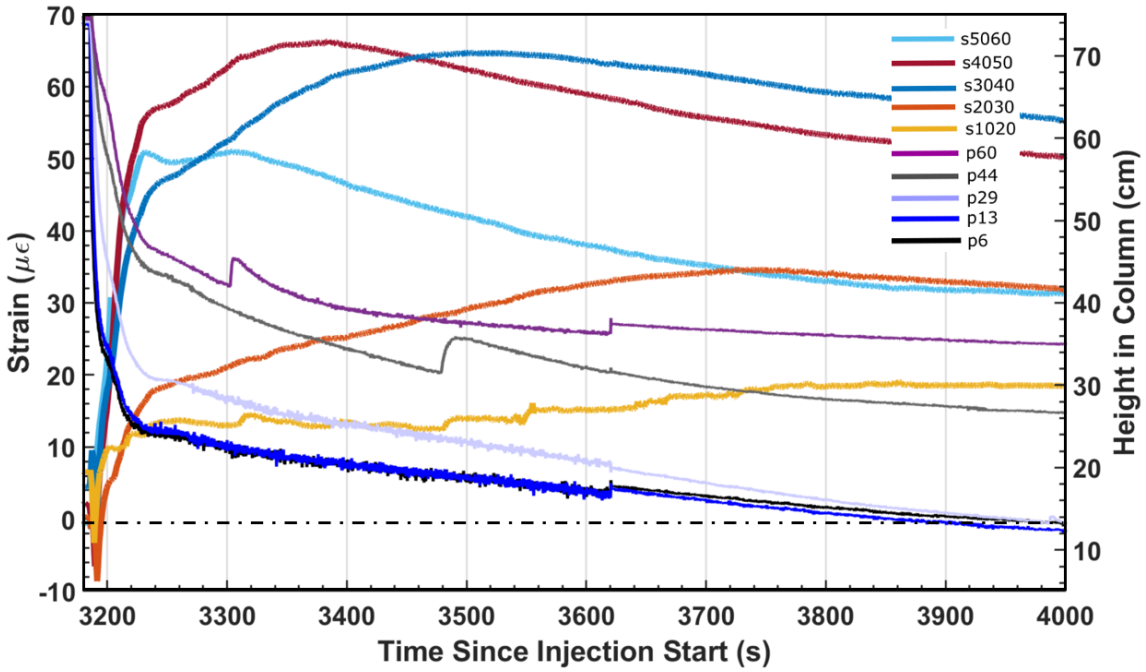

Figure 65: Strain and total head time-series for the drainage portion of the 10/25 gravity drainage test.

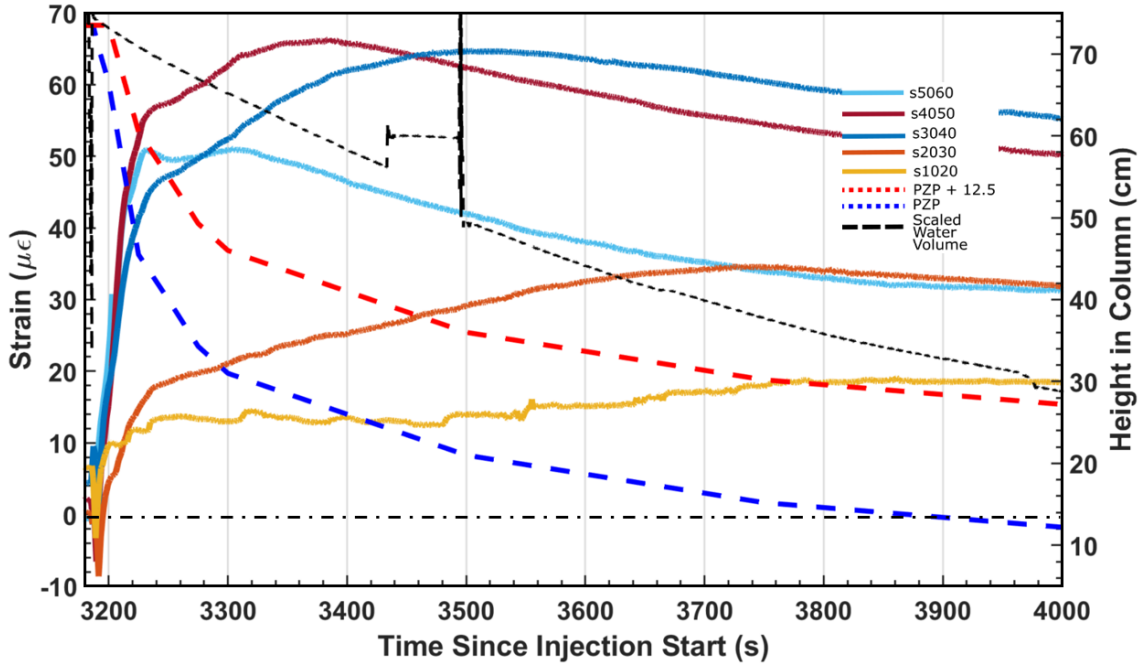

Figure 66: Strain, scaled water volume, and transition zone (PZP to PZP + 12.5 cm) height as functions of time for the gravity drainage portion of the 10/25 test. Blue band is the period of no-flow.

PATTERNS AND REPEATABILITY

Repeatable patterns in the time-series emerge from the data. These changes in strain seem to be due to changes in pressure and the movement of the transition zone. The general pattern for the column is tensioning when the PZP/wetting front enters the reflection zone. When the PZP moves above the reflector zone, the tensioning rate slows and then generally stops. Slight compression or tension can occur as the PZP moves higher. At a certain point, tensioning occurs again most likely due to the increase in pressure.

To better envision the patterns found from the data, the injection tests were conglomerated with normalized start times with zero being the start of injection. Differences occur during the tests supposedly due to differences in the starting conditions of the column. Because these tests were conducted on the same column separated by days, the column has a starting PZP and saturation curve above it. This results in the PZP reaching the surface of the column at different times. These times differ by up to 600 seconds.

Five tests were compiled for the series. The before mentioned Partial-Fill test and 10/16 test, as well as three gravity drainage tests. The 10/23 test was the first gravity drainage test conducted. Drainage had to be stopped a few seconds after the drain was opened dur to an improper placement of the outflow tubing resulting in a higher outflow head than planned. This issue was resolved, and the drainage continued as planned. The 10/25 test filled up quicker than the other injection tests, due to a higher starting saturation and PZP and appears numerically apart from the rest of the tests during

injection. The column was then drained by gravity. The overall patter of the 10/25 test is consistent with the other tests shown. The 10/27 gravity drainage test had no issues or inconsistent data.

The software Inkscape is used here to create graphs of the standard responses to injection and drainage. The thick black line represents the 10/16 injection/pumping out test earlier described. Grey shading represents the variability found during injection and ponding stages of the different tests. The blue dashed line is the typical gravity drainage response, formed graphically by comparing the 3 gravity drainage tests. The red dashed line represents the partial injection test described earlier extrapolated out in time to better compare with the other tests.

Different stages appear in the patterns of strain data related to the position of the transition zone and PZP. These regions are labeled and shaded for easier viewing. The stages shown correspond to the 10/16 test.

Stages 1-4 and Stage w represent stages during injection. Stage 1 represents the injection stage where little response occurs. The transition zone is below the sensor during this stage. Stage 2: Tensioning begins, the transition zone reaches the bottom reflector, and the stage continues until the PZP is above the top reflector. Stage 3: The PZP is above the top reflector and tensioning slows, stops, or even reverses into compression. Stage 4: The PZP is far above the sensor. Stage w: The transition zone reaches the surface of the column and continues until the PZP reaches the surface resulting in ponding. This results in large compression throughout the column.

Stages a-d represent stages during drainage. Stage a: Pumping out starts and the column tensions. This stage continues until the pond is fully drained from the surface. Stage b: This stage starts with the drainage of the surface resulting in the PZP being below the surface and a transition zone. This continues until PZP reaches the top reflector. Stage c: The PZP reaches the top reflector and continues until the transition zone passes the bottom reflector. Stage d: The transition zone is beyond the bottom reflector and continues until the pump is shut off.

s1020

The s1020 sensor starts tensioning at the start of injection (Figure 67). This tensioning slows and sometimes stops. It later resumes again and continues until surface wetting (Figure 68).

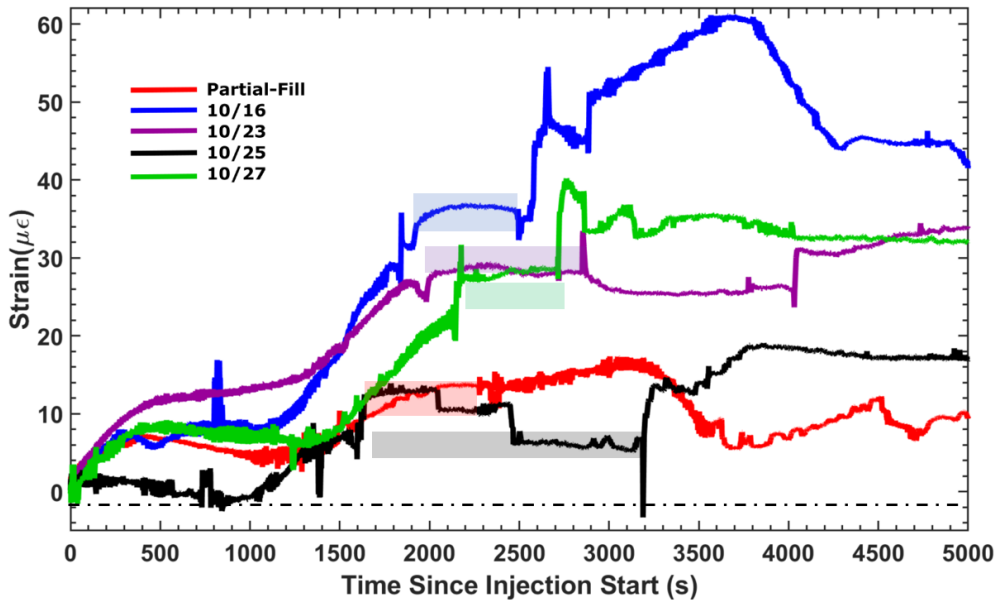

Figure 67: Strain time-series at s1020 sensor for five injection tests conducted on different dates with normalized start times. The No-Flow interval is represented by the transparent bands of the same color.

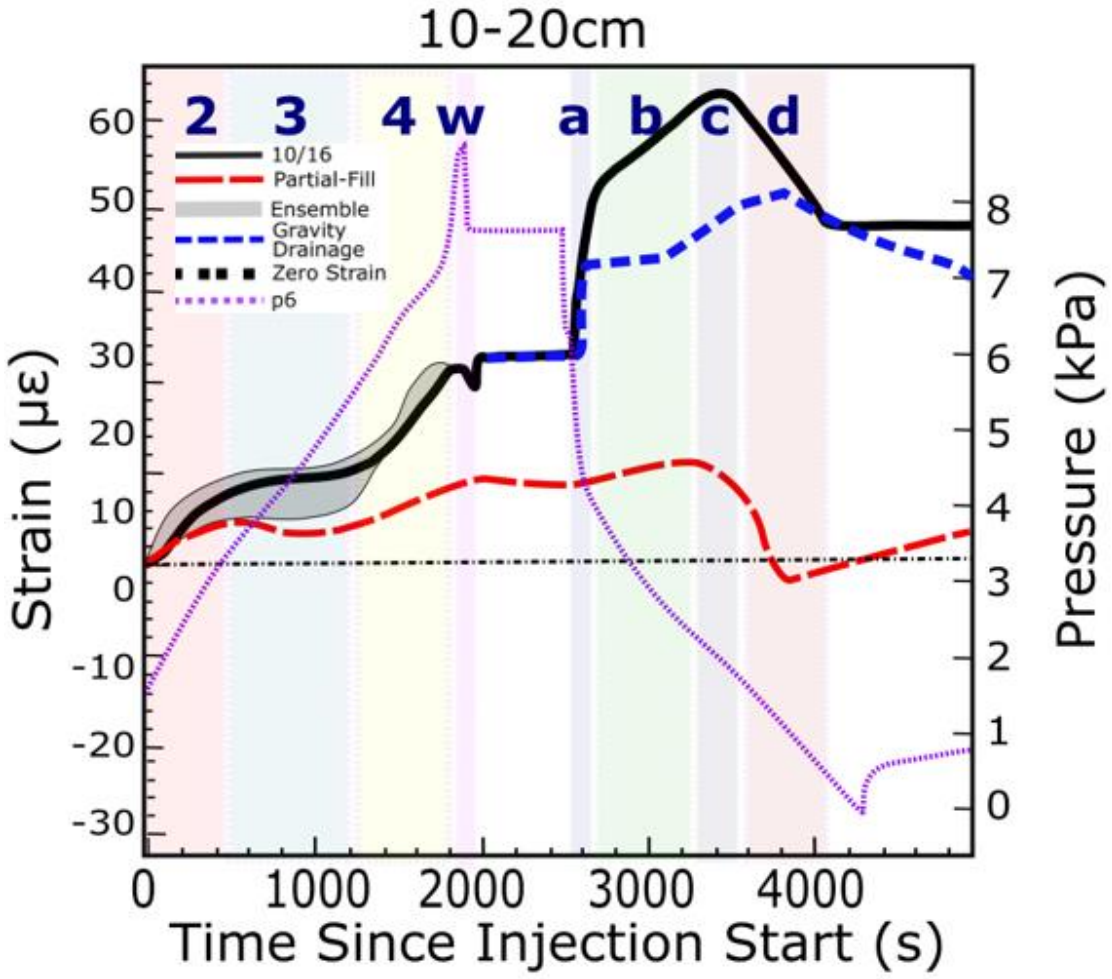

Figure 68: Ensemble strain and total head as pressure time-series for s1020 and p6. The white band is the no-flow interval.

Stage 1 is absent in this data set. The strain at s1020 is rapidly tensioned by approximately 2 με at the start of pumping (best seen n Figure 36 and somewhat in Figure 60). The reflector and p6 tensiometer is below the PZP at the start of the experiment. After turning on the pump, tensioning occurs linearly at a rate of approximately 0.025 με/s during Stage 2. Strain stabilizes after this period beginning Stage 3. Slight compression or tensioning can occur. Tensioning occurs during Stage 4 after Stage 3 at a rate of slightly higher than the first tensioning period (0.03 με/s). All

injection tests have the pattern of early tensioning, a period of little change, and a later period of tensioning (Figure 67). The strain at s1020 decreases by approximately 2 με when the pressure transition zone reaches the surface of the sand during Stage w, a response that is much less than the compression that occurs at the overlying strain sensors. The strain then stabilizes and is constant at a 30 +/- 5 με during the period of No-Flow (Figure 67).

Upon drainage the region undergoes tension during Stage a. Drainage causes interactions between the PZP and the surface of the sand, similar to the interactions during injection and the surface wetting. Sharp tensioning occurs during this initial drainage period. Two different types of tensioning occur after this. The pumping out case shows a gradual tensioning at a rate of 0.017 με/s. The tensioning during pump out peaks at around 900 seconds after the start of pumping in reverse. After this peak, compression occurs at a rate of 0.028 με/s. This continues until the pump is turned off.

The gravity drainage case shows a slight sharp initial tensioning followed by a gradual tensioning that eventually peaks and turns to compression.

s2030

The s2030 sensor begins tensioning at the start of injection (Figure 69). It later slows and sometimes compresses. Tensioning then resumes until surface wetting (Figure 70).

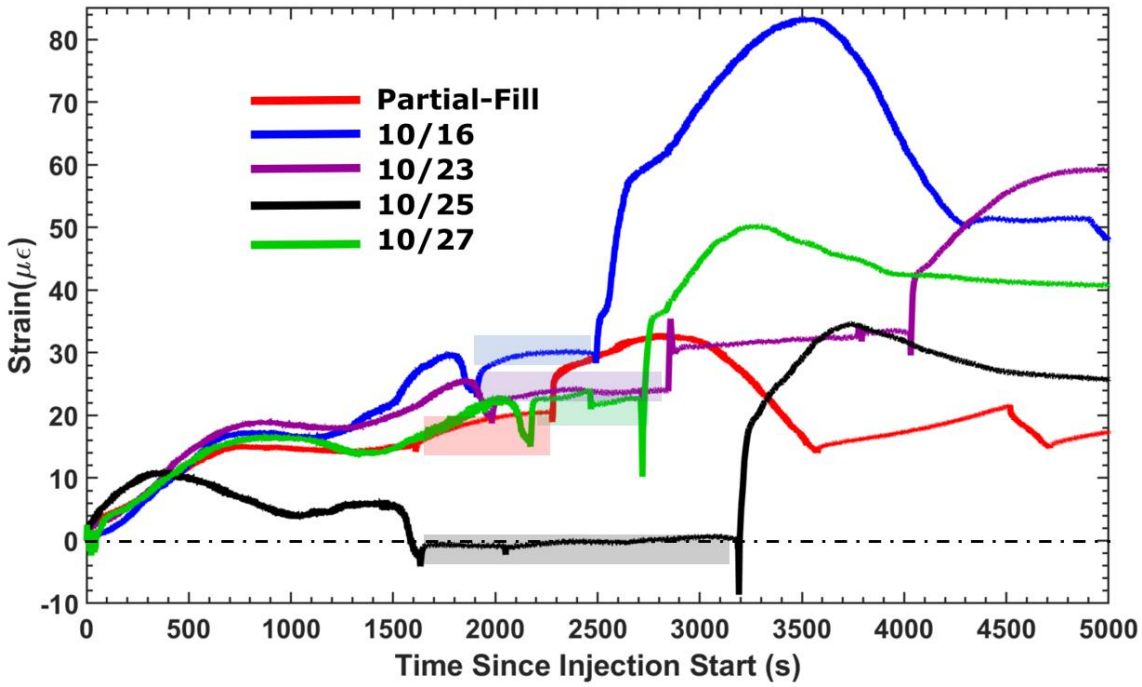

Figure 69: Strain time-series at s2030 sensor for five injection tests conducted on different dates with normalized start times. The No-Flow interval is represented by the transparent bands of the same color.

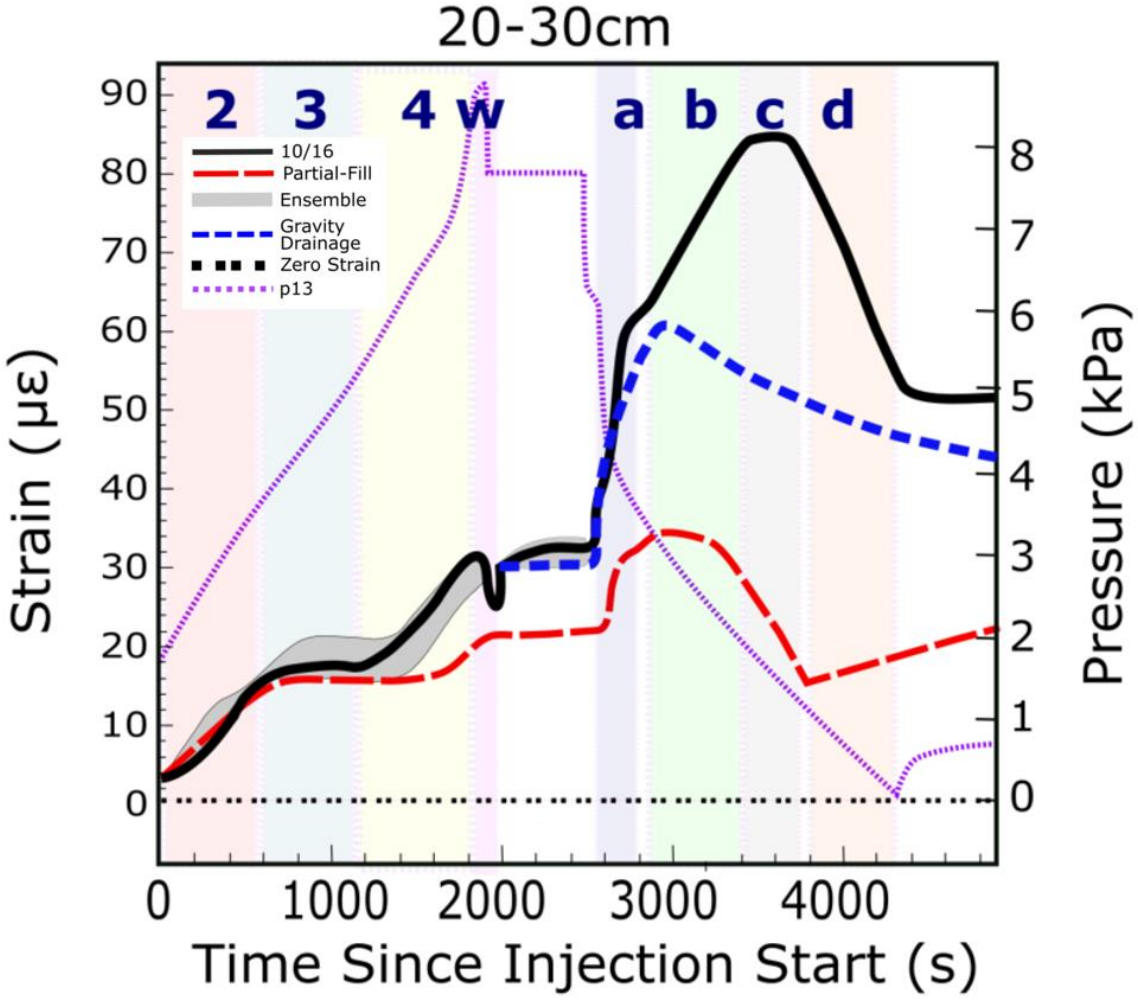

Figure 70: Ensemble strain and total head as pressure time-series for s2030 and p13. The white band is the no-flow interval.

This sensor responds similarly to the bottom strain sensor. An initial tensioning occurs of approximately 1 με when injection starts (Figure 70). Linear tensioning occurs at around 50 seconds after the start of injection at a rate of 0.025 με/s during Stage 2. The tensioning rate begins slowing and rounding off to a period of stability (Stage 3). During this stage slight compression can occur. At around 1,300 seconds, Stage 4 begins, and a second period of tension occurs. This has a similar rate of tensioning as before 0.025 με/s.

This region compresses slightly by 6 με when the transition zone reaches the surface of the sand at the top of the column, more than the sensor below it (Stage w). When drainage starts, sharp tensioning occurs (Stage a). The pumping out case shows a tensioning rate of 0.044 με/s during Stage b. This peaks at 35 με at t = 1,050 s during Stage c. This is higher than the lower sensor. The strain compresses at a rate of 0.050 με/s during Stage d and continues until the pump is turned off (Figure 70).

The gravity drainage case shows sharper strain rate change initially that then linearly tensions at a rate of 0.050 με/s. This peaks at 38 με 530 seconds after drainage starts and then compresses gradually as water is drained from the column (Figure 70).

s3040

The s3040 sensor usually does not begin increasing at the immediate start of injection (Figure 71). Tensioning starts later and reaches a maximum. After this it stabilizes and can compress. Tensioning can resume after this period and continue till surface wetting (Figure 72).

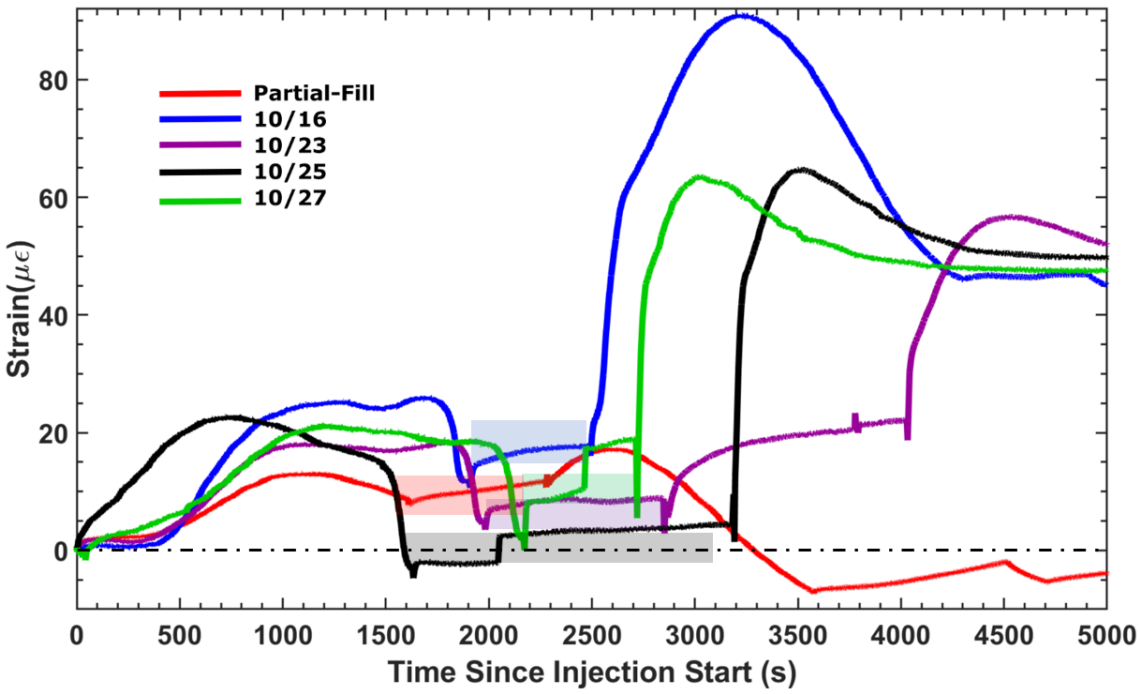

Figure 71: Strain time-series at s3040 sensor for five injection tests conducted on different dates with normalized start times. The No-Flow interval is represented by the transparent bands of the same color.

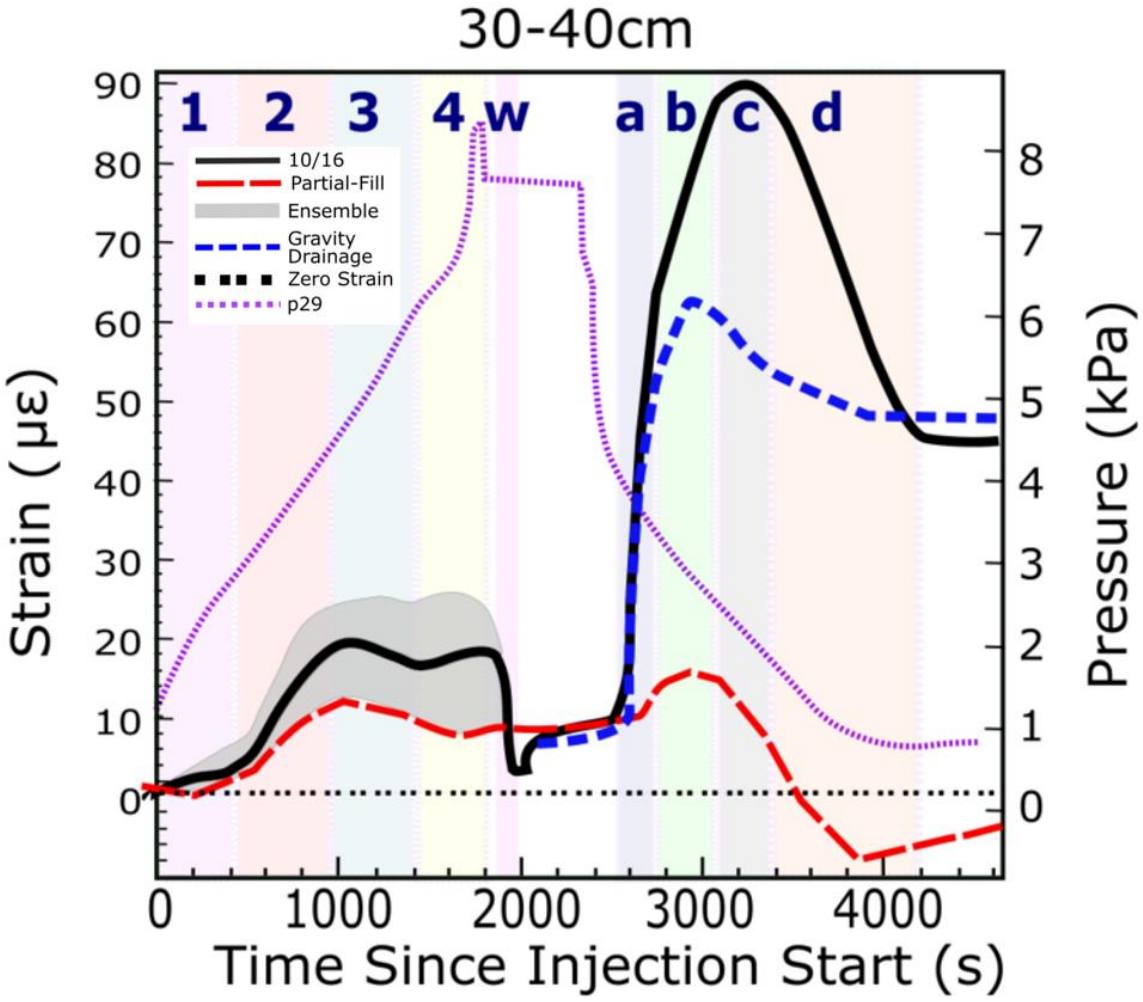

Figure 72: Ensemble strain and total head as pressure time-series for s3040 and p29. The white band is the no-flow interval.

Often initial tension occurs when the pump is first turned on, approximately 0.5 με, followed by a period of stability (Figure 72). Stage 1 is first present in this sensor. The strain goes into linear tension at around t = 400 to 900 s during Stage 2. The rate of tensioning is approximately 0.037 με/s. This corresponds to the transition zone reaching the area between the reflectors and ends with complete saturation in the length between the reflectors. After this stage, the tensioning rate flattens and can slightly compress (Stage 3). At around t = 1,500 s, Stage 4 begins, and new tensioning occurs. This rate is

similar to the start of the first tensioning period before linearity occurs. Interactions between the transition zone and the surface in Stage w coincide compression of approximately 15 με. The injection tests, other than the 10/25 test, show the pattern of little initial change, tensioning, a decrease of the tensioning rate, followed by

Once drainage begins, a sharp tensioning occurs of approximately 42 με (Stage a). Tension rate slows to 0.068 με/s after this in Stage b. The strain reaches a maximum of 73 με above pre-drainage values 350 seconds after the start of drainage in Stage c. After this maximum, the region compresses at a rate of 0.057 με/s in Stage d until the pump is shut off (Figure 72).

In the gravity drainage scenario, the tension maximum is reached sooner but is less than in the pumping out case (60 με). After the maximum, the region compresses gradually (Figure 72).

s4050

The s4050 sensor remains relatively stable (though compression sometimes occurs) from the start of injection until approximately t = 600 s when tensioning occurs. Tensioning reaches a maximum and then stabilizes and slightly compresses. (Figure 73) and ensemble (Figure 74).

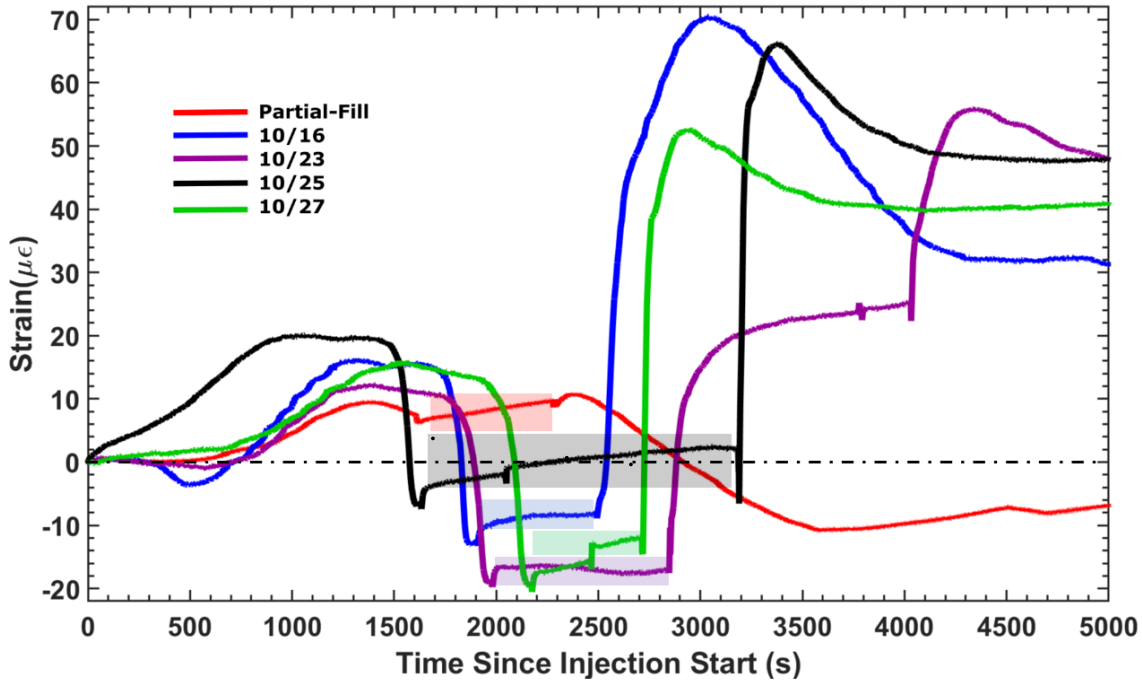

Figure 73: Strain time-series at s4050 sensor for five injection tests conducted on different dates with normalized start times. The No-Flow interval is represented by the transparent bands of the same color.

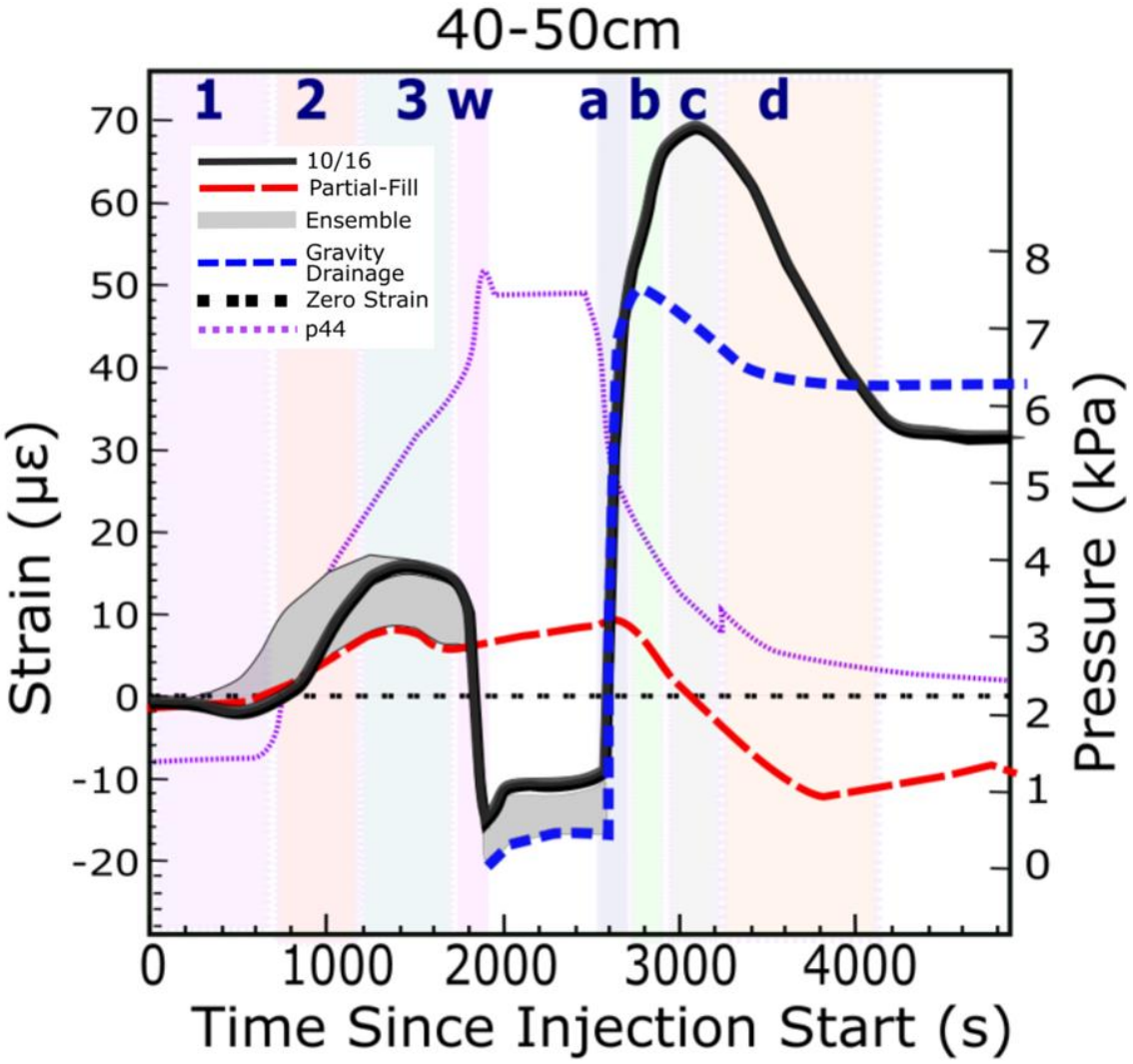

Figure 74: Ensemble strain and total head as pressure time-series for s4050 and p44. The white band is the no-flow interval.

The s4050 reflector and p44 tensiometer data remain unchanged (although very slight compression can occur) when the pump is turned on at t =0 to t ~700 s (Stage 1) (Figure 74). After this point, the strain during Stage 2 increases at a rate of roughly 0.026 με/s for 500 s (until t ~ 1,200 s), and then the strain rate diminishes to zero or slightly negative (Stage 3). Stage 4 is absent in this sensor. The strain compresses by approximately 30 με during surface interactions (Stage w).

Pumping out the column coincides with a sharp tensioning of 53 με over 150 seconds (Stage a). The tensioning rate slows to a rate of 0.087 με/s during Stage b. This tension reaches a maximum of 80 με during Stage c 300 seconds after the start of drainage. After this maximum, compression occurs at a rate of 0.040 με/s during Stage d (Figure 74).

Gravity drainage of the column shows a sharper initial tensioning, 50 με over 50 seconds. After the initial tensioning, linear tensioning of 0.16 με/s occurs. Tensioning peaks at 64 με. Gradual non-linear compression then occurs (Figure 74).

s5060

The s5060 sensor (Figure 75) is gradually compressed at the start of injection and then begins tensioning. This continues until surface wetting (Figure 76).

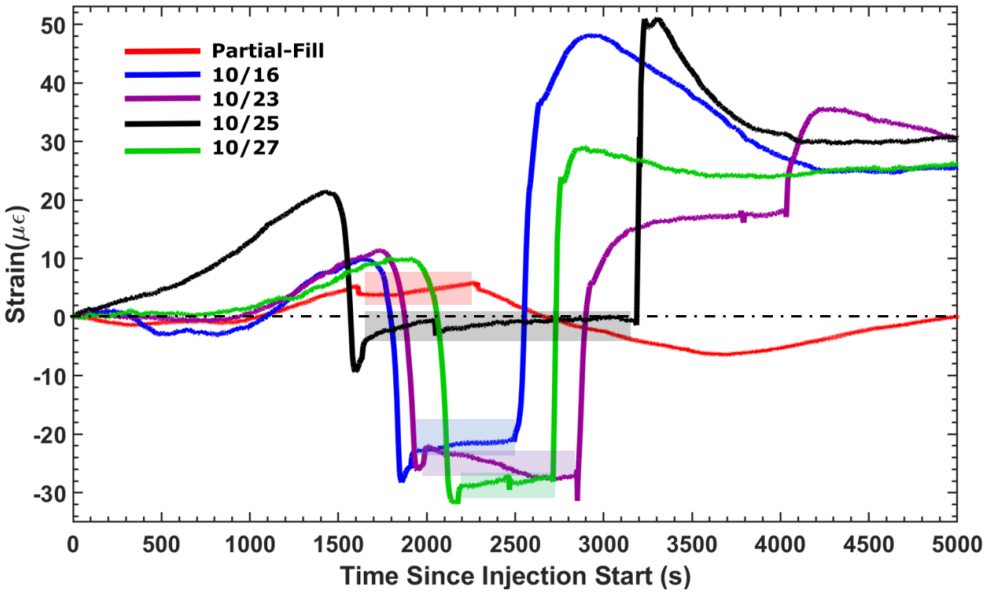

Figure 75: Strain time-series at s5060 sensor for five injection tests conducted on different dates with normalized start times. The No-Flow interval is represented by the transparent bands of the same color.

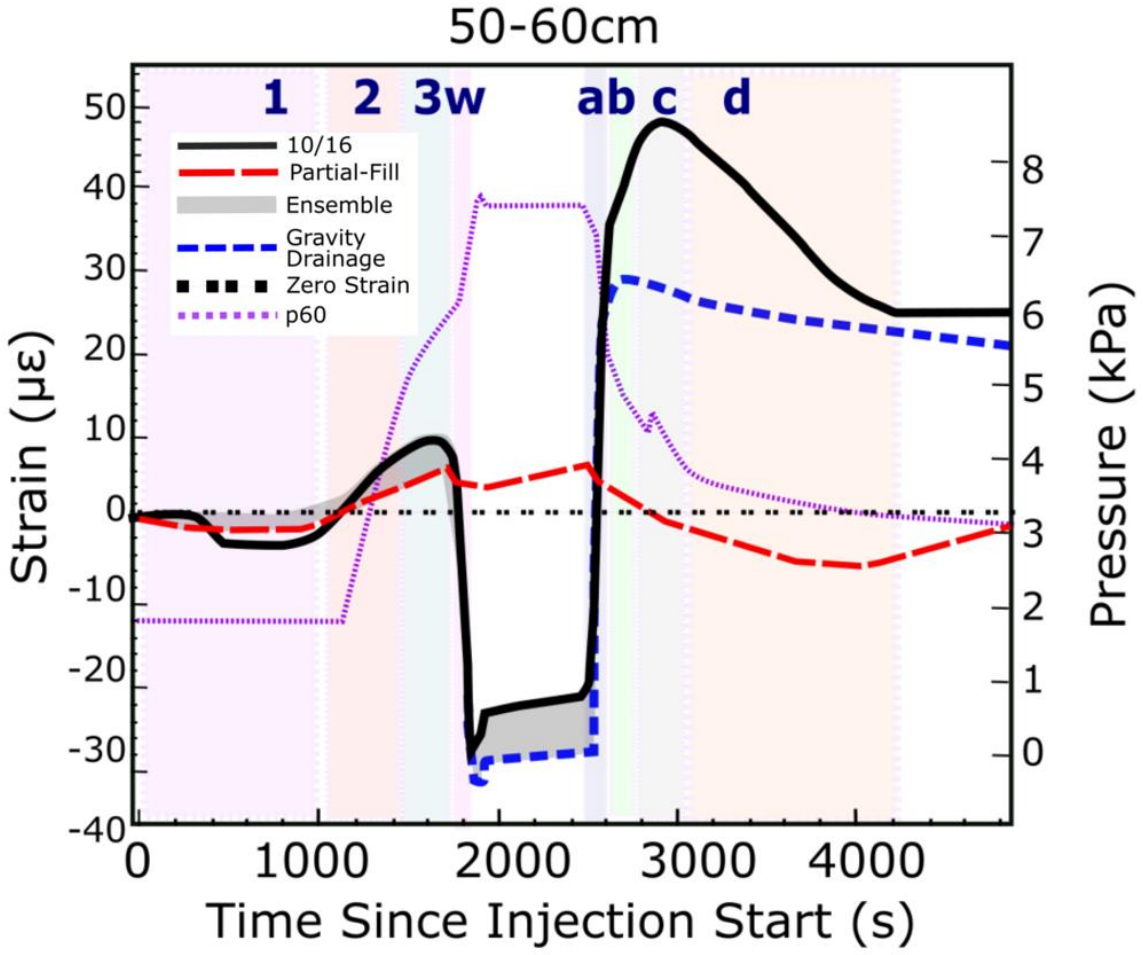

Figure 76: Ensemble strain and total head as pressure time-series for s5060 and p60. The white band is the no-flow interval.

No response is recorded when the pump is turned on at the start of the experiment from s5060 and p60 (Figure 76). During Stage 1, slight compression can occur as the PZP moves through the column. Tension occurs linearly during Stage 2 when the transition zone moves between the reflecting region at approximately 0.018 με/s beginning at t = 900 s. This tensioning slows and stops as the transition zone moves above the top reflector (Stage 3). Typically, this happens at t = 1,800 s. Rapid

compression occurs as the transition zone reaches the surface of the sand. The compression during Stage w is greatest in this sensor at approximately 35 με.

Upon pumping out in Stage a, an initial tensioning of 58 με occurs over 150 seconds. During Stage b, gradual tensioning occurs at a rate of 0.040 με/s. This rounds out to a peak of 69 με in Stage c 250 s after the pump is turned on. Compression occurs at a rate of 0.022 με/s in Stage d (Figure 76).

Draining of the column by gravity initially shows rapid tensioning in this sensor. The value of this tensioning is approximately 51 με over 50 seconds. Linear tensioning occurs for 50 seconds after this at approximately 0.083 με/s. Slight gradual compression occurs after this (Figure 76).

Displacement Over the Sensor

Disregarding the distributed nature of the optical fiber sensor further illustrates repeatability. The total displacement is parallel to the total strain. The total displacement of the optical fiber can be found by converting the individual strains into displacements by multiplying by the length between the reflectors (0.1 m) and adding the individual displacements up.

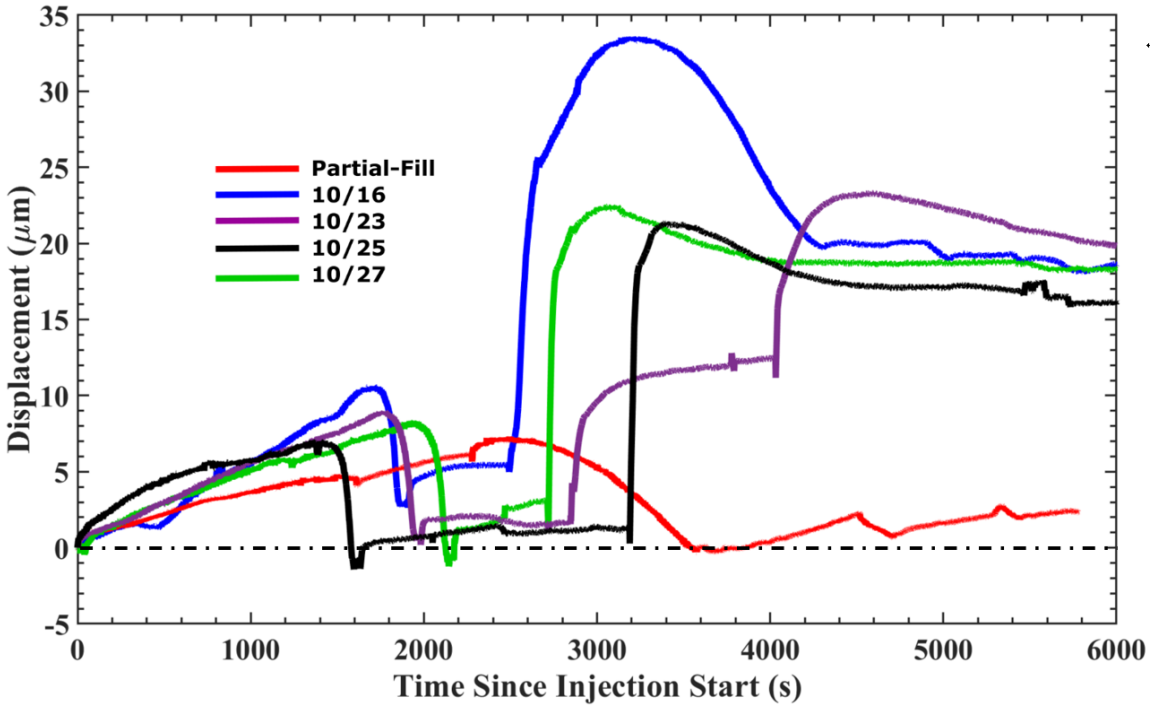

Figure 77: Total displacement time-series of the five tests.

The pattern of total displacements shows a lengthening during injection of between 5 and 10 µm (Figure 77). The fiber is compressed by a similar amount during the surface wetting stage. Dropping the pressure during drainage after complete surface saturation lengthens the fiber by 15 to 20 µm. The resulting displacement at the end of the experiments in the complete fill and drain tests is roughly 20 µm in added length. The optical fiber during the partial fill test with no surface interaction returned to approximately its original length.

PRESSURE AND STRAIN BEHAVIOR

As seen in the experiments, changes in pressure result in changes in strain. Changes in strain during injection have some linearity to them when the transition zone

passes between the reflectors. Strain and pressure changes during surface interactions (Stage 4) is comparatively large and occurs over a short period of time. When the strain is plotted against the pressure, the path the strain sensors go through can be seen. Surface interactions lead to repeatable responses that are clearly different from pressure and strain changes seen in other times in the experiments. These surface interaction events are shown as linear paths in the strain and pressure. Particularly in s2030 s3040 s4050 and s5060, the path the strain and pressures take seems somewhat repeatable. The erratic nature of s1020 makes this analysis unpredictable during stage 4 at this sensor. The slope of these linear paths reveals something resembling a modulus for the sand. This slope can be between 37 and 112 MPa. This is not exactly the moduli predicted for the sand but is within the range of reasonable values.

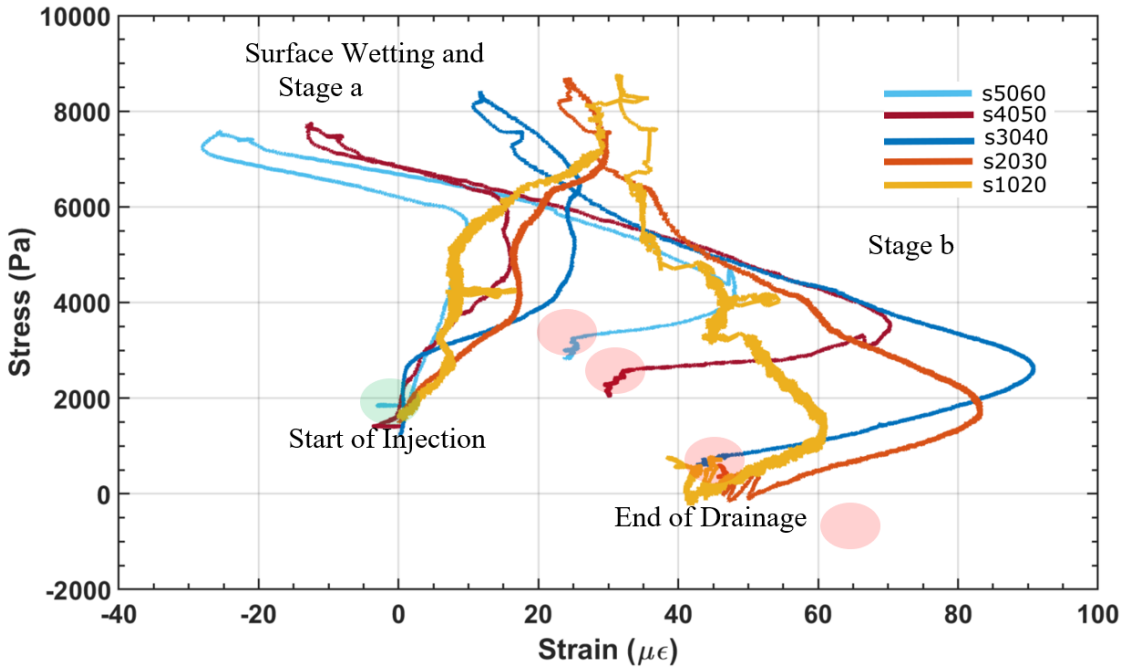

Figure 78: Strain and pressure during injection and pumping out for the 10/16 Injection Test. Surface wetting occurs at roughly t = 1800 s.

Stage b of drainage shows a similar modulus in the linear regions of roughly 47 MPa s5060, s4050, and s3040. s2030 has a modulus of 67 MPa. S1020 has a stiffer modulus of 112 MPa. The moduli increase with depth (greater confining pressure). These moduli are reasonable compared to the values for Young's modulus obtained during the triaxial test and the Loading Test and further confirm that these are real interactions between the water pressure and strain in the sand.

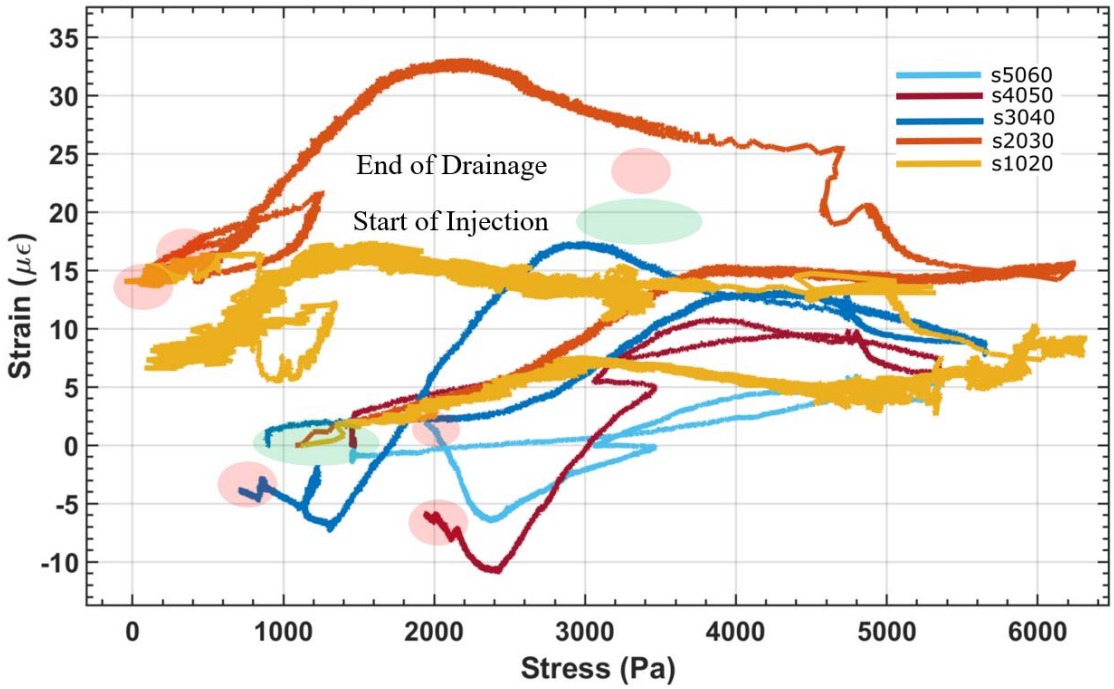

Figure 79: Strain and pressure during the Partial-Fill test.

The stress/strain relationship during the Partial-Fill test is more symmetric than the 10/16 test where surface interactions occurred. More of the strain is recovered with s3040, s4050, and s5060 ending within roughly 5 με of values at the start of injection.

OUTSIDE STRAIN SENSOR

The outside strain sensor shows changes in strain during injection and drainage tests. The best results from these sensors come from the 10/16 injection and pump out drainage test (Figure 80). This strain ribbon generally shows stretching during injection and compression during drainage.

The data have trends throughout the test. Temperature correction was not done on the strain data for the outside of the column. The temperature on directly the outside of the column is not the same temperature as on the inside temperature sensors or the temperature of the room. This is the most likely reason for the trends seen in the data. The 10/16 test shows a trend in the strain of 0.0015 με/s. These trends were removed. The trend correction is not all encompassing, but the overall pattern of the data is preserved.

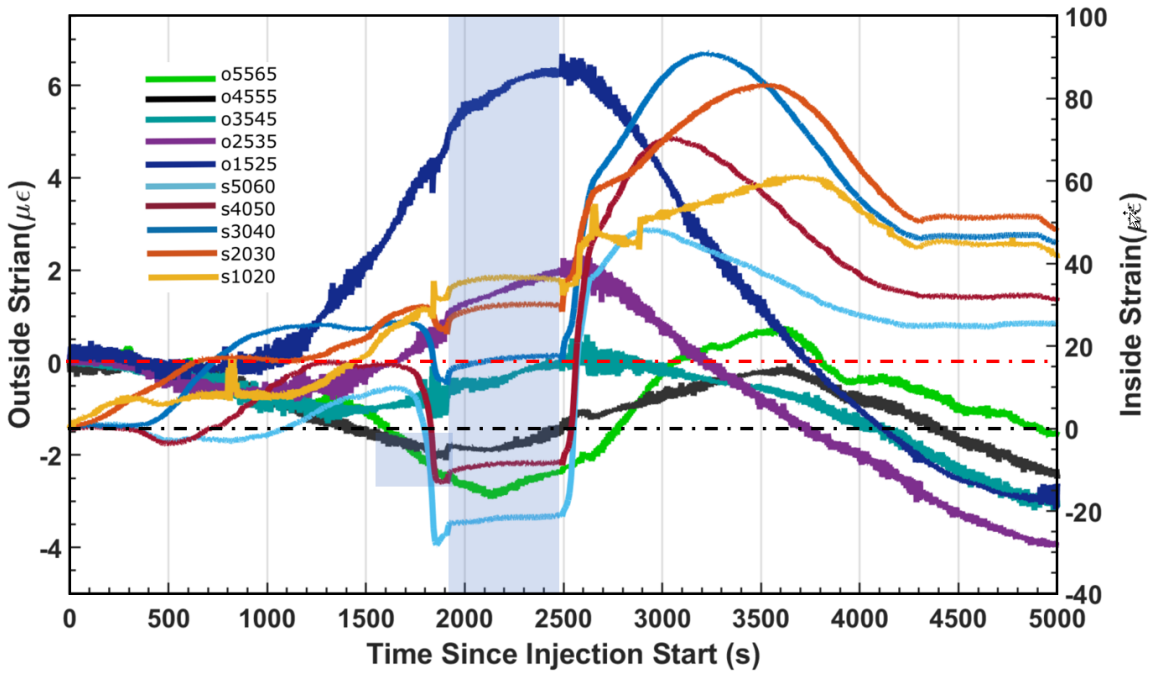

Figure 80: Time-series of the strain both inside and outside for the 10/16 test. Blue band is the period of no flow. Red dashed line is zero outside strain. Black dashed line is zero inside strain.

The patterns of data appear to be indicative of the column bulging in the lower regions and compressing in the upper regions where it is lowest. The lowest sensor is tensioned by the most and at the highest rate (Figure 81). Sensors progressively higher are tensioned by less (Figure 81-Figure 85). A midpoint between compression and tension is likely reached near o3545 due to this sensor being only slightly compressed (Figure 83). Sensors above this are compressed during injection with o5565 compressing the most (Figure 84 and Figure 85). During drainage, the lower regions of the column compress and the upper regions tension (Figure 80).

o1525/s1020

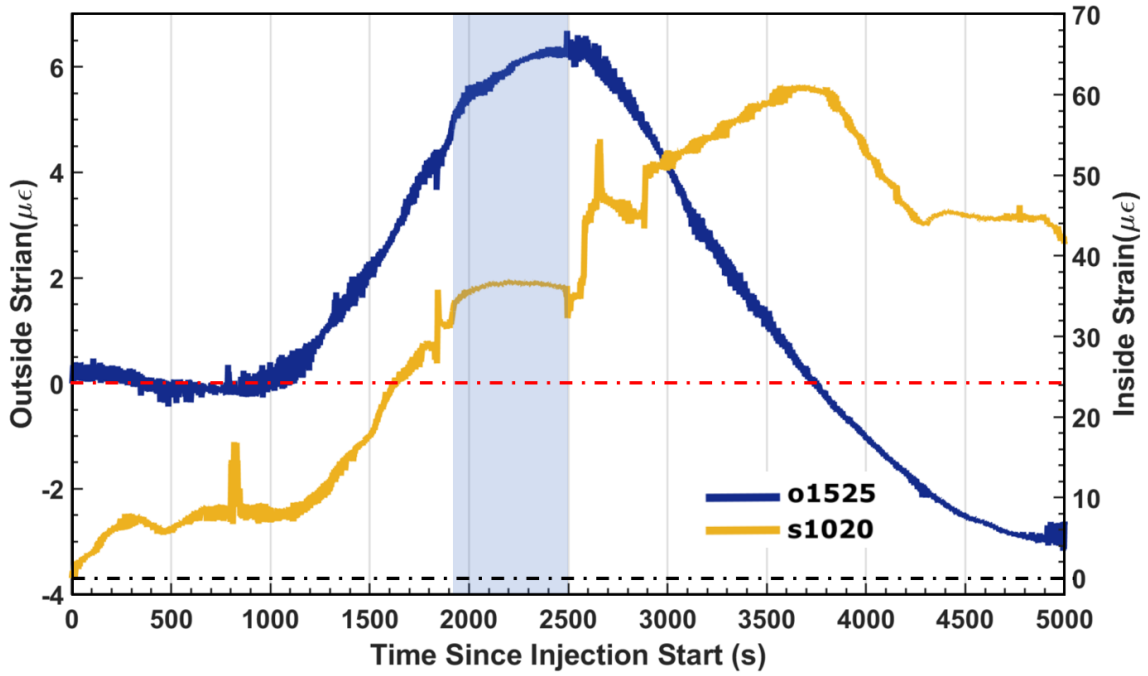

Figure 81: Strain in the sand (s1020) and PVC (o1525) for the 10/16 test. Blue band is the period of no flow. Red dashed line is zero outside strain. Black dashed line is zero inside strain.

The greatest tensioning occurs in the lower sensor. Tensioning of approximately 0.007 με/s occurs at t = 1,000 s and continues until t = 2,000 s. This reaches a maximum of approximately 8 με. Compression of 0.008 με/s occurs after the no flow period (Figure 81).

o2035/s2030

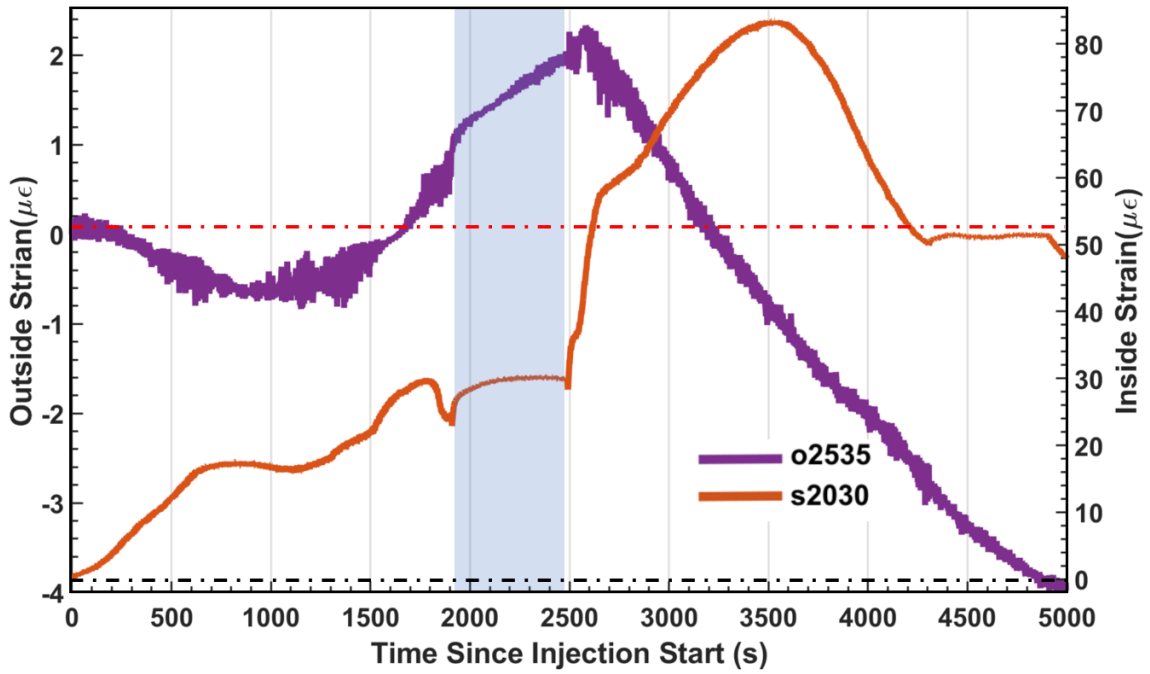

Figure 82: Strain in the sand (s2030) and PVC (o2535) for the 10/16 test. Blue band is the period of no flow. Red dashed line is zero outside strain. Black dashed line is zero inside strain.

Tensioning occurs in the 20-30cm strain sensor at t = 1,300 s and continues until the no flow period at a rate of 0.004 με/s. Compression occurs once the pump is turned on in reverse (Figure 82).

o3545/s3040

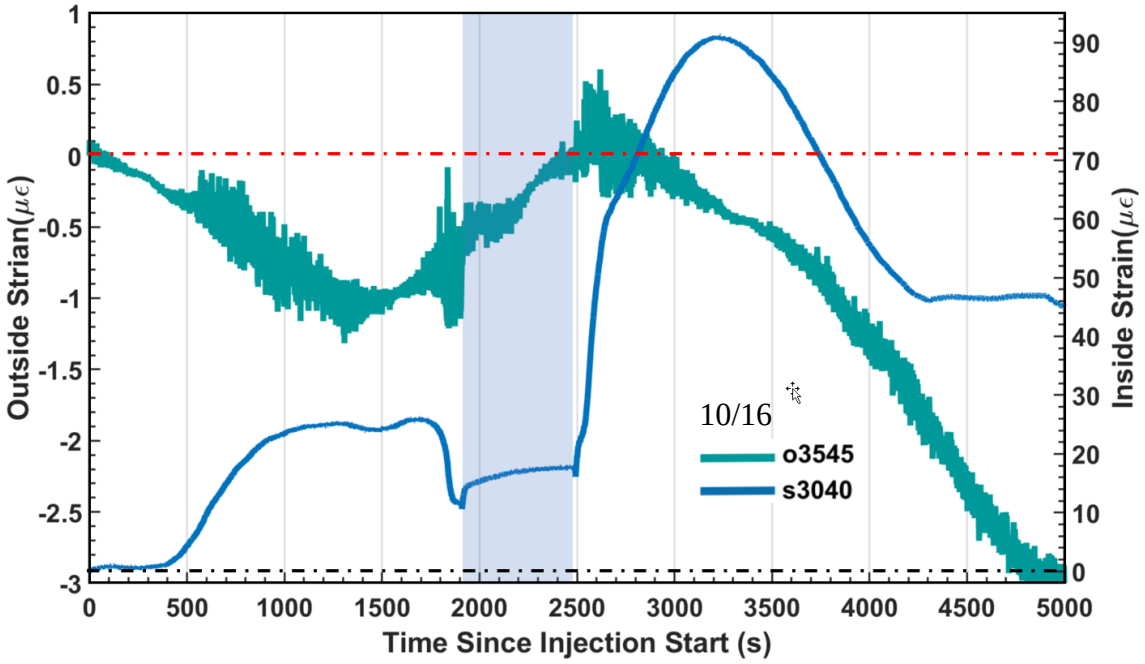

Figure 83: Strain in the sand (s3040) and PVC (o3545) for the 10/16 test. Blue band is the period of no flow. Red dashed line is zero outside strain. Black dashed line is zero inside strain.

The 30-40cm region does not appear to be affected much by the injection during the 10/16 test, however slight compression of approximately 1 με occurs followed by tensioning at t = 1,400 s (Figure 83).

o4555/s4050

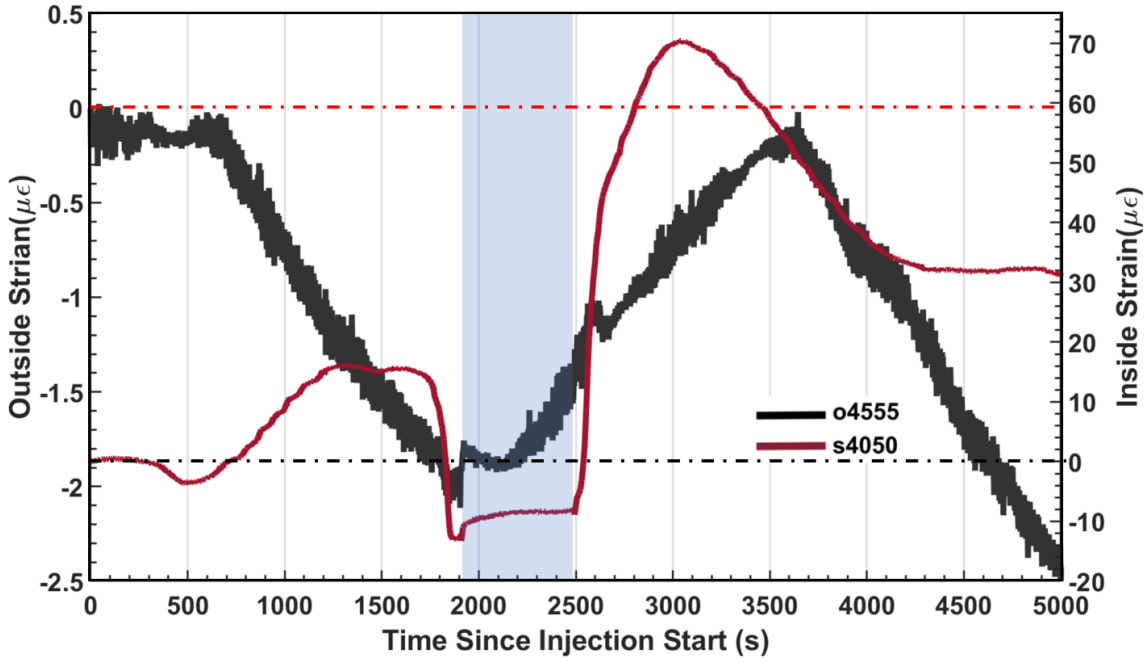

Figure 84: Strain in the sand (s4050) and PVC (o4555) for the Partial-Fill and 10/16 test. Blue band is the period of no flow. Red dashed line is zero outside strain. Black dashed line is zero inside strain.

Compression occurs t = 600 s and continues for until the pump is turned off.

Some tensioning occurs when the pump is turned on in reverse that reaches a maximum and reverses t = 3,600 s (Figure 84).

o5565/s5060

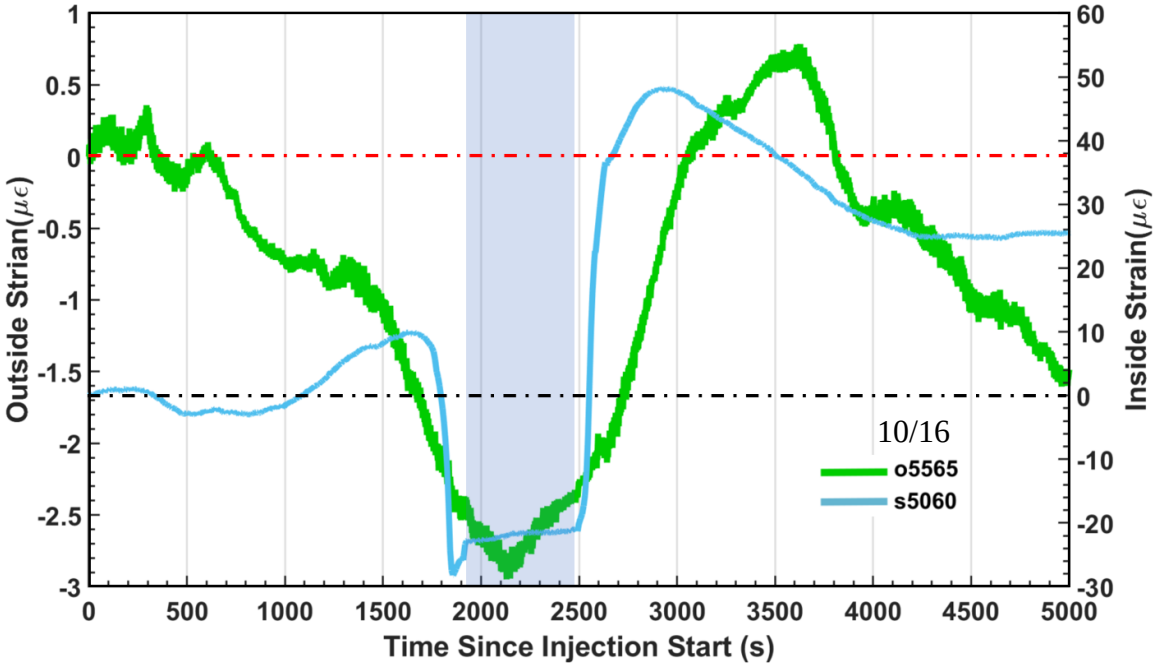

Figure 85: Strain in the sand (s5060) and PVC (o5565) for the Partial-Fill and 10/16 test. Blue band is the period of no flow. Red dashed line is zero outside strain. Black dashed line is zero inside strain.

Compression occurs in the upper outside strain sensor throughout injection reaching approximately 3 με (Figure 85). This is reversed during drainage.

INFILTRATION

Infiltration tests were conducted to simulate possible rainfall events (however, the rates of infiltration are much higher than in most natural settings). A showerhead sprinkles water onto the surface of the column. This showerhead is supported over the top of the column by the frame. A section of the showerhead is blocked off to protect the optical fiber tape from being directly rained on. Some of the sand at the top of the column has been removed to where there is a 2.5 cm gap between the top of the sand and the top of the PVC column. A protecting layer of separation gravel is place on top of the sand that's only a couple grains deep. This helps protect the sand from gouging from the infiltrating water.

These tests had two different set ups and various infiltration rates. The first set up involved closing the drain at the bottom of the column, allowing it to completely fill up during infiltration. The other set up features an open drain where water continuously flows out of the column.

Infiltration Fill-Up test

An infiltration test was conducted with a closed drain to fill up the column. Infiltration was stopped after a 2.5 cm pond was formed. Ten minutes after filling, the column is drained using gravity.

Results

Pore Pressure

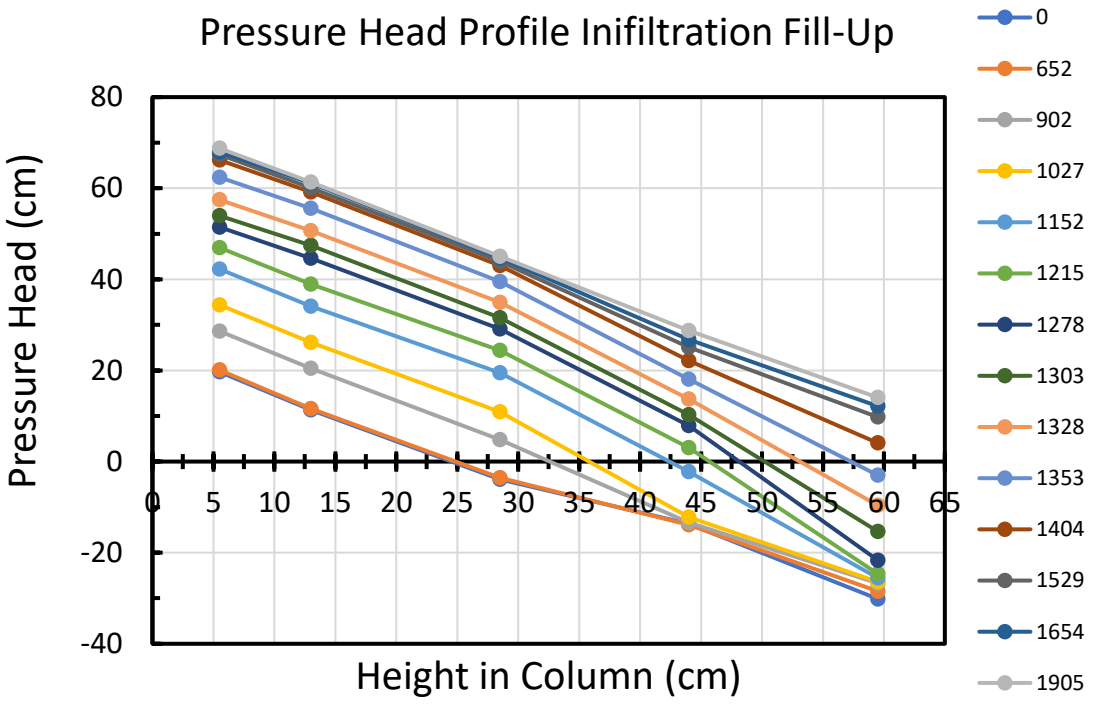

Figure 86: Pore pressure head profile for the infiltration fill-up test.

The infiltration rate during this test was 0.1 liters/min. This rate was lower than the rate of uptake in the sand, preventing the formation of a pond until the PZP reached the surface. The p60 tensiometer shows slight increase in pressure at time 450 seconds due to wetting from water flowing thought the column. The bottom three pressure sensors begin increasing around 675 seconds. This corresponds to the wetting front reaching the static PZP which then begins increasing in height. The pressure increases at a rate of 6.5 Pa/s. Around 1,050 seconds p44 begins increasing at the same rate as the lower three. The pressure gradient during infiltration is roughly 1.05. This is lower than the injection tests. As the PZP reaches the top of the column, the pressure begins to increase more

rapidly as the wetting front reaches the top of the column. Infiltration continues until a pond 2.5 cm deep forms. When the pump is shut off and infiltration stops, the bottom 3 pressure sensors stabilize but the top two slightly increase. The pressure heads approach the same value of 74 cm.

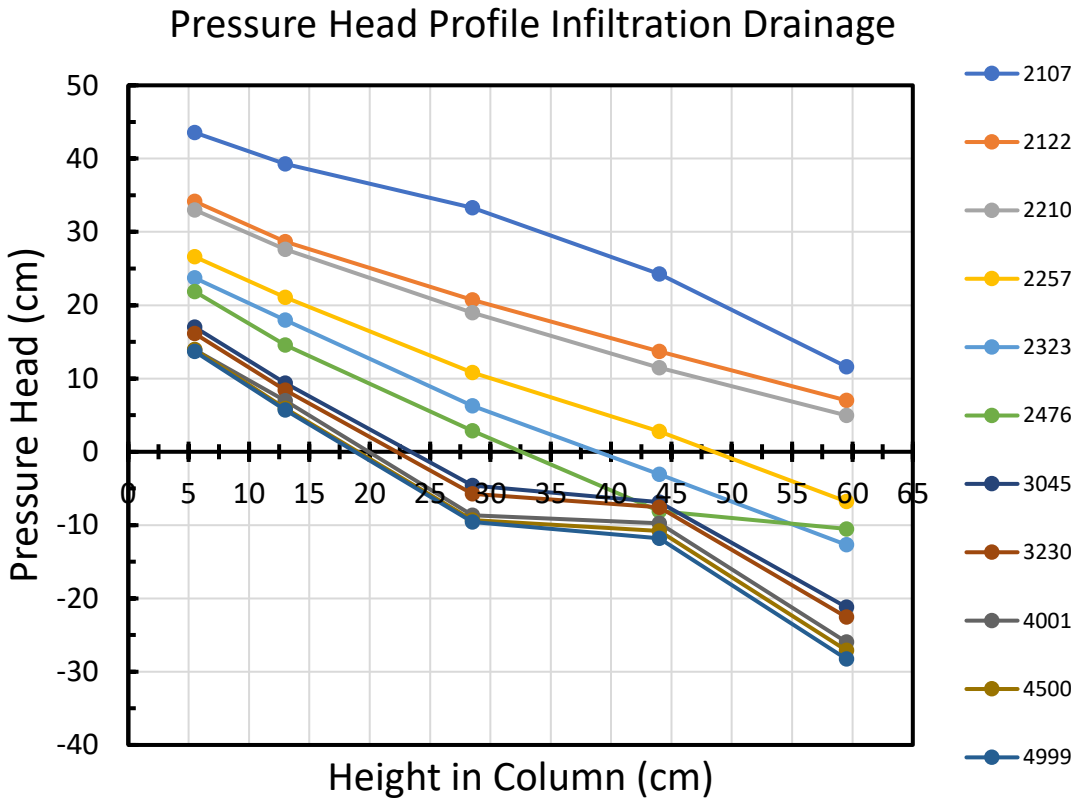

Figure 87: Pore pressure head profile for the drainage portion of the infiltration fill-up test.

After the infiltration, the drain is opened, and the column drains under gravity. The pond is deeper in this test than the other tests. While the pond drains, the pressure head forms a gradient of 1.77. Once the pond is drained the pore pressure responds similarly to the other gravity drainage tests.

Strain

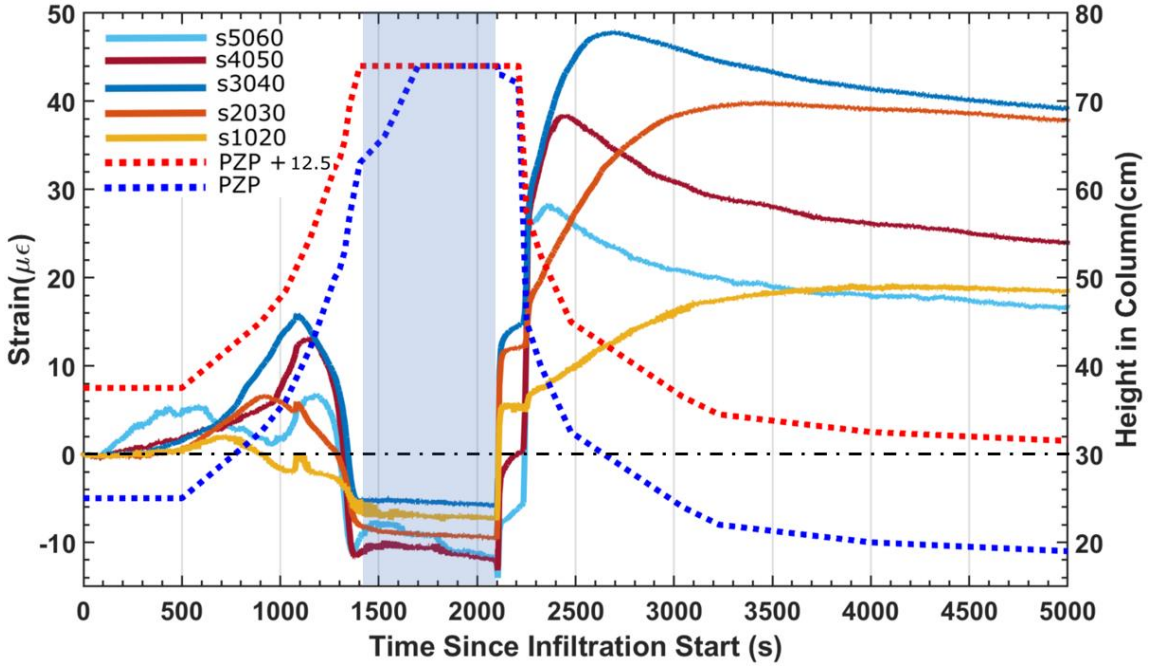

Figure 88: Strain and transition zone (PZP to PZP + 12.5 cm) height as functions of time for the infiltration fill-up test. Blue band is the period of no-flow.

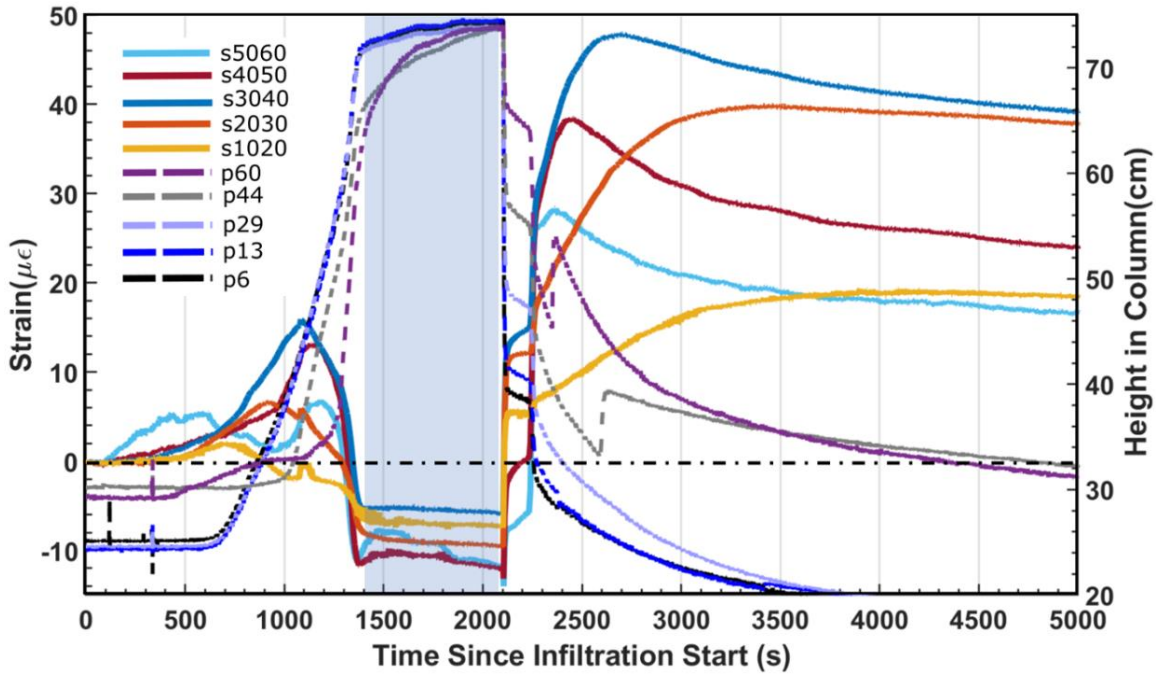

Figure 89: Strain and total head as functions of time for the infiltration fill-up test. Blue band is the period of no-flow.

The filling up of the column during infiltration produces a somewhat similar response to filling the column up during injection. Tensioning occurs as the wetting front from infiltration moves down the column. s5060 tensions the most during this period (upwards of 5 mu/s). The lower sensors increase more gradually. The rate of tensioning increases when the infiltrating front reaches the PZP causing it to rise. The strain reaches a maximum and begins compressing once the PZP reaches the top reflector (+/- 5 cm). The effect of ponding causes the rapid compression seen in the injection tests. After infiltration is stopped, the strain stabilizes and changes little until drainage begins.

After the infiltration, the drain is opened, and the column drains under gravity. Similar to other tests, starting drainage coincides with rapid initial tensioning. A period of stability occurs as the pond drains. This effect occurs for a longer time period due to a

deeper pond than in the injection tests. Once the pond is drained tensioning occurs similarly to the other tests involving gravity drainage with tensioning followed by compression as the transition zone through the column.

Strain in the Column

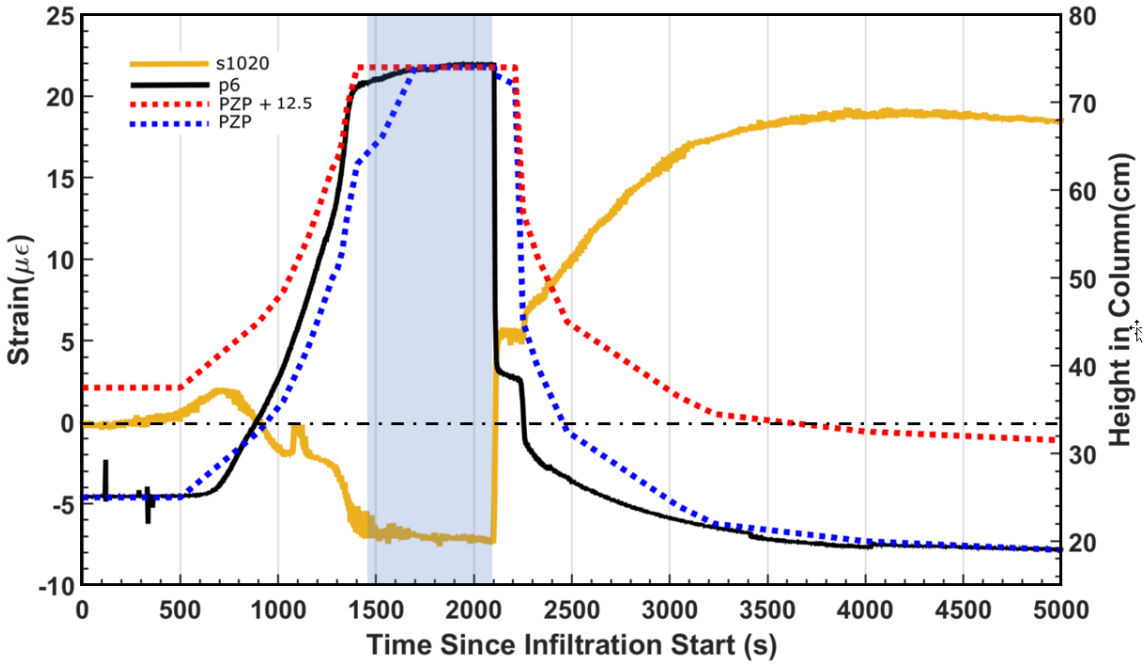

Figure 90: Strain at s1020, total head at p6, and transition zone (PZP to PZP + 12.5 cm) height as functions of time for the infiltration fill-up test. Blue band is the period of no-flow. Height or pressure head right axis label.

The s1020 sensor initially begins to tension at the time when the PZP begins increasing. After this point, it compresses until the formation of the pond. Little change occurs during the no flow region. Opening the drain coincides with approximately 15 με of tension. Little change occurs after this as the pond drains. After this, the sensor tensions similar to other gravity drainage tests.

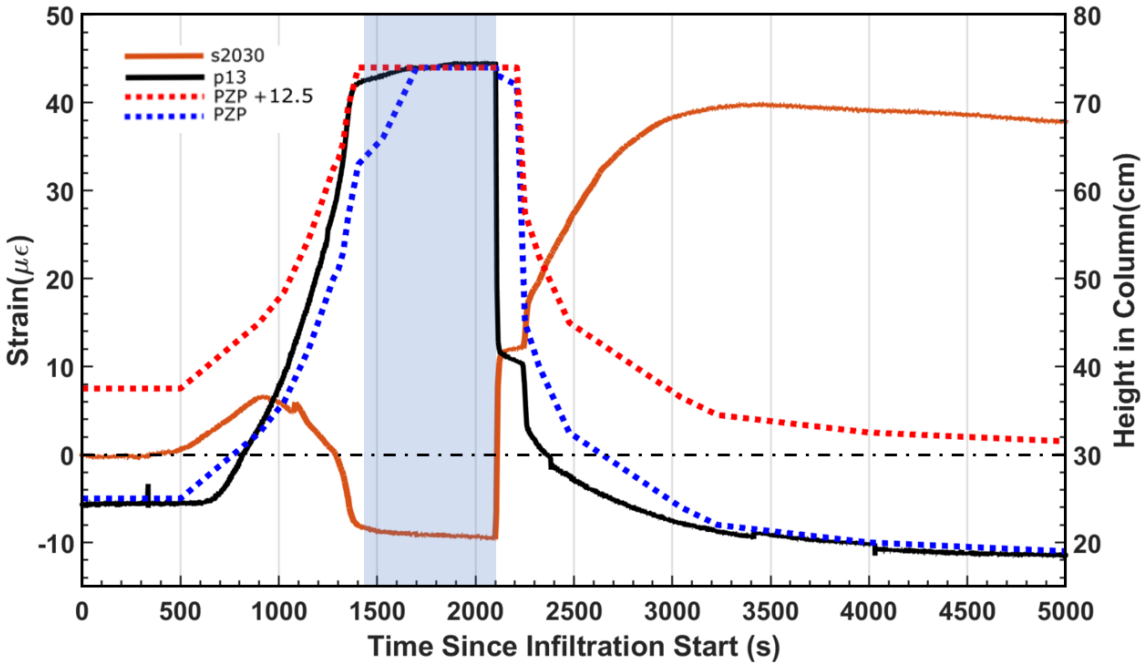

Figure 91: Strain at s2030, total head at p13, and transition zone (PZP to PZP + 12.5 cm) height as functions of time for the infiltration fill-up test. Blue band is the period of no-flow. Height or pressure head right axis label

The s2030 sensor begins increasing around the time the PZP starts increasing. It then begins compressing which continues until ponding occurs. Little change occurs during the no flow point. Opening the drain coincides with approximately 20 με of tension. Little change occurs after this while the pond drains. After this the response is similar to other gravity drainage tests.

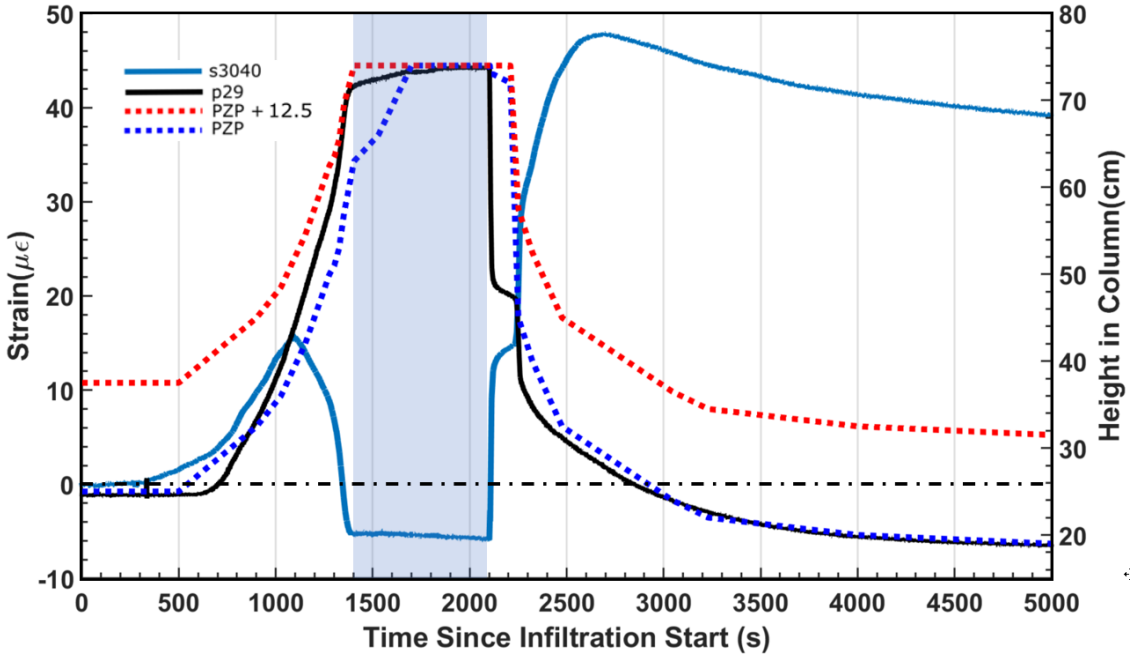

Figure 92: Strain at s3040, total head at p29, and transition zone (PZP to PZP + 12.5 cm) height as functions of time for the infiltration fill-up test. Blue band is the period of no-flow.

The s3040 sensor begins tensioning before the infiltrating water reaches the PZP causing it to increase in height. After a point, the sensor begins compressing. Ponding causes a larger rate of compression. Little change occurs during the no flow point. Opening the drain coincides with 20 με of tensioning. 2 με of tensioning occur while the pond drains. The response after this is similar to other gravity drainage tests.

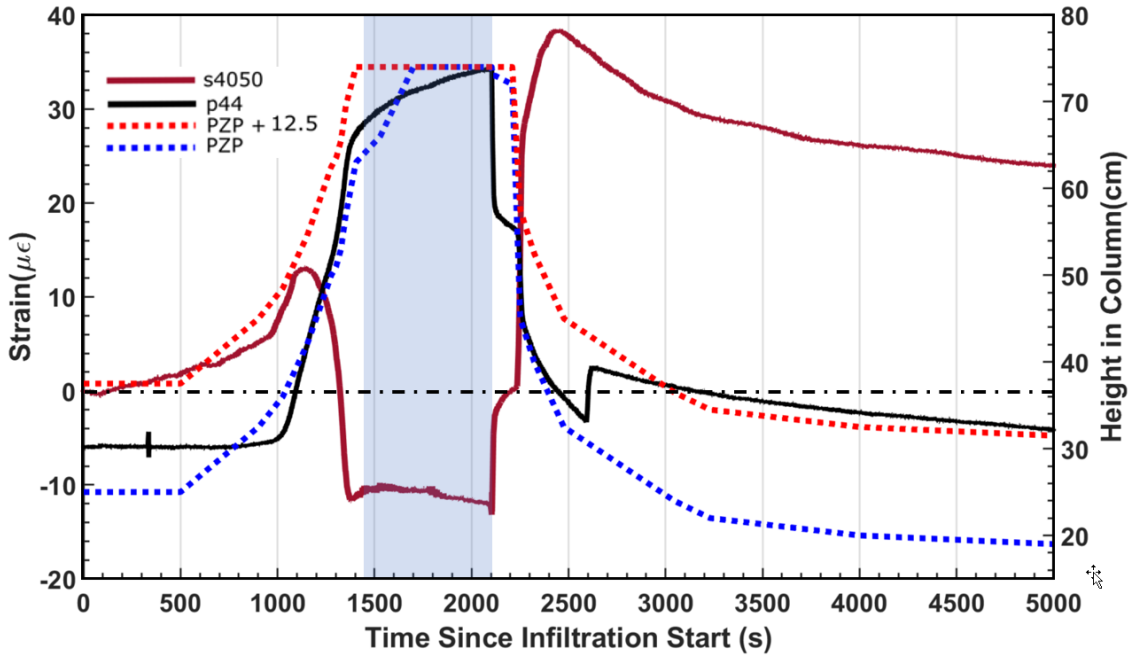

Figure 93: Strain at s4050, total head at p44, and transition zone (PZP to PZP + 12.5 cm) height as functions of time for the infiltration fill-up test. Blue band is the period of no-flow.

The s4050 sensor begins tensioning well before the wetting front reaches the PZP. Tensioning occurs more quickly at around t =1,000 s. Pond formation causes compression. Little change occurs during the do flow period. Opening the drain coincides with approximately 10 με of tensioning. Approximately 5 με of tensioning occurs while the pond drains. After complete drainage of the pond, the response is similar to other gravity drainage tests.

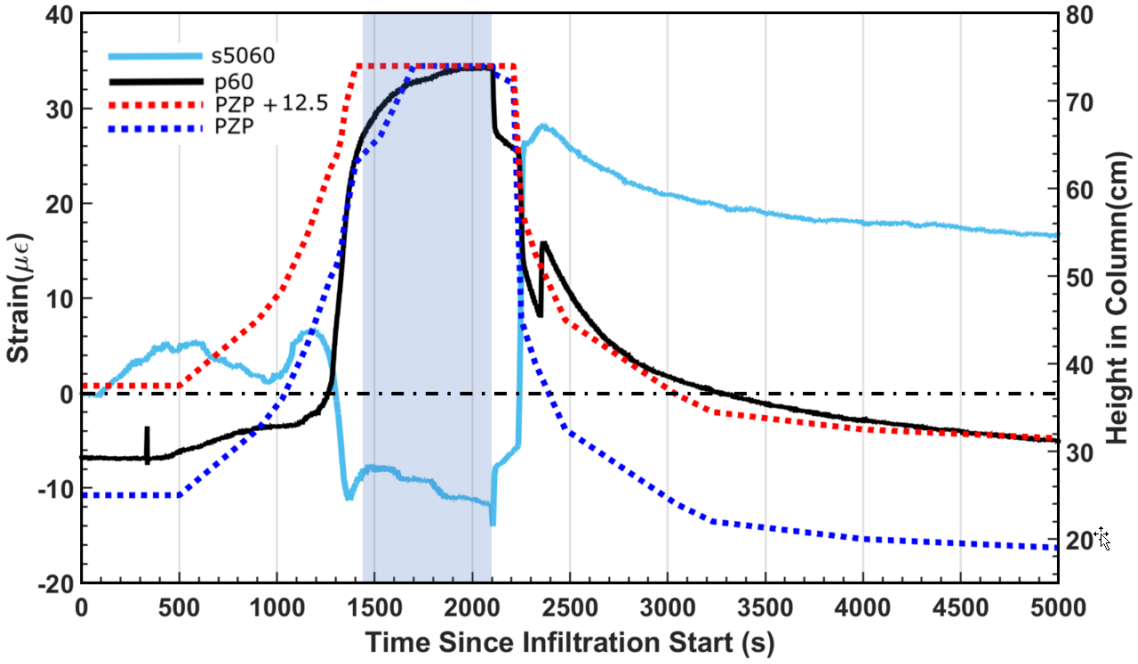

Figure 94: Strain at s5060, total head at p60, and transition zone (PZP to PZP + 12.5 cm) height as functions of time for the infiltration fill-up test. Blue band is the period of no-flow.

The strain at s5060 begins increasing at t =100 s and the pressure at p60 starts to increase slightly at t =400 s. The strain increases sharply at t =1,000 s and peaks at t =1150 s rounding off to compression. Ponding causes sharp compression as seen in other tests. Slight erratic change occurs during the no flow period. Opening the drain coincides with 5 με of tensioning. Another 5 με of tensioning happens as the pond drains. After complete drainage of the pond, the s5060 sensor responds similar to other gravity drainage tests.

Infiltration Open Drainage

Open drainage tests were conducted with various infiltration rates. These rates have varying effects on ponding. Ponding occurs when the rate of infiltration is greater

than the rate of uptake. Infiltration was conducted at a rate of 0.7 l/min. This is a high enough rate to create a pond on the surface.

Results High Rate

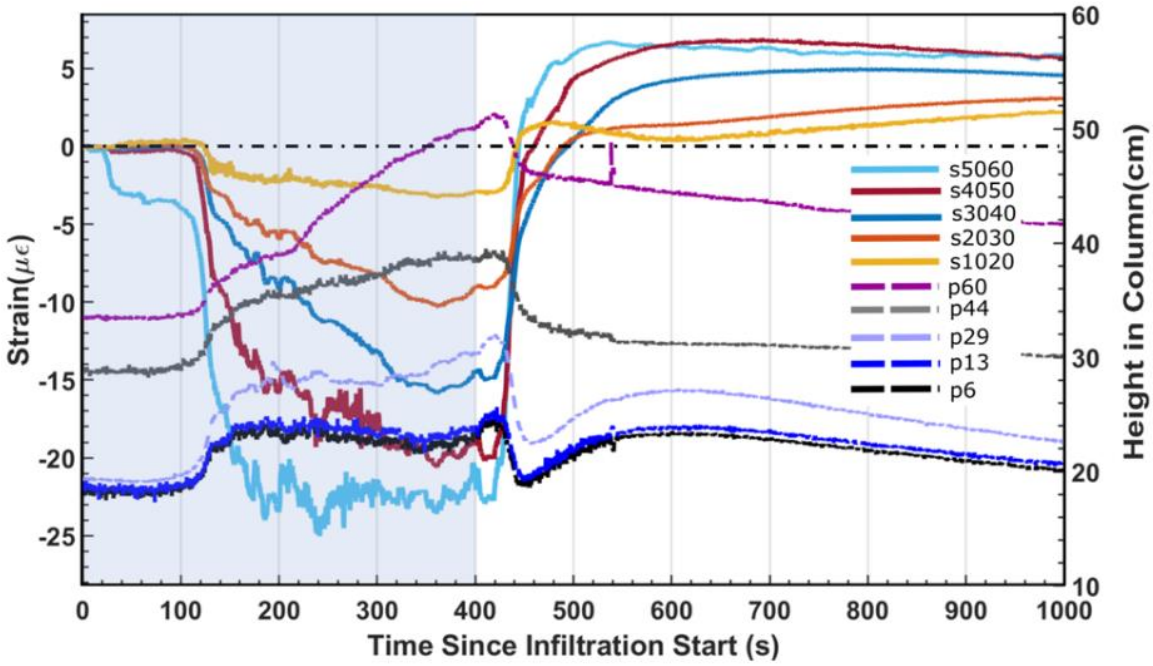

Figure 95: Infiltration test were the infiltration rate was greater than the uptake rate. This causes ponding on the surface. Strain and total head time series shown. Infiltration is on during the blue band.

Pore Pressure

Pressure jumps positively as soon as a pond is formed on the surface of the column. During the ponding, while infiltration is still on, pressures increase as water moves through the column. p60 increases the most with regions having a lower head. Pressure rapidly decreases after the pond sinks and completely goes away. After this drop, the pressure slowly increases as more water moves downward through the column.

Strain

s5060 compresses by 3 με 20 seconds after infiltration starts. Interestingly, ponding coincides with compression even when the rest of the column is unsaturated. Compression occurs when the uppermost grains of sand are completely saturated. This compression first happens at the top of the column and continues to the bottom. The compression is greatest in the upper regions of the column. When the infiltration is turned off, the pond drains. When the pond fully drains and the water moves beyond the top grains, tensioning occurs. Sharp tensioning happens throughout the column. The amount of tensioning increases with height in the column with the strain approaching between 0 and 5 με above pre-infiltration values.

Results Lower Rate

An infiltration scenario was created where ponding occurs and but due to the infiltration rate 0.35 l/min and drainage rate reach an equilibrium and the PZP forms at 30 cm.

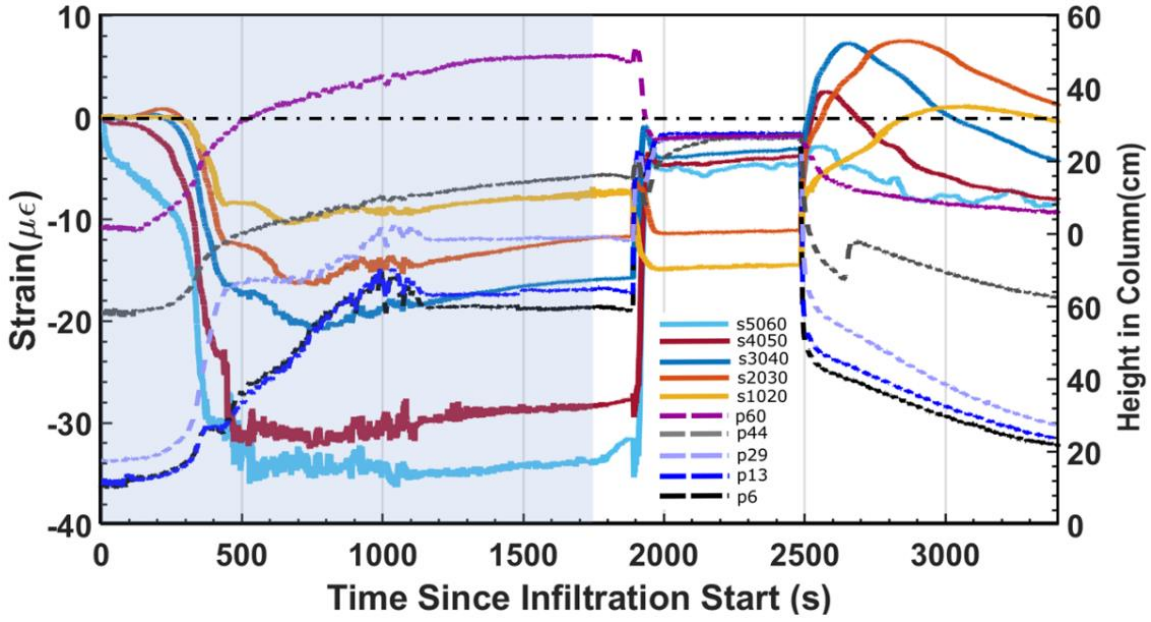

Figure 96: Strain and total head time series. This test had a lower infiltration rate but high enough to cause ponding. Drainage was stopped and restarted during the test. Infiltration is on during the blue band.

Pore Pressure

Pressure begins to increase 100 seconds after infiltration starts. The pressure increases to a point and then stabilizes. At time 1,750 s the infiltration is stopped. 150 seconds later the pond fully drains. After 10 seconds drainage is stopped. This causes the pressure to stabilize at the same value throughout the column. At 2,500 seconds the drain is opened again, and the drainage is similar to other gravity drainage situations.

Strain

s5060 is compressed by 4 με/s almost immediately following the start of infiltration. s4050 is compressed more gradually shortly after infiltration starts. s3040 compresses later and even more gradually. s2030 and s1020 compress begin compressing

at roughly the same time when the pond forms. The formation of the pond compresses all sensors in the column.

s5060 begins tensioning slightly when infiltration is shut off. When the pond fully drains, all sensors tension. The tensioning is cut off when drainage is stopped. When drainage is resumed, the strain behaves similar to other gravity drainage tests with the exception of s5060, which is most likely due to the PZP already being below it.

Breaking the drainage of the column into two events illustrates that two separate events cause tensioning in the column. First, opening the drain causes an initial shock to the system with a pressure wave propagating up the column. This causes the initial tensioning.

.

SEPARATION OF EFFECTS AND COMMONALITIES

The infiltration experiments allow for some of the effects seen in the injection tests to be separated and further studied.

Ponding during infiltration corresponds to compression throughout the column. This occurs in both infiltration conditions where the wetting front rises from below, and where the infiltration rate is high enough to form a pond on top of an unsaturated column. The pattern of the magnitude of compression decreasing with depth in the column also occurs with s5060 compressing the most and s1020 compressing the least.

The drainage of the pond corresponds with tensioning throughout the column. In the Infiltration-Fill up test, two separate tensioning events are seen. One corresponding with the drain opening, and one corresponding with the pond being fully drained. In the other infiltration tests, immediate tensioning occurred as soon as the pond was drained.

The drainage curves of the Infiltration-Fill Up and the Lower rate infiltration Open Drain test follows the same pattern as the injection tests drained using gravity.

CHAPTER SIX: CONCEPTUAL MODEL

The experimental observations can be integrated to a conceptual model that provides some insight into processes affecting strain during changes in saturation. Basic mechanics indicates that increasing pore pressure displaces grains of sand away from each other, reducing effective stress and causing tension. Decreasing the pressure has the opposite effect as the sand grains move closer to each other, causing compression. This concept is expressed in Hooke's Law, where vertical strain is given under uniaxial conditions as

$$\varepsilon_{zz} = C_u(\sigma_{zz} + \alpha p) \tag{31}$$

where σ_{zz} is the total vertical stress, α is the Biot-Willis coefficient, and

$$C_u = \frac{(1-2\nu)(1+\nu)}{(1-\nu)E} \tag{32}$$

with ν is Poisson's ratio and E is Young's modulus. Uniaxial strain means the horizontal strain is zero, which could be approximated by the relatively stiff tube used constrain the sand in the column. Assuming that the total vertical stress remains constant, it is apparent that the pressure compliance is

$$\frac{\partial \varepsilon_{zz}}{\partial p} = \frac{\alpha(1-2\nu)(1+\nu)}{(1-\nu)E} \tag{33}$$

In the experiments, $\alpha = 1$ and $0.25<\nu<0.45$, and 10MPa < *E* < 40MPa. This indicates that the strain increases (becomes more tensile) when the pressure increases, which is

consistent with the concept outlined above. It also shows that the expected pressure compliance is in the range $0.006\frac{\mu\varepsilon}{Pa} < \frac{\partial \varepsilon_{zz}}{\partial p} < 0.08\frac{\mu\varepsilon}{Pa}$.

Another important effect that can cause strain is related to the observation that the stress change in one area is transferred to another area in order to maintain equilibrium (Wang, 2000). For example, when the far-field stress remains constant, a stress increase in one area will decrease the stress in the neighboring region in order to maintain equilibrium with the far-field stress. So, an increase in pressure that causes local tensile strain and expansion in the pressurized area can result in compression in a neighboring region. This non-local strain can itself cause a change in pressure. An example of this effect is the pressure increase in confining units that occurs when pumping causes pressure to drop in an underlying aquifer, a process called the Noordbergum effect (summary in Wang, 2000; 218-221). A similar effect can cause a pressure reversal during injection into a single fracture (Murdoch and Germanovich, 2013). Pressurizing a borehole in tight rocks causes the pressure to decrease as a result of this stress transfer effect (Wang, 2000, Fig 8.8).

A third effect that can cause strain is a changing load on the boundary. Increasing the total stress normal to the free surface will increase the strain within the sand. The total stress is the sum of the effective stress and the pore pressure, so changing the pore pressure at the boundary will change the boundary condition and create strain within the sand.

These considerations identify three effects:

Hooke's law effect: strain is proportional to the local change in pressure, so the pressure compliance is positive.

Stress transfer effect: strain is caused by stress transfer from a neighboring region, so the strain can be independent of the local change in pressure. The pressure compliance can be zero or negative in this case.

Boundary load effect: Strain is a result of changes in the load applied to a boundary. Strain can be independent of the local pressure.

Several aspects of the experiments complicate interpretation of the results. All of the important parameters (Young's modulus, Poisson's ratio, permeability, effective Biot-Willis parameter) are non-linear functions of saturation. This may cause basic inferences to differ from expectations. Moreover, the experiments were conducted inside a tube that is more rigid than the sand used in the experiment. This will tend to make the deformation uniaxial, which simplifies interpretations, but friction on the wall of the column will introduce effects that may be difficult to anticipate.

The conceptual model will be described using both Stages in time and Zones in space. A representative set of reflectors are assumed to be in the middle of the column, and Stages are identified based on characteristic changes in the strain time-series associated with the sensing region between those reflectors. Zones are identified based on the characteristics of the pore pressure distribution (Ambient Zone, Transition Zone, Positive Pressure Zone).

INJECTION STAGES

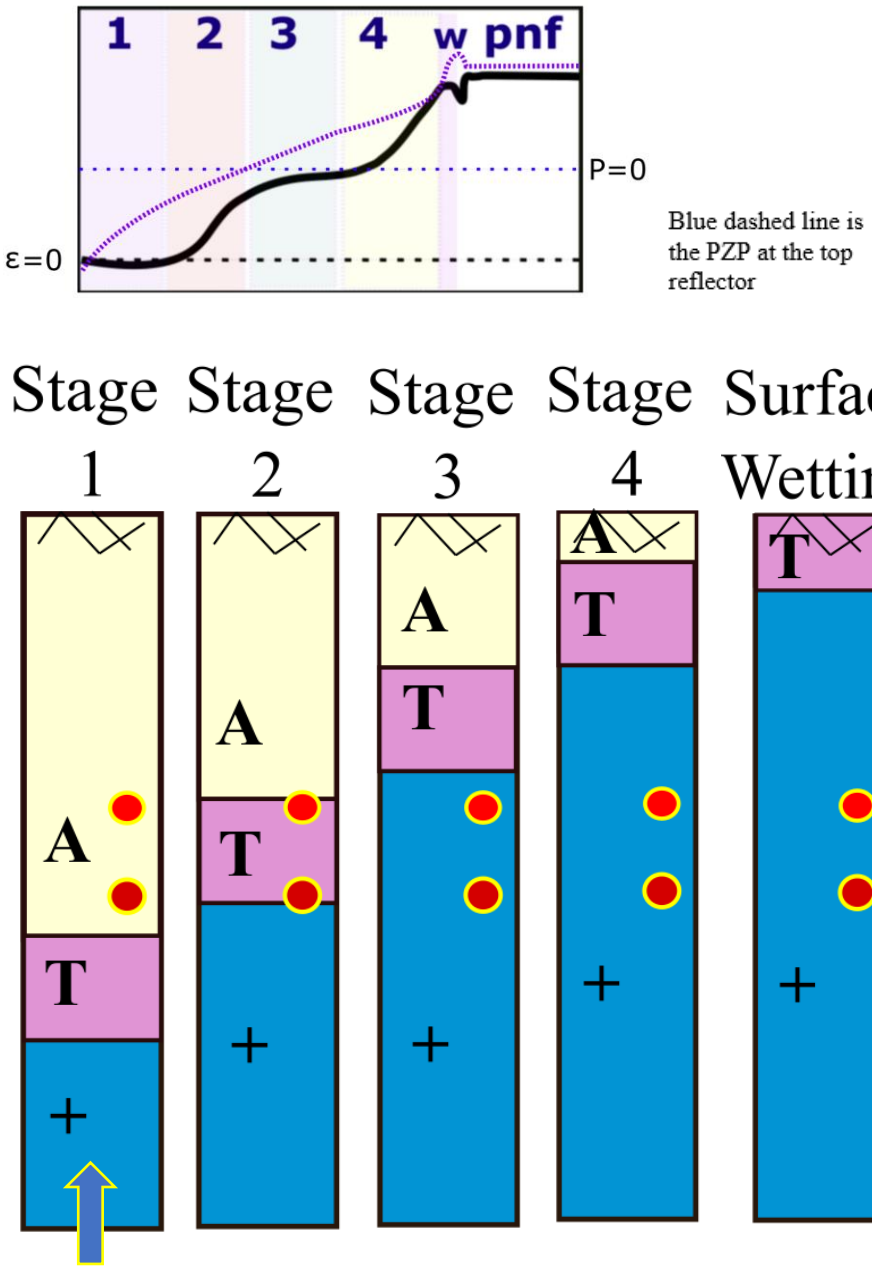

Figure 97: Strain time-series with stages (labeled colors) and sketches of different stages (Ambient, Transition, and Positive pressure (+)) in the column during injection. Red dots are a representative strain sensor. P=0 is for the top of the reflector.

Stage One

Stage One starts with the strain in the sensing region at ambient conditions. The strain then becomes negative (compression) reaching several με of compressive strain before the strain starts to increase. For example, s4050 and s5060 in Figure 74 and Figure 76 (Figure 34 and 59). This stage is absent from sensors below the transition zone at the start of the test (e.g. s1020 and s2030 in Figure 68 and Figure 70).

The pressure transition zone underlies the strain sensing region throughout Stage One, but the increase in strain that marks the end of the Stage occurs as the leading edge of the pressure transition zone arrives at the lower reflector (Figure 98). Strain appears to be unaffected by the rising pressure when the transition zone is significantly below the sensing region, but the region is compressed as the transition zone approaches. This appears to be a strain transfer effect from expansion in the advancing underlying transition zone. The rate of compression during Stage One is roughly half the rate of expansion in the underlying transition zone, but this may be because the elastic modulus in the relatively dry sand under ambient saturation is stiffer than under the more saturated conditions in the transition zone. The pressure compliance during Stage One is zero or negative. This is consistent with strain caused by the stress transfer effect.

Stage Two

The beginning of Stage Two is marked by an increase in strain that continues until the strain is increasing at a roughly constant rate of approximately 0.02 με/s. The slope flattens and goes to approximately zero at the end of the stage.

The pore pressure is negative at the start of this stage and it increases first at the bottom of the interval between the reflectors and then throughout the interval. The pressure head reaches zero at the bottom reflector at approximately the end of Stage Two. The rate of pressure head change ranges from 0.025cm/s at the lower transducers (p6, p13, p29) to 0.08 cm/s in the upper two transducers (p44 and p60 in Figure 59). The upper two transducers appear to represent far-field conditions at the start of the tests, whereas the lower ones may be influenced by the initial position of the transition and positive pressure zones. As a result, the relatively rapid pressure increase measured at the upper two transducers is inferred to be representative of Stage Two.

Stage Two appears to be controlled by the location of the pressure transition zone. The PZP+ 12.5 (top of transition zone) is approximately at the level of the bottom reflector at the start of Stage Two (e.g. Figure 66). The PZP(bottom of the transition zone) is approximately at the level of the top reflector at the end of the end of Stage Two. The duration of Stage Two is approximately 800s. The velocity of the water is approximately 0.027 cm/s, the transition zone is 12 cm high and the spacing between the reflectors is 10 cm. As a result, the time for the transition zone to transit the sensing interval is 22cm/0.027 cm/s =814 s, which is consistent with the observed duration of the Stage Two.

The vertical pressure head gradient in the transition zone is approximately 2 to 2.5, according to the data. This is the steepest pressure head gradient of the three pressure zones. The gradient is approximately 1.2 in the positive pressure zone and 1.0 in the ambient zone. The rate of injection is constant, so the steep pressure gradient in the

transition zone caused the rate of pressure increase during Stage Two to be several times faster than during the other Stages; the rate of change of pressure head is approximately 0.08 cm/s in Stage Two and it drops to 0.025 cm/s in Stage Three.

The pressure compliance determined from the ratio of the strain and pressurization rates is 0.01 με/Pa, and it ranges from 0.05 to 0.02 (e.g. slopes of the lines in Figure 79 and 80). This is in the range expected for strain caused by a pressure increase, as calculated above.

Stage Three

This stage begins with the slowing of the strain rate and continues until the rate is essentially zero, and in some cases the rate drops to negative values (Figure 59). The Stage ends in the records from the upper sensors when the pump is turned off, but strain in the lower two sensors increases prior to turning off the pump. As a result, we infer that a significant increase in strain marks the end of Stage Three (Figure 97). This indicates that the duration of Stage Three is 500s to 700s (Figures 59 and 60). It follows that this increase in strain would have occurred in the upper sensors if the duration of pumping was longer.

The pore pressure is positive in this stage and the pressure head is increasing at a rate of approximately 0.025cm/s (2.5 Pa/s). The sand is saturated and the pressure gradient is uniform and approximately 1.2. The PZP is approximately at the upper reflector at the beginning of this Stage and it is 13 to 19 cm above the upper reflector at the end of the Stage.

The pressure compliance decreases to zero and becomes negative in Stage Three. This is inconsistent with strain caused be a local pressure change. It is consistent, however, with compression caused by stress transfer from the expansion in the overlying pressure transition zone. Although the pressurization rate is positive during Stage Two, it is roughly one third of the rate of pressurization that occurs during Stage Two. This is a result of a flattening of the pressure head gradient by roughly half from Stage Two to Stage Three. The interpretation is that the expansion that occurs in the pressure transition zone is sufficient to counter the expansion that would have occurred due to the increasing pressure during Stage Three.

Stage Four

This Stage is marked by an increase in strain to 0.02 to 0.03 με/s, approximately the same rate that occurred during Stage Two. This stage only occurs in data from the lower sensors, s1020, s2030, and s3040 (Figure 68, Figure 70, and Figure 72). The pressure continues to increase at a rate of approximately 2.5 Pa/s, and the pressure gradient remains constant at 1.2. This implies that the pressure compliance is 0.008 to 0.012 με/Pa, which is in the expected range for strain change according to Hooke's Law.

It appears that the process causing strain has returned to the same process as during Stage Two. The PZP and transition zone are more than 20 cm above the upper reflector during Stage Four.

One explanation for this behavior is that expansion in the transition zone compresses the sand above and below it. This effect causes compression observed during

Stages One and Three. The effect diminishes with distance, however, and it appears to be negligible beyond 20 cm below the PZP where the sand expands in proportion to the increasing pressure.

Surface Wetting Stage (w)

Interaction with the free surface begins with a decrease in the slope of the strain time series that marks the beginning of the Surface Wetting Stage, Stage *w* in Figure 97. The slope decreases and the rate drops as low as -0.7 με/s, as the strain becomes increasingly compressive. The magnitude of the compressive strain is greatest near the free surface where it is up to 30 με more compressive than the initial conditions (it drops from 10 με to -30 με). The rates and final magnitude diminish with depth, however, and the strain at s2030 drops by only a few με and the change is negligible at s1020. The negative slope abruptly flattens, and the strain is essentially constant by the time the pump is turned off to mark the end of the Stage Four (Figure 76 and Figure 68).

The pressurization rate increases from 2.5 Pa/s during Stage Four to a maximum of 25Pa/s during the Surface Wetting Stage. The maximum pressurization rate coincides with the largest negative strain rate. The pressurization rate diminishes and drops back to the original rate of 2.5 Pa/s as the strain rate drops to zero at the end of the Stage. The change in slope produces a sigmoidal pattern where approximately 1000 Pa of pressure is gained relative to projected pressure change caused by filling the column with water. This anomalous increase in pressure is roughly independent of depth, unlike the magnitude of the strain change, which decreases with depth.

The appearance of the surface of the sand changes through this stage, initially darkening as the moisture content increases first in the lowest areas. The moisture content continues to increase through the period of increasing pressurization rate and diminishing strain rate. The inflection in these curves appears to coincide with the development of free water ponding on the sand. The rates of both the pressure and strain diminish as the extent of ponding expands and the rates drop to essentially zero when free water covers the full sand surface.

The location of the PZP can be extrapolated from measurements at the p60 pressure sensor, and this indicates that the beginning of the Surface Wetting Stage occurs when the PZP+12.5 point reaches the free surface of the sand. The appearance of free water at the surface of the sand occurs approximately when the PZP reaches the free surface.

The effects observed in the Surface Wetting Stage appear to be a result of interactions between the pressure transition zone and the free surface of the sand. The change in appearance of the surface of the sand is a result of increasing moisture content that occurs as the transition zone moves upward. Even though the moisture content increases at the surface, flow of water out onto the surface of the sand is inhibited for most of this Stage. This causes the pressure to increase up to 10x faster that it would have otherwise increased.

The increase in pressure and the large decrease in strain that occur during the Surface Wetting stage occurred in all tests where then the rise in the water level was sufficient to cause ponding. These effects are absent from the Partial Fill test where

ponding did not occur. This is strong evidence that these effects are a result of interactions between the pressure transition zone and the free surface.

Capillary exclusion was originally recognized by Philip & Knight, (1989) as a process where water in unsaturated soil is prevented from entering a buried cavity, like a macropore, cave or tunnel. The water is excluded from entering the cavity so long as the water pressure is less than atmospheric pressure. Capillary exclusion of downward flowing water has received considerable attention because it explains the conditions required for water to flow across the free surface of a cavity in the vadose zone. Capillary exclusion will also occur when upward flowing water encounters a free surface, as in the experiments. Extrapolating pressure data measured at p60 indicates that the PZP reaches the sand surface at approximately the same time free water was observed accumulating at the surface. This is consistent with expectations from the capillary exclusion effect. The observed excess increase in pressure of approximately 1000 Pa appears to be a consequence of capillary exclusion.

Mechanical processes associated with capillary exclusion are poorly known, but they can be inferred from the experimental observations. The pressure compliance during surface wetting is negative, roughly -0.028 με/Pa, ruling out the possibility that the strain is a result of local pressure changes. It is also unlikely that strain transfer is an explanation because there is no indication of a region undergoing the rapid expansion that would be needed to explain the observed rapid compression. The observed strain behaves as if a compressive stress is applied at the upper boundary. The effects of a

boundary load would diminish with depth as a result of friction along the wall of the column, as was observed in the loading tests (Figure 22).

One possibility is the boundary load is related to the change in pressure that occurs due to capillary exclusion. The magnitude of the pressure increase is approximately 1000 Pa. Assuming this pressure is applied downward at the surface, this would cause strain of approximately $\varepsilon_{zz} = C_u 1000Pa$. C_u depends on E and ν for saturated conditions. Assuming E=18MPa and ν=0.35 in eq. gives $C_u = 3.5 \times 10^{-8}$ Pa^{-1}. This indicates that the expected strain is $3.5 \times 10^{-5} = 35$ με. Approximately 40 με of compression was observed at the upper strain sensor, s5060 (Figure 58). As a result, the boundary load hypothesis appears to explain the magnitude of the compressive strain observed during the Surface Wetting Stage.

Ponded No-Flow

The strain rate goes to essentially zero when free water covers the top of the column (ponding), and turning off the pump causes slight, but immediate tensioning throughout the column. Strain and pressure stabilize during the Ponded No-Flow stage. The pressure head gradient collapses to 1.

DRAINAGE STAGES

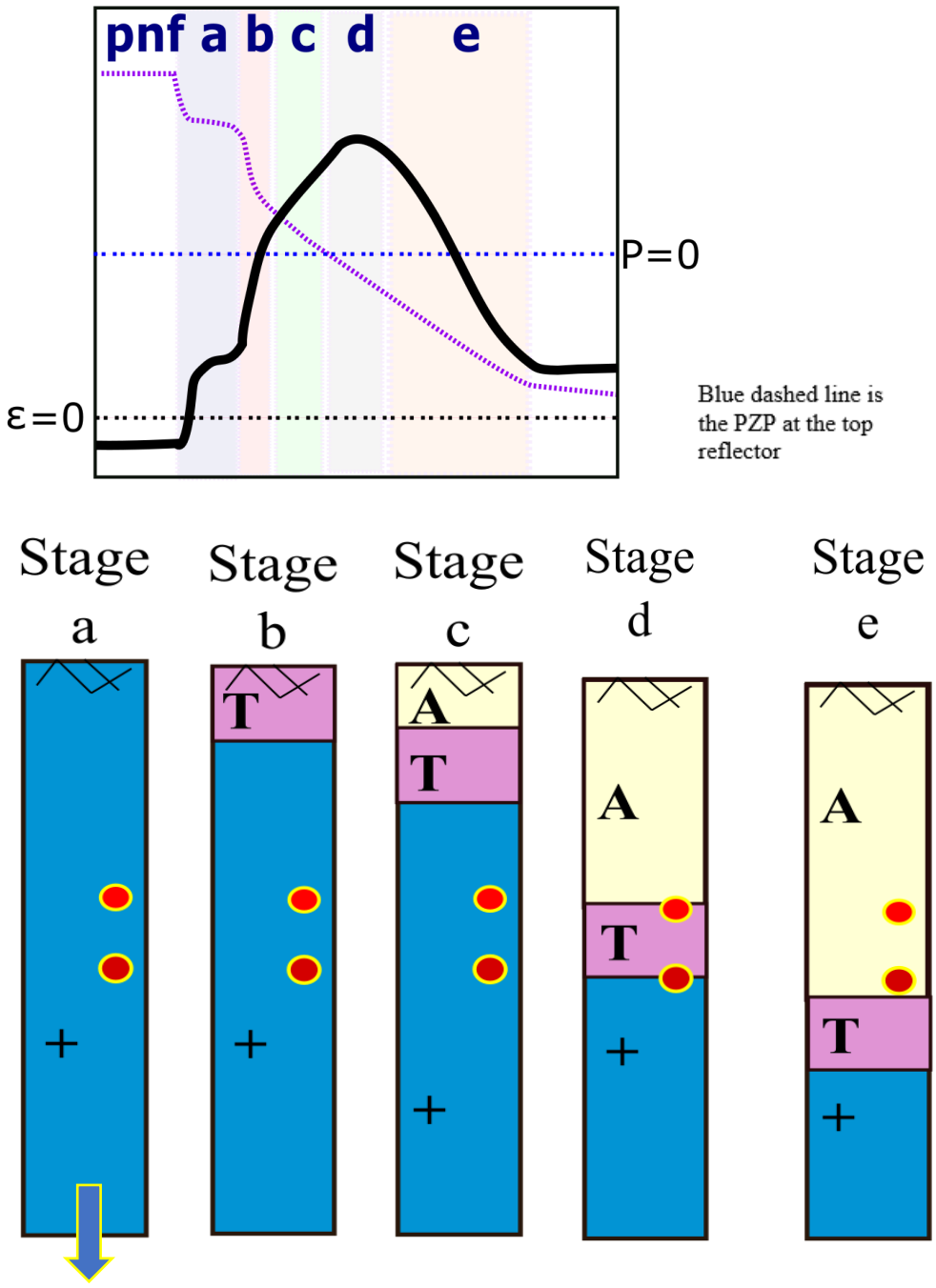

Figure 98: Strain time-series with stages (labeled colors) and sketches of different stages (Ambient, Transition, and Positive pressure (+)) in the column during drainage. Red dots are a representative strain sensor.

DRAINAGE STAGES

Drainage occurs when water is removed from the bottom of the column, either by pumping or by opening a valve and allowing gravity drainage. This process results in four stages, designated *a, b, c, d*, and defined by characteristics of the strain signal (Figure 98).

Stage *a*

The strain time series during the onset of drainage resembles a tangent function (sigmoid rotated by 90^{o}), with an initial rapid increase at the onset of drainage followed by a decrease in the rate and a subsequent increase. Stage *a* begins with the start of drainage and ends at the inflection point in the sigmoid. All of the experiments where Stage *a* occurred start with water ponded on the surface of the sand. The depth of the ponded water decreases when drainage starts, and the ponded water is completely drained from the surface at approximately the same time as the inflection in the strain signal. As a result, the end of Stage *a* is characterized by the inflection point in the strain signal, but that time was selected because it coincides with the drainage of the ponded water.

The shape of the strain time series when drainage occurs by pumping differs significantly from the shape when drainage occurs by gravity, although both shapes resemble tangent functions, and they share the characteristic that ponded water is depleted at the inflection point. The strain rate increases at the outset of drainage, but the rate is faster and the overall strain that occurs during gravity drainage (Figure 90) is larger than when draining by pumping (Figure 64).

The changes in pressure in the two experiments also have similarities and differences. In both the gravity drainage and the pumping cases, the pressure is sigmoidal with a rate that is initially steeply negative, flattens with time and then steepens. The pressure drops much faster at the start of gravity drainage (Figure 90) compared to the drainage by pumping (Figure 64). The hydraulic head measured at different locations along the column is uniform during the no-flow period and the head drops first at the bottom of the column when drainage starts. The head drops by approximately 10 cm at the start of pumping, but it drops by over 60 cm at the start of gravity drainage (the outflow tube was approximately 65 cm below the top of the initial water level). These differences in the head account for the differences in the strain between these two cases. Nevertheless, the cases share a sigmoidal shape with an inflection point that occurs when the ponded water drains from the surface of the sand.

The pressure compliance is negative throughout Stage *a* with tensile strain accompanying a drop in pressure. This effect is explained by a stress transfer that is related to inferred compressive strain at the bottom of the column. The pressure drop during drainage will be greatest at the bottom of the column, and this is inferred to cause negative strain (compression). This is similar to subsidence caused by reducing pressure in an aquifer. Negative strain at the bottom of the column would initially cause positive strain in the overlying sand. The rates and magnitudes of the strain increase with the rates and magnitudes of the pressure change, which accounts for the differences between the gravity and pumping cases. Friction between the sand and the wall of the column may increase the magnitude of the effect.

Stage *b*

Stage *b* starts with an increase in the strain rate following Stage *a* and it includes a period of rapidly increasing strain. The end of Stage *b* is marked by an abrupt decrease in the strain rate. The strain rate during Stage *b* is among the most rapid during the test. It reaches 0.9 με/s during the pump out (Figure 64) and it is even faster during gravity drainage (Figure 90). This fast strain rate persists for up to a few tens of seconds and results in tensile strain of up to tens of με. The tensile strain that occurs during Stage *b* is greater than the compression that occurs during the Surface Wetting stage.

The pressure drops rapidly during Stage *b,* reaching a rate of -0.3 cm/s (-30Pa/s) (Figure 64). Interestingly, this rate is similar to, but opposite in sign to the rate of pressure increase during the Surface Wetting stage. The PZP starts at the top and moves downward into the column during Stage *b*. The pressure is positive during Stage *b*.

Stage *b* shares some important similarities with the Surface Wetting stage. They both occur as the pressure at the surface of the column changes significantly. The pressure increases and approaches zero as the transition zone approaches the free surface during the Surface Wetting stage, and it starts at zero (when the ponded water drains) and decreases during Stage *b*. However, the pressure drop during Stage *b* is larger than the pressure increase during Surface Wetting (e.g. Figure 59). This difference in pressure change may explain why the strain increase during Stage *b* is greater than the decrease during the Surface Wetting stage.

The similarity between the Surface Wetting stage and Stage *b* implies that the capillary boundary load inferred to occur during the Surface Wetting stage also occurs during Stage *b*. This means that the sharp decrease in pressure that occurs at the surface of the sand behaves like a tensile boundary load.

Stage *c*

Stage *c* is marked by a rapid decrease in both the strain and pressure rates by approximately and order of magnitude. The strain rate drops to 0.07 με/s and the rate of change of the pressure head increases to -0.03 cm/s (-3Pa/s), and these rates are similar for the upper three sensors during the pump out test. These data lead to a pressure compliance of -0.23 με/Pa.

The pressure transition zone during filling (imbibition) is a region where the pressure increases rapidly and expansion occurs, but during drainage it is a region where the pressure drops and contraction occurs. The regions bordering the pressure transition zone appeared to experience compression during filling, and this is manifested by compression during Stage 1 and reduced extension to compression during Stage 3. A similar effect appears to occur during draining. In this case, the pressure transition zone undergoes contraction and this causes the region below it to expand.

As a result, the strain during Stage c appears to result from a stress transfer effect underlying the pressure transition zone. This is analogous to Stage 3 during filling.

Stage *d*

Stage d is characterized by a sharp decrease and a change in sign of the strain rate (Figure 98). The strain reaches a maximum value, which is roughly twice the maximum strain at the time when the column was filled with water.

The boundaries of Stage d are related to the location of the PZP. The stage begins when the PZP arrives at the upper reflector and it ends when the PZP reaches the lower reflector in the strain sensing interval.

The pressure decreases at approximately a steady rate of 0.02 Pa/s, which is typical of pumping conditions. As a result, the pressure compliance changes sign from negative to positive during Stage *d*.

The maximum strains occur at times that increase progressively with depth in the column. This is consistent with an effect that is associated with the location of the downward moving PZP.

The effects outlined for Stage d occur in tests that involve complete filling and ponding, as well as the Partial Fill test (Figure 34). This further supports the conclusion that this stage is controlled by the moving transition zone, and it demonstrates that the effects during this stage are independent of the extent to which the column is filled.

The data indicate that the stress transfer effect that was controlling strain during Stage *c* is also important at the beginning of Stage d. This changes however as the transition zone moves through the zone between the reflectors on the strain sensor. The Hooke's Law effect controls the strain at the end of Stage *d*.

Stage *e*

Both the pressure and the strain decrease during Stage e. The rates diminish with time. Stage e starts in the upper sensors sooner than in the lower sensors, so the rates at shallow depths are slower than at greater depth. The pressure compliance is similar at the different depths, even though the rates are different. For example, the strain rate at the lower sensors is -0.06 με/s when the pressure rate is -2.5 Pa/s at t = 3400s during the 10/16 tests, while the strain rate at the s5060 sensor is -0.02me/s and the pressure rate is -0.8 Pa/s. The pressure compliance is 0.025 με/Pa at both locations.

These results indicate that the strain during Stage *e* is consistent with Hooke's Law.

SUMMARY

Strain during the experiments appears to be controlled by effects associated with the pressure transition zone (Figure 99). During the imbibition that accompanies filling, the pressure is increasing in the transition zone and this causes it to expand while the regions above and below are compressed. This effect diminishes with depth and the strains are tensile in the region more than 20 cm below the transition zone when the

pressure is increasing. These effects explain Stages 1, 2, 3, and 4.

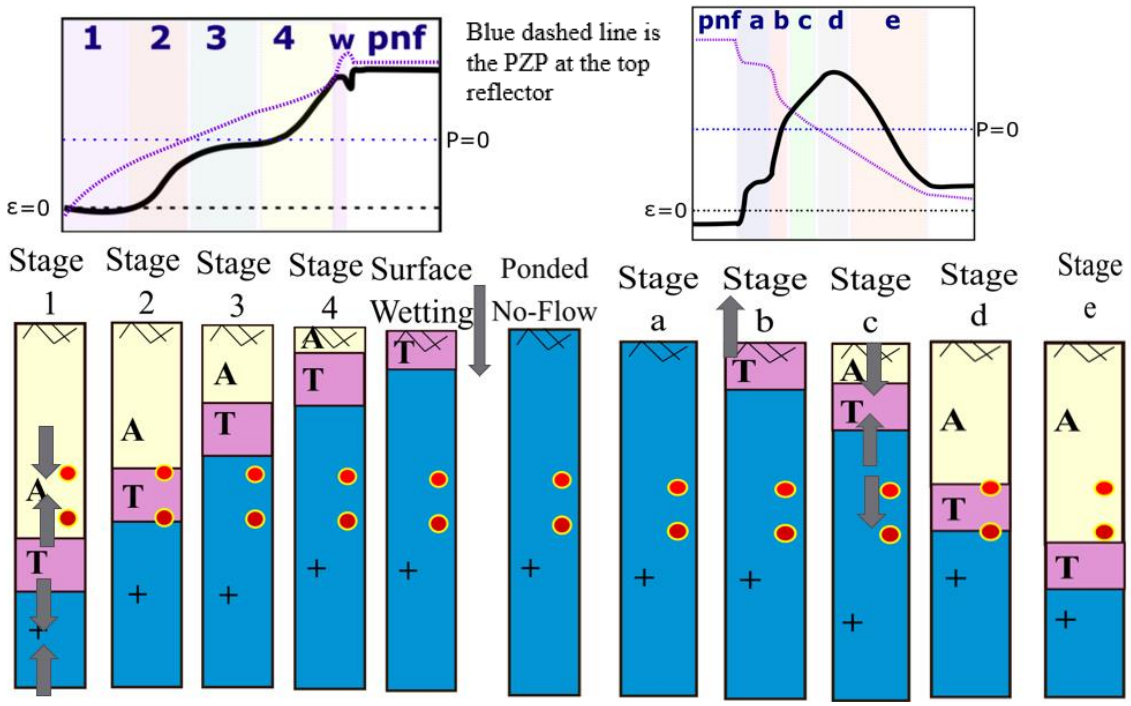

Figure 99: Graphical summary of strain and pressure events during imbibition and drainage. Grey arrows represent dilation or contraction.

Sharp changes occur as the pressure transition zone approaches the free surface. Capillary exclusion causes the pressure to increase. A capillary boundary effect that behaves like a compressive stress approximately equal to the change in pore pressure causes compressive strain that increases until the surface becomes saturated. The strain rate goes to zero and the pressurization rate slows significantly when the surface of the sand is fully covered in ponded water.

Strain during drainage controlled by the same effects as during filling. The strain is sensitive to draining of ponded water, and a sharp tension occurs when the pressure at the surface of the sand drops below zero. This is equivalent to the sharp increase in

compression as the transition zone reaches the surface during filling. The transition zone compresses during draining the causes expansion in the underlying sand. As a result, the downward moves transition zone causes tension as it approaches and compression when it arrives and passes a strain measurement location.

CHAPTER SEVEN: SUMMARY AND CONCLUSIONS

A new method of measuring strain in unconsolidated materials was developed and evaluated using laboratory experiments. The method uses 250 μm optical fiber laminated in a thin compliant ribbon of polyester film 2.5 cm wide. Reflectors on the optical fiber are interrogated using a novel strain sensing technique called CMPI. The strain ribbon is embedded in sand and coupled to strain in the sand through friction.

A strain ribbon with reflectors spaced every 10 cm was placed along the axis of a plastic cylinder filled with sand and instrumented with pressure and temperature sensors. Water was injected into the bottom of the sand-filled column and then drained while the pressure, temperature and strain were measured.

An initial suite of tests was conducted by placing weights on top of the sand and measuring the resulting strain. The results indicate that the strain is proportional to the applied load and the proportionality is generally consistent with the expected elastic properties of the sand. The strain in the sand decreases with depth, and strain can be measured in the wall of column. This suggests that some stress in the sand is transferred to the column.

A suite of tests was conducted where the column was filled until water ponded on the surface of the sand, and then it was drained. Another test was conducted where the column was partially filled with water, and additional tests were conducted where water was infiltrated from the top of the column.

The results show that the strain and pressure increase during filling and decrease during drainage of the column. The pressure occurs in three zones: an *ambient* zone where the pressure is unchanged from the initial conditions, a *pressure transition* zone where the pressure is greater than ambient but less than zero, and a *positive pressure* zone.

Although the records of strain distributed along the column generally increase during injection and decrease during drainage, details of these records are complex but generally repeatable. Some aspects of the records are repeated even during experiments that are quite different. Repeatability of the general pattern of strain indicates that the sensors are measuring a signal that reflects strain processes within the sand.

Eleven stages were identified in the strain signals and pressure signals of experiments where water completely filled the column. Stages 1,2,3,4, and *w* occur during filling, Stage pnf occurs when the injection pump is turned off, and Stages *a,b,c,d,e* occur during draining. Strain during these stages appears to be controlled by effects associated with the pressure transition zone. During the imbibition that accompanies filling, the pressure is increasing in the transition zone and this causes it to expand while the region above and below are compressed. This effect diminishes with depth and the strains are tensile in the region more than 20 cm below the transition zone when the pressure is increasing. These effects explain Stages 1, 2, 3, and 4.

Sharp changes occur as the pressure transition zone approaches the free surface. Capillary exclusion causes the pressure to increase. A capillary boundary effect that behaves like a compressive stress approximately equal to the change in pore pressure

causes compressive strain that increases until the surface becomes saturated. The strain rate goes to zero and the pressurization rate slows significantly when the surface of the sand is fully covered in ponded water.

Strain during drainage controlled by the same effects as during filling. The strain is sensitive to draining of ponded water, and a sharp tension occurs when the pressure at the surface of the sand drops below zero. This is equivalent to the sharp increase in compression as the transition zone reaches the surface during filling. The transition zone compresses during draining that causes expansion in the underlying sand. As a result, the downward moving transition zone causes tension as it approaches, and compression when it arrives and passes a strain measurement location.

SIGNIFICANCE

This work demonstrates a new method for measuring strain in unconsolidated materials. The strain ribbon is minimally invasive, inexpensive, and robust. The compliance is similar to soil, so strain in the soil is expected to be readily transferred to the optical fiber. Previous methods for measuring strain in unconsolidated materials require much larger devices with complex anchors. The strain ribbon will enable strains at many locations separated by dm to be measured with a resolution of 10^{-8}. Applications are envisioned in hydrogeology, soil science, agriculture, geotechnical engineering, and other fields where strain in soil is of interest.

This work also demonstrates new insights into strains that occur during changes in saturation. Conventional expectations that strain is proportional to the local pressure

change, according to Hooke's Law, are met in some locations, but other processes also affect strain. In particular, stress transfer, where the strain in one location is affected by fluid pressure in another location, is also important. This work also identified a possible boundary condition associated with capillary effects near a free surface that appears to be previously unrecognized.

The new technology and new insights it provides set the stage for evaluations of this approach in the field. The ultimate significance of this work will be the role it played preparing a new method for monitoring strains in hydrogeologic field applications.

REFERENCES

Aharoni, I., Siebner, H., & Dahan, O. (2017). Application of vadose-zone monitoring system for real-time characterization of leachate percolation in and under a municipal landfill. *Waste Management*, *67*, 203–213. https://doi.org/10.1016/j.wasman.2017.05.012

ASTM. (2003). *Standard Test Methods for Determination of the Soil Water Chararcteristic Curve for Desorption Using a Hanging Column, Pressure Extractor, Chilled Mirror Hygrometer, and/or Centrifuge*. *04*(February).

Baram, S., Kurtzman, D., & Dahan, O. (2012). Water percolation through a clayey vadose zone. *Journal of Hydrology*, *424–425*, 165–171. https://doi.org/10.1016/j.jhydrol.2011.12.040

Blonquist, J. M., Jones, S. B., & Robinson, D. A. (2005). A time domain transmission sensor with TDR performance characteristics. *Journal of Hydrology*, *314*(1–4), 235–245. https://doi.org/10.1016/j.jhydrol.2005.04.005

Dal Moro, G., & Zadro, M. (1998). Subsurface deformations induced by rainfall and atmospheric pressure: Tilt/strain measurements in the NE-Italy seismic area. *Earth and Planetary Science Letters*, *164*(1–2), 193–203. https://doi.org/10.1016/S0012-821X(98)00203-9

Dobriyal, P., Qureshi, A., Badola, R., & Hussain, S. A. (2012). A review of the methods available for estimating soil moisture and its implications for water resource management. *Journal of Hydrology*, *458–459*, 110–117.

https://doi.org/10.1016/j.jhydrol.2012.06.021

Engman, E. T. (1991). Applications of microwave remote sensing of soil moisture for water resources and agriculture. *Remote Sensing of Environment*, *35*(2–3), 213–226. https://doi.org/10.1016/0034-4257(91)90013-V

Fattahi, H., & Amelung, F. (2016). InSAR observations of strain accumulation and fault creep along the Chaman Fault system, Pakistan and Afghanistan. *Geophysical Research Letters*, *43*(16), 8399–8406. https://doi.org/10.1002/2016GL070121

Freeman, C. (2012). *Estimating Water Flux and Storage Using Displacement Measurements*.

Gambolati, G., Teatini, P., & Tomasi, L. (1999). *Stress-Strain Analysis in Productive Gas/Oil Reservoirs*. *1519*(October 1997), 1495–1519.

Gemperline, M. C., & Rinehart, R. V. (2018). *Soil-Pipe Interface Friction Coefficients for Buried PE4710 Pipe*.

Hagiwara, Y. (1974). Probability of earthquake occurrence as obtained from a Weibull distribution analysis of crustal strain. *Tectonophysics*, *23*(3), 313–318. https://doi.org/10.1016/0040-1951(74)90030-4

Hall, K. M., & Fox, P. J. (2018). Large Strain Consolidation Model for Land Subsidence. *International Journal of Geomechanics*, *18*(11), 06018028. https://doi.org/10.1061/(asce)gm.1943-5622.0001267

Hisz, D. B., Murdoch, L. C., & Germanovich, L. N. (2013). A portable borehole

extensometer and tiltmeter for characterizing aquifers. *Water Resources Research*, *49*(12), 7900–7910. https://doi.org/10.1002/wrcr.20500

Honeywell. (n.d.). *FSG Series Force Sensor* (pp. 268–270).

Hongdong, F., Kazhong, D., Chengyu, J., Chuanguang, Z., & Jiqun, X. (2011). Land subsidence monitoring by D-InSAR technique. *Mining Science and Technology*, *21*(6), 869–872. https://doi.org/10.1016/j.mstc.2011.05.030

Hua, L., Song, Y., Cheng, B., Zhu, W., Zhang, Q., & Xiao, H. (2017). Coherence-length-gated distributed optical fiber sensing based on microwave-photonic interferometry. *Optics Express*, *25*(25), 31362–31376.

Hua, L., Zhu, X., DeWolf, S., Lei, J., Zhang, Q., Murdoch, L., & Xiao, H. (2020). Phase demodulation by Frequency Chirping in Coherence Microwave Photonic Interferometry. *IEEE Journal of Selected Topics in Quantum Electronics*, *27*(2), 7700109. https://doi.org/10.1109/jstqe.2020.2975575

Inaudi, D., & Glisic, B. (2006). Distributed fiber optic strain and temperature sensing for structural health monitoring. *Proceedings of the 3rd International Conference on Bridge Maintenance, Safety and Management - Bridge Maintenance, Safety, Management, Life-Cycle Performance and Cost, July*, 963–964. https://doi.org/10.1201/b18175-412

Keller, T., Arvidsson, J., Schjønning, P., Lamandé, M., Stettler, M., & Weisskopf, P. (2012). In Situ Subsoil Stress-Strain Behavior in Relation to Soil Precompression Stress. *Soil Science*, *177*(8).

https://journals.lww.com/soilsci/Fulltext/2012/08000/In_Situ_Subsoil_Stress_Strain_Behavior_in_Relation.3.aspx

Leung, C. K. Y., Wan, K. T., Inaudi, D., Bao, X., Habel, W., Zhou, Z., Ou, J., Ghandehari, M., Wu, H. C., & Imai, M. (2015). Review: optical fiber sensors for civil engineering applications. *Materials and Structures/Materiaux et Constructions*, *48*(4), 871–906. https://doi.org/10.1617/s11527-013-0201-7

Luttrell, K., Mencin, D., Francis, O., & Hurwitz, S. (2013). Constraints on the upper crustal magma reservoir beneath Yellowstone Caldera inferred from lake-seiche induced strain observations. *Geophysical Research Letters*, *40*(3), 501–506. https://doi.org/10.1002/grl.50155

Madjdabadi, B., Valley, B., Dusseault, M. B., & Kaiser, P. K. (2016). Experimental evaluation of a distributed Brillouin sensing system for measuring extensional and shear deformation in rock. *Measurement: Journal of the International Measurement Confederation*, *77*, 54–66. https://doi.org/10.1016/j.measurement.2015.08.040

Martin, J. P., & Koerner, R. M. (1984). The influence of vadose zone conditions in groundwater pollution. Part II: Fluid movement. *Journal of Hazardous Materials*, *9*(2), 181–207. https://doi.org/10.1016/0304-3894(84)80017-5

Murdoch, L., Falta, R., & Moysey, S. (2016). *MEASURING AND INTERPRETING VERTICAL DISPLACEMENTS RELATED TO SHALLOW HYDROLOGIC PROCESSES A Proposal Presented to The Graduate School of Clemson University In Partial Fulfillment of the Requirements for the Degree Master of Science*

Hydrogeology by Colby T. May.

Neelam, M. K., & Kalaga, S. (2002). Elastic properties of PVC pipes. *Journal of Structural Engineering (Madras)*, *29*(2), 91–96.

Nitzsche, K., & Herle, I. (2020). Strain-dependent slope stability. *Acta Geotechnica*, *15*(11), 3111–3119. https://doi.org/10.1007/s11440-020-00971-3

Ochsner, T. E., Cosh, M. H., Cuenca, R. H., Dorigo, W. A., Draper, C. S., Hagimoto, Y., Kerr, Y. H., Larson, K. M., Njoku, E. G., Small, E. E., & Zreda, M. (2013). State of the Art in Large-Scale Soil Moisture Monitoring. *Soil Science Society of America Journal*, *77*(6), 1888–1919. https://doi.org/10.2136/sssaj2013.03.0093

Philip, J. R., & Knight, J. H. (1989). Unsaturated Seepage and Subterranean Holes: Conspectus, and Exclusion Problem for Circular Cylindrical Cavities. *Water Resources Research*, *25*(1), 16–28.

Prakash, G., Sadhu, A., Narasimhan, S., & Brehe, J. M. (2018). Initial service life data towards structural health monitoring of a concrete arch dam. *Structural Control and Health Monitoring*, *25*(1), 1–19. https://doi.org/10.1002/stc.2036

Satoshi Yamashita,1 Michele Jamiolkowski, 2 and Diego C. F. Lo Presti3. (2000). Stiffness Nonlinearity of Three Sands. *JOURNAL OF GEOTECHNICAL AND GEOENVIRONMENTAL ENGINEERING*, *126*(October), 929–938.

Thrash, C. (2016). *Measuring and Interpreting Vertical Displacements Related to Shallow Hydrologic Processes*. 1–161.

Topp, G. C., Lapen, D. R., Young, G. D., & Edwards, M. (2001). Evaluation of shaft-mounted TDT readings in disturbed and undisturbed media. *TDR 2001 - Second International Symposium and Workshop on Time Domain Reflectometry for Innovative Geotechnical Applications, Northwestern University, Evanston, Ill., 5-7 September 2001*, *2000*, 62–71.

van Genuchten, M. T. (1980). A Closed-form Equation for Predicting the Hydraulic Conductivity of Unsaturated Soils. *Soil Science Society of America Journal*, *44*, 892–898.

Wang, H. F. (2000). *Theory of Linear Poroelasticity with Applications to Geomechanics and Hydrogeology*. Princeton University Press. http://www.jstor.org/stable/j.ctt1jktrr4

Warpinski, N. R., Branagan, P. T., & Engler, B. P. (1997). *Evaluation of a Downhole Tiltmeter Array for Monitoring Hydraulic Fractures*. *34*(329), 3–4.

Weiss, J. R., Walters, R. J., Morishita, Y., Wright, T. J., Lazecky, M., Wang, H., Hussain, E., Hooper, A. J., Elliott, J. R., Rollins, C., Yu, C., González, P. J., Spaans, K., Li, Z., & Parsons, B. (2020). High-Resolution Surface Velocities and Strain for Anatolia From Sentinel-1 InSAR and GNSS Data. *Geophysical Research Letters*, *47*(17). https://doi.org/10.1029/2020GL087376

You, R., Ren, L., & Song, G. (2019). A novel fiber Bragg grating (FBG) soil strain sensor. *Measurement: Journal of the International Measurement Confederation*, *139*, 85–91. https://doi.org/10.1016/j.measurement.2019.03.007

Zreda, M., Shuttleworth, W. J., Zeng, X., Zweck, C., Desilets, D., Franz, T., & Rosolem, R. (2012). COSMOS: The cosmic-ray soil moisture observing system. *Hydrology and Earth System Sciences*, *16*(11), 4079–4099. https://doi.org/10.5194/hess-16-4079-2012